

https://dspace.org/

Electrocatalytic detection of drugs of abuse using onion-like carbon based electrocatalysts

Ehirim, Tobechukwu Justice

2024

https://hdl.handle.net/10539/37432

Downloaded from a DSpace repository. https://dspace.org/

ELECTROCATALYTIC DETECTION OF DRUGS OF ABUSE USING ONION-LIKE CARBON BASED ELECTROCATALYSTS



UNIVERSITY OF THE
WITWATERSRAND,
JOHANNESBURG

Submitted by

Tobechukwu Justice Ehirim (1569304)

Supervisor: Prof. Kenneth I. Ozoemena

A thesis submitted to the Faculty of Science, University of Witwatersrand Johannesburg in fulfilment for the degree of

Doctor of Philosophy in Chemistry

Johannesburg

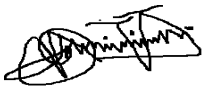
November 2022

DECLARATION

I solemnly declared that this thesis is self-reliant and independently studied. It is being submitted to the School of Chemistry, Faculty of Science, University of the Witwatersrand, Johannesburg for the award of the degree of Doctor of Philosophy. It has not been submitted previously to any other institution of higher learning for consideration of any degree.

Tobechukwu Justice Ehirim **24 = 02 - 2023**

Name Date



Signature

DEDICATION

This Ph.D. work is dedicated to my late father, Chief. Livinus Uzoma Nlewedimanya Ehirim (Uzoudo 1 of Amazano) who taught me never to get tired of developing myself through life-long acquisition of knowledge, and my mother, Lolo. Dorathy Adaeze Ehirim (Ugo-si-Mba) who offered herself as a reminder and launching pad unto this Academic work long after the passing of my father, and specially dedicated to Jehovah Chineke Bu Eze, God Almighty who grants me the grace to so do.

ACKNOWLEDGEMENTS

My deepest gratitude and indebtedness go to my supervisor, Professor Kenneth Ikechukwu Ozoemena, a world-renowned chemist and researcher, for the opportunity given me, his dedicated guidance, encouragement and support that made this accomplishment possible. A special and heartfelt appreciation to my beautifully brilliant and wonderfully made wife, Lolo. Vivienne Ogechi T.J. - Ehirim, my academically supportive children, Ubasinachi J.TJ-Ehirim, Chimzikora Mikayla TJ-Ehirim, T. Jehovah Bu Eze TJ-Ehirim, Chiamaka Rhianda TJ-Ehirim and Chidera E. TJ-Ehirim. Not forgetting my siblings and relatives who has been serious sources of encouragement and motivation, Chika Blaise Ehirim, Igwebuike Bede Ehirim, Uche Barbara Ehirim-Umunnakwe, Chidera Pat, Ehirim-Uka and Chinedu Ashinobi, Uchenna Chukwumezie, Ifeanyi Orji, Patrick Obi, Dr. Rita Ozoemena, Uche Olebuike, amongst others.

I wish to specially acknowledge and thank my co-researcher, and co-author, Okoroike Celestine Ozoemena who put in so much dedication to enhance the achievement of this feat through his academic collaborations. My gratitude also goes to my colleagues and co-researchers at the Ozoemena research group, at The University of the Witswatersrand, Dr. Aderemi Haruna, Dr.Thapelo Mofokeng, Dr. Patrick Mwonga, Dr. Adewale Ipadeola, Siwaphiwe Pheteni, Kelechi Lebechi, Refilwe Modise, Lesego Goalahle, Ms. Itumeleng Mokhosi, Thokozane Tsoari, Sebenzile Shabalala, Seremo Podile, Dr. Tobile Khawula, Bokome Shaku, Dr. Victor Mashindi, Coolani Fakude, Tebogo Tsekedi, Funanani Tshivase, also not forgetting Prof. Careen Billing of the Wits School of Chemistry for her support through the use of her laboratory, and a host of others.

Finally, I want to acknowledge my colleagues at work and my Pharmacy Profession who have in no little way supported me through this academic journey amongst whom are S.Choma, D,Bayerver, R.Lotter, N.P. Mthetwa, C,Hadebe, S. Dikgang, L. Maswabi, L.V. Khambule, R. M. Mashile, A. Paruk, T. Tshabalala, N. H. Ndlovu, F. Asmal, T. Shabangu, H. Pabhoo, D.E. Dlamini, V. Adoons, T. Ncube, amongst others.

RESEARCH OUTPUTS

LIST OF PUBLICATIONS

1) **Tobechukwu J. Ehirim,** Okoroike C. Ozoemena, Patrick V. Mwonga, Aderemi B. Haruna, Thapelo P. Mofokeng, Karolien De Wael, and Kenneth I. Ozoemena, Onion-Like Carbons Provide a Favorable Electrocatalytic Platform for Sensitive Detection of Tramadol Drug, *ACS Omega* **7, 51** (2022) 47892-47905. doi.org/10.1021/acsomega.2c05722

2) Okoroike C. Ozoemena, Nsovo S. Mathebula, **Tobechukwu J. Ehirim**, Tobile Maphumulo, Goodness M. Valikpe, Jerry L. Shai, Kenneth I. Ozoemena. Onion-like carbon re-inforced electrospun polyacrylonitrile fibres for ultrasensitive electrochemical immunosensing of *Vibrio cholerae* toxin. *Electrochimica Acta* **356** (2020) 136816. doi.org/10.1016/j.electacta.2020.136816

3) Okoroike C. Ozoemena· **Tobechukwu J. Ehirim**· Tobile Khawula· Katlego Makgopa· Leshweni J. Shai· Kenneth I. Ozoemena. Bovine Serum Albumin-Dependent Charge-Transfer Kinetics Controls the Electrochemical Immunosensitive Detection: Vibrio cholerae as a Model Bioanalyte, *Electrocatalysis* **12** (2021) 595-604. doi.org/10.1007/s12678-021-00673-8.

4) **Tobechukwu J. Ehirim,** Okoroike C. Ozoemena, Adewale K, Ipadeola, Patrick V. Mwonga, Aderemi B. Haruna, Thapelo P. Mofokeng, Karolien De Wael, and Kenneth I. Ozoemena, Utilizing the unique electronic interactions between Pd and CeO2@onion carbon for enhanced electrocatalytic oxidation of ethanol and sensing, Electrochimica Acta (under review).

PODIUM PRESENTATIONS AT INTERNATIONAL CONFERENCES

5) **Tobechukwu J. Ehirim**, Siwaphiwe Pheteni, Adewale Ipadeola, Kenneth I. Ozoemena. Electrochemical detection of Tramadol at onion-like carbon modified electrode. 70th Annual Meeting of the International Society of Electrochemistry. Held August 4 – 9, 2019 at the International Conference Centre, Durban, South Africa.

6) **Tobechukwu J. Ehirim**, Okoroike C. Ozoemena, Adewale Ipadeola, Kenneth I. Ozoemena. Electrochemical detection of drugs of abuse. 4th African Nanotechnology Conference/ Workshop. Held 19th – 23rd of July at University of Nigeria, Nsukka (UNN), Enugu State, Nigeria.

MEMBERSHIP OF PROFESSIONAL BODIES AND ASSOCIATIONS

1. The South African Pharmacy Council (SAPC).

ABSTRACT

Substance abuse is a serious problem worldwide. Among abused substances, tramadol and alcohol are one of many. There is an urgent need to use electrochemical method for their detection since electrochemistry methods are simple, low-cost, high sensitivity and can easily be miniaturised. This PhD work reports the first investigation on the application of nanodiamond-derived onion-like carbons (OLC) and conductive carbon black (CB) as (i) electrocatalysts for the detection of tramadol, and (ii) as support materials for nano-sized palladium electrocatalysts (Pd/OLC, Pd/CB, Pd-CeO_2/OLC) for the detection of ethanol. The catalysts were characterised with X-ray diffraction (XRD), Raman, Brunauer–Emmett–Teller (BET), Thermal gravimetric analysis (TGA), X-ray photoelectron spectroscopy (XPS), Scanning electron microscopy (SEM) and Transmission electron microscopy (TEM).

For the detection of tramadol, OLC gave the best sensing performance compared to CB. Theoretical calculations (DFT simulations) predict that OLC is better because it allows for weaker interaction energy with tramadol (E_{ad} = -26.656 eV) than CB (E_{ad} = -40.174 eV). OLC-modified glassy carbon electrode (GCE-OLC) shows a wide linear calibration curve (55 – 392 μM), high sensitivity (0.0315 μA /μM), low limit of detection (LoD) and quantification (LoQ) of 3.8 and 12.7 μM, respectively. OLC-modified screen-printed electrode (SPE-OLC) successfully detected tramadol in real tramadol drug and human serum. The OLC-based electrochemical sensor promises to be useful for sensitive and accurate detection of tramadol in clinics, quality control and routine quantification of tramadol in pharmaceutical formulations.

For the oxidation and detection of ethanol, Pd/CB, Pd/OLC and Pd-CeO_2/OLC, were studied as catalysts. In comparison, adding ceria (CeO_2) to Pd/OLC, the performance was enhanced significantly than in carbon-only support for palladium. GCE/Pd-CeO_2/OLC shows the best electrocatalytic performance (i.e., high current density, fast electron transport, etc). DFT calculation, supported by XPS and HRTEM data, predict that this high activity may be related to CeO_2 modulating the electronic properties of the catalyst. GCE/Pd-CeO_2/OLC gave wide linear range for ethanol sensing (38.5 – 286 mM), excellent sensitivity (0.00024 mA mM^{-1}) and LoD of ~ 8.7 mM. The GCE/Pd-CeO_2/OLC shows excellent potential for application in real samples of commercial alcoholic beverages and human serum, with satisfactory recoveries (89 – 108 %).

TABLE OF CONTENTS

DECLARATION i

DEDICATION ii

ACKNOWLEDGEMENTS iii

RESEARCH OUTPUTS iv

ABSTRACT vi

TABLE OF CONTENTS ix

LIST OF FIGURES xv

LIST OF TABLES xx

LIST OF SYMBOLS xxi

LIST OF ABBREVIATIONS xxii

CHAPTER 1 1

INTRODUCTION 1

1.1 Research Problems 1

1.2 Rationale or Justifications 2

1.3 Research Aim and Objectives 3

1.3.1 Aim of the study 3

1.3.2 Objectives of Study 4

1.4 Outline of the thesis 4

1.5 References 6

CHAPTER 2 8

LITERATURE REVIEW 8

2.1 Rationale for the detection of tramadol and alcohol 8

2.2 Brief Overview of Current Detection Methods of Ethanol: Pros and Cons 13

2.2.1 UV-Visible spectroscopy 13

2.2.3 Mass Spectroscopy 14

2.2.4 High Performance liquid chromatography (HPLC) 14

2.2.5 Electrochemical detection (Advantages & Disadvantages). 15

2.2.6 Electrode materials 16

2.2.6.1 Onion-Like Carbon (OLC) 16

2.2.6.2 Palladium Carbon on Carbon and Carbon-Ceria Supports as Catalysts 18

2.2.7 Tramadol and Ethanol 19

2.2.7.1 Tramadol 19

2.2.7.2 Ethanol 19

2.2.8 Ferri-Ferrocyanide Solution. 20

2.2.9 Amstel Beer (4.0 % Alc) 20

2.2.10 Nederberg Wine (13.0 % Alc) 20

2.2.11 Interferents 20

2.3 References 22

CHAPTER 3 27

MATERIALS AND METHODS 27

3.1 Material Characterization 28
3.1.1 Powder X-ray Diffraction (PXRD) 28
3.1.2 Raman Spectroscopy 28
3.1.3 Scanning electron microscopy (SEM) 29
3.1.4 Energy-dispersive X-ray spectroscopy (EDX) 29
3.1.5 Transmission electron microscopy (TEM) 29
3.1.6 Thermogravimetric analysis (TGA) 30
3.1.7 Brunauer-Emmett-Teller (BET) surface area analysis 30
3.1.8 X-ray Photoelectron Spectroscopy (XPS) 30
3.2 Electrochemical Characterization Techniques 31
3.2.1 Cyclic voltammetry 31
3.2.2 Square wave voltammetry 31
3.2.3 Differential pulse voltammetry (DPV) 32
3.2.4 Electrochemical impedance spectroscopy 32
3.2.5 Chronoamperometry 32
3.3 Evaluation of Electrochemical Sensor's Figures of Merit. 33
3.3.1 Sensitivity 33
3.3.2 Limit of detection 33
3.3.3 Limit of quantification 34
3.3.4 Specificity / Selectivity 34
3.3.5 Repeatability / Stability 34

3.4 References..... 35

CHAPTER 4..... 37

4.1 Introduction..... 38

4.2 Experimental section..... 40

4.2.1 Materials, reagents and methods..... 40

4.2.2 Physical property characterization..... 41

4.2.3 Electrochemical detection procedure..... 41

4.2.4 Density functional theory (DFT) calculations..... 43

4.3 Results and discussion..... 44

4.3.1 Materials characterization..... 44

4.3.2 Cyclic voltammetry: mass transport and charge-transfer kinetics..... 47

4.3.3 Electrochemical Impedance Spectroscopy: Charge-Transfer Kinetics . 52

4.3.4 Electrocatalytic detection of tramadol..... 55

4.3.5 Predicting the High Electrocatalytic Activity of OLC Over CB Towards the Detection of Tramadol: DFT Calculations… 58

4.3.6 Analytical application of OLC-based electrochemical sensors..... 61

4.3.6.1 Determination of raw tramadol in PBS (pH 7.40……....61

4.3.6.2 Determination of tramadol in pharmaceutical sample and human serum……. .....……62

4.4 Conclusion..... 66

4.5 References..... 67

CHAPTER 5..... 77

5.1 Introduction 78

5.2 Experimental 80

5.2.1 Materials and reagents 80

5.2.2 Synthesis procedures 81

5.2.2.1 Synthesis of Pd/carbon. 81

5.2.2.2 Synthesis of OLC-CeO_2 support 81

5.2.2.3 Synthesis of Pd-CeO_2/OLC 82

5.2.3 Physical property characterization 82

5.2.4 Density functional theory (DFT) calculations 83

5.2.5 Electrochemical and physical characterization 84

5.3 Results and Discussion 85

5.3.1 Materials characterization 85

5.3.2 Cyclic voltammetry and EIS: Charge-transfer kinetics 92

5.3.3 Electrocatalytic Oxidation and Detection of Ethanol in Alkaline Medium 96

5.3.4 Reasons for the high performance of the Pd-CeO_2/OLC electrocatalyst towards ethanol oxidation reaction 100

5.3.5 Analytical application of Pd-CeO2/OLC-based electrochemical sensor 106

5.3.5.1 Alcohol detection in alkaline medium……106

5.3.5.2 Determination of ethanol in real alcoholic samples……107

5.4 Conclusion 108

5.5 References..... 109

CHAPTER 6..... 120

6.1 Electrocatalytic Sensing of Tramadol..... 120

6.2 Electrocatalytic Sensing of Alcohol..... 121

APPENDIX..... 123

LIST OF FIGURES

Figure 2.1 Isomeric structures of tramadol……..12

Figure 2.2 Chemical Structure of Ethanol……13

Figure 2.3 Pictures depicting faces of alcohol and drug abuse in the society (Courtesy: Bing images, assessed 15 March 2022)……..……13

Figure 2.4 (A) HRTEM images of onion-like carbon (OLC) and (B) its structural representation. (Ugarte,1995)……18

Figure 4.1 Isomeric structures of commercial tramadol hydrochloride……41

Figure 4.2 Electrode modification for tramadol electrocatalytic oxidation and sensing. The images are modified from the photographs obtained from electrode suppliers: (A) courtesy of BASi, copyright 2022; and (B) courtesy of Metrohm Dropsens, copyright 2022)……45

Figure 4.3 SEM images of (A) CB and (B) OLC, and (C) HRTEM image of OLC….46

Figure 4.4 Comparing powder XRD (A), Raman spectra (B), BET adsorption desorption curve, and (inset) pore size distribution curves (C), and TGA and their corresponding derivative TGA (D) of OLC and CB……47

Figure 4.5 Cyclic voltammograms of the electrode at (A) 10 mV/s ansd (B) 150 mV/s; CV at different scan rates (10 – 150 mV/s) for the (C) OLC and (E) CB, and their corresponding plots of peak currents versus square root of scan rate (D) and (F), respectively. All data were collected in a redox probe ($[Fe(CN)_6]^{4-}$/$[Fe(CN)_6]^{3-}$ in 0.1 M KCl)……50

Figure 4.6 (A) Nyquist plots and (B-D) Bode plots of the GCE, GCE-OLC and GCE-CB. Data points are experimental, while lines are fitted data using the electrical equivalent circuit (inset in Figure 6A). All data were collected in redox probe ([Fe(CN)6]4−/[Fe(CN)6]3−) in 0.1 M KCl……..55

Figure 4.7 (A) CV evolutions of the GCE, GCE-CB and GCE-OLC in PBS (pH 7.4) containing 0.5 mM tramadol at 20 mV/s, (B) Comparing the CVs of GCE-OLC in PBS alone and PBS containing 0.5 mM tramadol at 20mV/s, (C) CV evolution showing the effect of changing scan rates on the current responses, (D) plot of peak potential versus log scan rate. All data acquired in PBS containing 0.5 mM tramadol……..58

Figure 4.8 Adsorption sites of tramadol at the surfaces of CB and OLC. The dark blue dots (shades) show the possible site tramadol molecules are adsorbed. Inset is used to determine the isosurface potentials of tramadol @+/- 0.05181 isovalue(a.u.), for tramadol molecule……61

Figure 4.9 Band structures and PDOS for tramadol adsorbed on (A,B) CB and (C,D) OLC electrodes……..63

Figure 4.10 (A) Typical square wave voltammograms obtained in PBS (pH 7.4) containing different concentrations of tramadol (0 – 392 μM), and (B) plot of peak current response versus concentration of tramadol……64

Figure 4.11 Typical SWV curves (A, C) obtained in real sample analysis using screen-printed carbon electrode (SPCE) modified with OLC (SPCE-OLC) for tramadol in drug capsule (A) and in human serum solution (C); and the plot of background-subtracted peak current responses versus the concentrations of tramadol (B,D)……..66

Figure 5.1 TGA of CB and OLC and their derivative TGA……87

Figure 5.2 Raman spectra (A-C) and XRD patterns (D-F) of the electrocatalysts……88

Figure 5.3 Typical low-resolution HRTEM images of (A) Pd/C, (B) Pd/OLC and (C) Pd-CeO_2/OLC, and typical HRTEM images of (D) Pd/CB; (E) Pd/OLC and (F) Pd-CeO_2/OLC. The particle size distribution of (G) PdCB, (H) Pd/OLC and (I) Pd-CeO_2/OLC……..90

Figure 5.4 XPS data showing the wide spectra of (A) Pd/OLC and (B) Pd/CeO_2-OLC; C 1s scans of (C) Pd/OLC and (D) Pd-CeO_2/OLC; O 1s scans of (E) Pd/OLC and (F) Pd-CeO_2/OLC; Pd 3d scans of (G) Pd/OLC and (H) Pd-CeO_2/OLC; and Ce 3d scan of (I) of Pd-CeO_2/OLC……...91

Figure 5.5 XPS data for the core Pd 3d scans of (A) Pd/CB, (B) Pd/OLC, (H) Pd-CeO_2/OLC; and Ce 3d scan of (D) Pd-CeO_2/OLC……93

Figure 5.6 Typical comparative (A) cyclic voltammograms at 100 mVs^{-1}, and (B) Nyquist plots of the electrocatalysts immobilized onto GCE surface obtained at 0.22 V (vs Ag|AgCl, 3 M KCl). All data were collected in a redox probe ($[Fe(CN)_6]^{4-}$/$[Fe(CN)_6]^{3-}$ in 0.1 M KCl)……94

Figure 5.7 Cyclic voltammograms of the electrode at (A) 10 mV/s ansd (B) 150 mV/s; CV at different scan rates (10 – 150 mV/s) for the (C) OLC and (E) CB, and their corresponding plots of peak currents versus square root of scan rate (D) and (F), respectively. All data were collected in a redox probe ($[Fe(CN)_6]^{4-}$/$[Fe(CN)_6]^{3-}$ in 0.1 M KCl)……96

Figure 5.8 Cyclic voltammograms (A) 1.0 M KOH alone and (B) mixture of 1.0 M KOH and 1.0 M ethanol of the Pd-based electrocatalysts……97

Figure 5.9 (A-C) Scan rate studies and (D) plots of the current against the square root of scan rates of the electrocatalysts toward ethanol oxidation reaction……99

Figure 5.10 Acetyl group adsorption sites at the surfaces of (A) Pd/CB, (B) Pd/OLC and (C) Pd-CeO_2/OLC. The dark blue dots (shades) show the possible site ethanol molecules are adsorbed……103

Figure 5.11 HRTEM showing the interfacial interaction between Pd and CeO2 in Pd-CeO_2/OLC, and the valence band spectra of the (B) Pd/CB (C) Pd-CeO2/CB and (D) Pd-CeO_2/OLC catalysts……..106

Figure 5.121 (A) Typical chronoamperometric curves obtained in 1 M KOH containing different concentrations of ethanol (0 – 666.7 mM), and (B) plot of peak current response versus concentration of ethanol…….....108

LIST OF TABLES

Table 4.1 Surface parameters CB and OLC materials……48

Table 4.1 CV parameters of the OLC- and CB-based electrodes obtained in a solution of redox probe..…… 51

Table 4.2 EIS parameters for the GCE, GCE-CB and GCE-OLCs…….56

Table 3.4 Predicted energy values from the DFT calculations accompanying the interaction of tramadol with the surfaces of OLC and CB……..61

Table 4.4 Summary of results obtained in this work for electrochemical sensing of tramadol, using the DPV method……68

Table 5.1 BET surface areas and porosity of the electrocatalysts……..90

Table 5.2 CV parameters of the OLC- and CB-based electrodes obtained in a solution of redox probe……...94

Table 5.3 Predicted energy values from the DFT calculations accompanying the interaction of tramadol with the surfaces of Pd/CB, Pd/OLC and Pd-CeO_2/OLC……105

Table 5.4 Summary of results obtained in this work for electrochemical sensing of tramadol, using the DPV method……..110

LIST OF SYMBOLS

A	Electron transfer coefficient
Aa	Anodic electron transfer coefficients
Ac	Cathodic electron transfer coefficients
υ	Scan rates
Δ	Standard deviation
Λ	Wavelength
ΔE	Peak potential separation
C	Analytes bulk concentration (mol/L)
℃	Degree Celsius
D	Diffusion coefficient of analytes (cm^2/s)
E1/2	Half – wave potential
Ω	Ohms
µm	Micrometre
Z'	Real impedance
Z''	Imaginary impedance
Ma	mill Ampere
$-\Delta G$	Negative change in the Gibb's free energy

LIST OF ABBREVIATIONS

A	Electrodes electroactive area (cm^2)
AA	Ascorbic acid
API	Application Programming Interface
BET	Brunauer-Emmett-Teller
CA	Chronoamperometry
Cad	Cathode
CB	Carbon black
CE	Counter electrode
DC	Direct current
µ-DEFC	Direct ethanol micro-fuel cell
Cdi	Double layer capacitance
CE	Counter electrode
CNF	Carbon Nano Fibers
CNT	Carbon nanotube
COOH	Carboxylic acid
CV	Cyclic Voltammetry
D	Diffusion coefficient
DI	Deionized
DMF	N, N-Dimethylformamid
DPV	Differential Pulse Voltammetry
E	Potential
ECD	Electrochemical deposition

ECSA	Electrochemical active surface area
EDC	1-Ethyl-3-(3-dimethylaminopropyl carbodiimide hydrochloride
EEC	Electrical equivalent circuits
EG	Ethylene glycol
Epa	Peak anodic potential
Epc	Peak cathodic potential
EIS	Electrochemical Impedance Spectroscopy
EMS	Energy management system
EtOH	Ethanol
EOR	Ethanol oxidation reaction
FC	Fuel cell
FCBrAS	Fuel cell-based breath alcohol sensor
FCEV	Fuel cell electric vehicles
FTIR	Fourier transform infrared spectroscopy
Ferri/Ferro	Potassium Ferrocyanide/Potassium Ferricyanide
FRA	Frequency response analyser (analysis)
GCE	Glassy carbon electrode
GHG	Greenhouse gas
GPES	General purpose electrochemical system
HCl	Hydrochloric acid
HER	Hydrogen evolution reaction
HOR	Hydrogen oxidation reaction
Ip	Peak current
I	Current

Ipa	Peak anodic current
Ipc	Peak cathodic current
KCl	Potassium chloride
K-L	Koutecky-Levich
KHz	kilohertz
kV	Kilovolt
LoD	Limit of Detection
LoQ	Limit of Quantification
M	Molar
mHz	Milli hertz
Min	Minutes
Mg	Milligram
ml	Millilitre
mM	Millimolar concentration
mW	Milliwatt
N_2	Nitrogen
O_2	Oxygen
OLC	Onion-like carbon
ORR	Oxygen reduction reaction
Pd	Palladium
Pt	Platinum
RC	Resistant-current
Rct	Charge transfer resistance
Ret	Electron transfer resistance

Rs	Ohmic resistance of the electrolyte solution
SEM	Scanning Electron Microscope
SWV	Square Wave Voltammetry
TEM	Transmission Electron Microscopy
UA	Uric acid
V	Volt
Vs	Versus
W	Watt
WE	Working electrode
WHO	World Health Organisation
WITS	University of the Witwatersrand
XAS	X-ray Absorption Spectroscopy
XPS	X-ray Photoelectron
XRD	X-ray Diffraction
Z	Impedance
Zw	Warburg impedance

CHAPTER 1

INTRODUCTION

The research problems, research aims and objectives, significance of the study and outline of the thesis are summarised in this chapter.

1.1 Research Problems

Drugs of abuse (DOA) are normally described as psychoactive substances used by individual or people for numerous reasons including (i) curiosity and peer influence amongst youth, (ii) prescribed drugs, that are initially deliberated for pain relief, are rather used for recreational activities and become addictive, (iii) religious belief (people use them for rituals), and (iv) an avenue to get creative inspiration. However, the DOA poses severe negative consequences on humans' health and the society at large. The consequences of the DOA on human body makes it to be classified into three categories:

- Depressants: These substances may cause depression.
- Stimulants: These substances stimulate the brain for alertness and accelerate activities like rapid heat rate, dilated pupils, increased blood pressure, nausea or vomiting and behavioral change (i.e., agitation, and impaired judgment).
- Hallucinogens: These substances results in hallucinations and an "out of the world" feeling of dissociation from one's comportment, causing distorted sensory perception, delusion, paranoia and even depression.

Some of the DOA are tramadol, alcohol, cocaine, tobacco, marijuana, heroin, opioids etc. Tramadol and alcohol are amongst the most abused substances in the world that cause significant global risk factors, resulting in disability and premature loss of life [1]. The health implication of the tramadol and alcohol abuse leads to major economic cost such as health care and law enforcement expenditure, low productivity, and other unforeseen cost (i.e., harm to others) [2]. A study has shown that 1-15% of drivers on the highway drive in the influence of one or more DOA, thereby impairing their driving ability culpable of an accident [3]. Abusing of drugs and substances, particularly tramadol and alcohol is becoming a major challenge amongst our teeming youths in the society. Hence, there is need for law enforcement agents to be provided with devices that can detect the abused substances in individual or people on site, so that they could be easily prosecuted and perhaps may serve as deterrent to other youths and the elderly to desist from abusing these drugs.

1.2 Rationale or Justifications

The need for these drugs of abuse to be detected and controlled more effectively using less cumbersome, much simpler, faster and cost-effective techniques than the conventional techniques has become imperative. Different conventional methods such as Uv-visible spectroscopy, Raman spectroscopy, high-performance liquid chromatography, gas chromatography, spectrofluorometry and electrochemical technique have been proffered for detecting these abused substances, but there is limitation to the use of all the techniques for on-site detection of DOA, except the electrochemical techniques,

since the method consistently produce exceptional performance. Furthermore, the method is easy to carry out and can provide rapid detection and selectivity and sensitivity [4]. This finding informed our interest to design and fabricate the electrochemical-based devices for the detection of tramadol and alcohol, leading to the main crux of this study. This research holds a number of promises to the body of knowledge in that amongst other things it can potentially:

- Provide us with faster and more sensitive techniques to determine drugs and substances of abuse like tramadol or alcohol in humans
- Provide us with a more selective technique in the determination of tramadol and Alcohol.
- Provide us with a less cumbersome, cost-effective and miniature facility to detect drugs and substances of abuse, e.g., tramadol, alcohol.

This study can potentially add to the efforts in enhancing control of drug abuse (e.g., tramadol abuse,) and substances abuse (e.g., Alcohol abuse, and dangerous habits like driving under the influence of substances of abuse in society. The results obtained here can be extended to other drugs and substances of abuse.

1.3 Research Aim and Objectives

1.3.1 Aim of the study

The aim of this study was to investigate the performance of nanocarbons- (i.e., onion-like carbon (OLC), carbon black Nanotubes and palladium-based (i.e., palladium on carbon (Pd/CB), palladium on carbon-ceria composite (Pd-CeO_2/CB), palladium on OLC (Pd/OLC), palladium on OLC-ceria composite (Pd-CeO_2/OLC)

electrode materials in the electrocatalytic detection of tramadol and alcohol, respectively.

1.3.2 Objectives of Study

The aim was achieved with the following:

(i) To synthesize the nanocarbon-based materials (OLC, CB) and palladium-based materials (Pd/C, Pd/C-CeO_2, Pd/OLC and Pd/OLC-CeO_2) using microwave-assisted methods.

(ii) To characterize the nanocarbon-based materials (OLC, CB) and palladium-based materials (Pd/C, Pd/C-CeO_2, Pd/OLC and Pd/OLC-CeO_2) using scanning electron microscopy (SEM), transmission electron microscopy (TEM), energy-dispersive X-ray spectroscopy (EDX), ultraviolet-visible (UV-vis) spectroscopy, Fourier transform infra-red (FTIR), X-ray diffraction (XRD), Raman spectroscopy, X-ray photoelectron spectroscopy (XPS) and Brunauer-Emmett Teller (BET), thermogravimetric analysis (TGA).

(iii) Use of electrochemical technique such as cyclic voltammetry (CV), chronoamperometry (CA), square wave voltammetry (SWV), and electrochemical Impedance spectroscopy (EIS) to determine or measure the performances of the nanocarbon-based and palladium-based materials for the detection of tramadol and alcohol, respectively.

1.4 Outline of the thesis

Chapter 1 (Introduction): This is the introductory chapter of the thesis that explains the rationale, and objectives of this study, as well as illustrates the research problems, the research aims and objectives of the study.

Chapter 2 (Literature review): This chapter reviews recent literature that explains developmental trends for the detection of drugs and substances of abuse, particularly tramadol and alcohol, their mode of operations and application, electrode materials and their synthetic approaches, and description of electrochemical techniques employed in this study.

Chapter 3 (Materials Characteristics Methods): This chapter explains, illustrates, and demonstrates all methodologies for the physical and electrochemical characterizations employed in this study.

Chapter 4 (Electro-catalytic detection of tramadol): This chapter explains and discusses in detail the electro-catalytic detection of tramadol using the identified Nano-Carbons.

Chapter 5 (Electro-catalytic detection of Ethanol): This chapter explains and discusses in detail the electro-catalytic detection of ethanol using the identified Nano-Carbons.

Chapter 6 (Conclusions and Recommendations): This chapter deals with the conclusions drawn from the study results and recommendations therefrom.

1.5 References

1) S. S. Lim, T. Vos, A. D. Flaxman, G. Danaei, K. Shibuya, H. Adair-Rohani, et al. Lancet 2012, 380, 2224–2260.
2) J. Rehm, C. Mathers, S. Popova, M. Thavorncharoensap, Y. Teerawattananon, J. Patra. Lancet 2009, 373, 2223–2233.
3) R. Penning, J. Veldstra, A. P. Daamen, B. Oliver, J. C. Joris, Current Drug Abuse Reviews 2010, 3, 23-32.
4) K. I. Ozoemena, S. Musa, R. Modise, A. K. Ipadeola, L. Gaolatlhe, S. Peteni, G. Kabongo, Current Opinion in Electrochemistry 2018, 10, 82-87.
5) A. V. Tripkovi, K. D. Popovi, B. N. Grgur, B. Blizanac, P. N. Ross, and N. M. Markovi, “Methanol electrooxidation on supported Pt and PtRu catalysts in acid and alkaline solutions,” Electrochim. Acta, 2002, 47, 3707-3714.
6) J. Prabhuram and R. Manoharan, “Investigation of methanol oxidation on unsupported platinum electrodes in strong alkali and strong acid,” J. Power Sources, 1998, 74(1), 54-61.
7) A. S. Arico, V. Baglio, and V. Antonucci, Direct methanol fuel cells, 2010. New York: Nova Science Publishers. https://doi.org/10.1201/9781439833148. ch5
8) J. R. Varcoe, R. C. T. Slade, and E. Lam How Yee, “An alkaline polymer electrochemical interface: A breakthrough in application of alkaline anionexchange membranes in fuel cells,” Chem. Commun., 2006, 1428-1429.
9) J. R. Varcoe and R. C. T. Slade, “An electron-beam-grafted ETFE alkaline anion-exchange membrane in metal-cation-free solid-state alkaline fuel cells,” Electrochem. commun., 2006, 8, 839-843.
10) J. R. Varcoe, R. C. T. Slade, E. L. H. Yee, S. D. Poynton, and D. J. Driscoll, “Investigations into the ex situ methanol, ethanol and ethylene glycol

permeabilities of alkaline polymer electrolyte membranes," J. Power Sources, 2007, 173, 194-199.

CHAPTER 2

LITERATURE REVIEW

2.1 Rationale for the detection of tramadol and alcohol

For some years detection of drugs and substances of abuse (notably, tramadol and alcohol which are the main focus of this PhD project) had been undertaken by health workers, providers, Doctors, Pharmacists, Nurses, researchers, and government departments to determine causes of some unpalatable symptoms experienced by some patients, and to ascertain the actual drugs or substances of abuse being used by such patients to effectively diagnose and prescribe accurately for the treatment of the symptoms.

Sometimes public health units and departments undertake drug detections in areas where there are indications of environmental contamination sometimes from known drugs and substances of abuse (in their sources of water, in their soil, in the air etc) which by extension affects the health of the public to find interventions and mitigations in such occurrences. In recent times, societies have learnt to adopt preventive measures over and above curative interventions so, reasons or rationale for detecting drugs of abuse had extended beyond keeping the streams, ponds and sources of domestic water supply devoid of contaminants capable of causing danger to public health, the rationale for detecting drugs and substances of abuse has extended to over and above health professionals, police and other security agencies proactively and preventatively testing drivers, sportsmen and women, and citizens in general to identify illicit use of such drugs and substances on individuals which has critical undesirable effects not only on individuals but on society at large especially

as some of such drugs and their opioid and euphoric effects enable commission of social misdemeanours and violent crimes in the society.

Drugs of abuse such as tramadol (Figure 2.1) and alcohol (Figure 2.2) are prevalent in many countries including Africa and Asian countries. Tramadol exhibits an effect in patients similar to that of opioid agonists, and tramadol abuse just like opioids as indicated seem to be a problem on the rise for a number of countries. Over and above other violent crimes associated with the abuse of tramadol, the relationship between tramadol and sexual function appears to be controversially linked to its increasing abuse. It is recorded that men with premature ejaculation may benefit from taking tramadol off label; however, these patients live “on a knife's edge” and are more likely to develop other sexual dysfunctions and dependencies. According to the work done by Hamid *et al*. [1] on tramadol abuse and sexual function, the problem of tramadol abuse is controversially driven by the pursuit of the supposed sexual benefits as against the potential risks of tramadol on different sexual functions including ejaculation, orgasm, erection, desire, and testosterone levels.

Originally tramadol was never thought of being among abused substances and dependence potentials worldwide [1], however, recently in some African, Middle East, and West Asia countries it has become a serious issue. The 11 clinical trials conducted to evaluate tramadol benefit of premature ejaculation and were evaluated by 6 systematic reviews and 3 of which pooled data in a meta-analysis. Regarding abuse of tramadol for other sexual challenges such as low libido, erectile dysfunction, hypogonadism, and anorgasmia the evidence is inadequate.

Tramadol may be effective substance in treating premature ejaculation. Early studies had challenges namely, selection, allocation, or assessment bias. Over the years,

fields to research drug abuse are emerging. Clinical research is one of the fields and studies are carried out on the negative effects, dose, and safety of drugs. The off-label use of tramadol [2] which are in the increase costing the various countries heavily.

On the part of ethanol, alcohol is the favorite beverage all over the world. Society consumes it to have fun or stress reliever. However, regular consumption may put health condition susceptible to chronic problems such as cardiovascular diseases, cancer, and digestive tract conditions [3-5]. Moreover, over consumption of alcohol at a short space of time may lead to violence and accidents [6]. Road accidents due to alcohol is a trend that occurs each an every year, especially in South Africa during festive season. Africa follow the global pattern. In 2004, young African males between the age of fifteen to twenty-four years experienced a disability-adjusted life years due to alcohol. The nexus between alcohol and infectious diseases are general not recognized and/or poorly addressed in Africa. Rehm et al.,[7] estimated that there was an increase in infectious diseases attributed to alcohol by 50% in Africa. Despite the increasing evidence, most cities and nations neglect importance of risk factor of alcohol on the epidemics burden of infectious diseases such as HIV and Tuberculosis. Studies conducted in 2004 and 2010 by Rehm et al., [7, 8] assessed alcohol-related diseases and injuries around the world and identified conditions of contributing factor.

In closing, the negative impact of abuse of tramadol and ethanol (Figure 2.3) as indicated and its attributable injuries and disease burden in developing countries especially African nations is on the rise, hence confirming the relevance and importance of this study to develop more efficient, cost-effective methods of detection of these drugs. Various researchers such as [8,9], present the

epidemiological situation regarding alcohol as it relates to disease burden in Africa specifically giving details on alcohol exposure, and its impact on deaths and disability, using estimates from the World Health Organization (WHO) Global Health Estimates for outcome data and the WHO Global Status Report on Alcohol and Health (GSRAH) for risk relations. In addition, researchers present impact of ethanol abuse under different scenarios which include the impact of alcohol on HIV/AIDS incidence, economic costs of excessive alcohol consumption, alcohol abuse and dependence, excessive use of ethanol and impaired productivity, alcohol abuse and criminal justice system costs etc. [10]

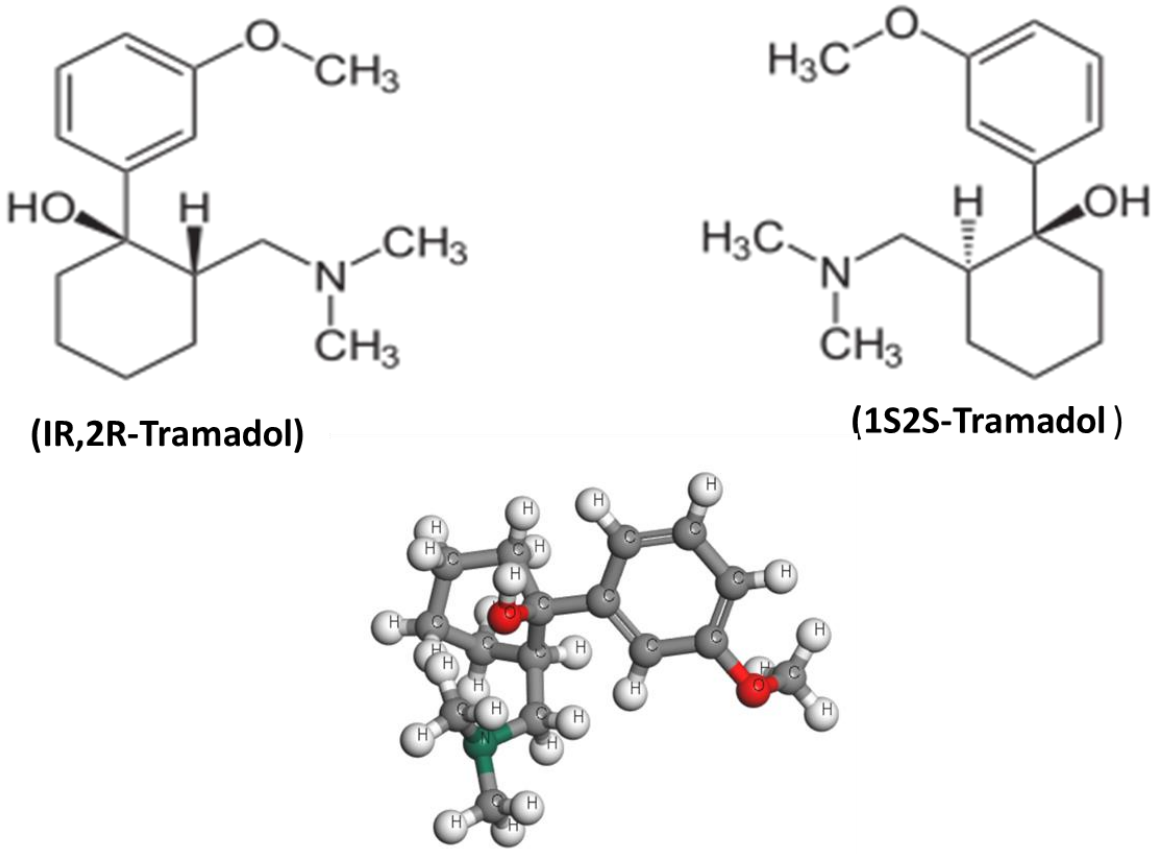


Figure 2.1: Isomeric structures of tramadol

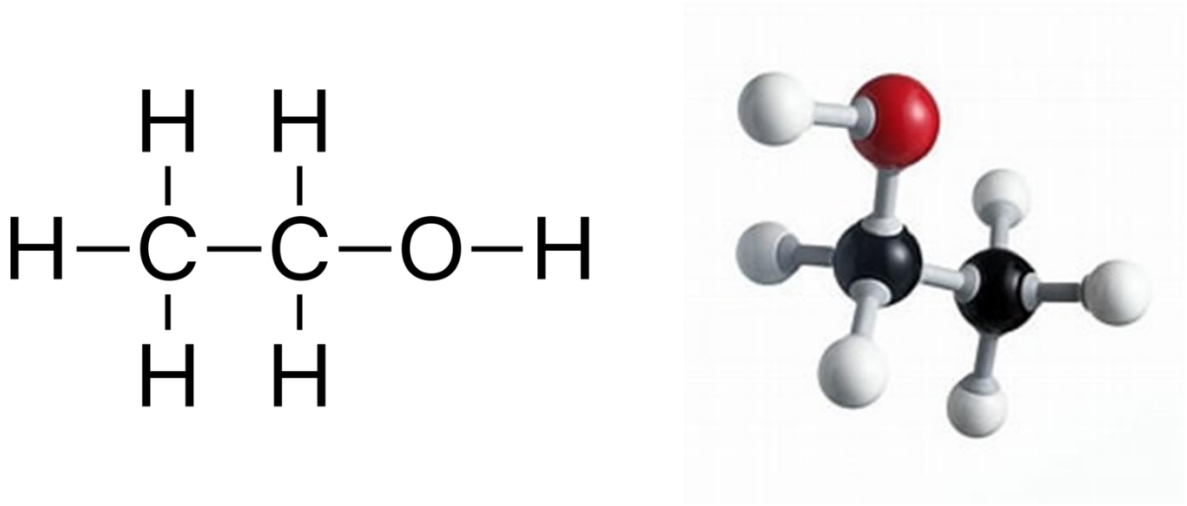


Figure 2.2 Chemical Structure of Ethanol



Figure 2.3 Pictures depicting faces of alcohol and drug abuse in the society (Courtesy: Bing images, assessed 15 March 2022)

2.2 Brief Overview of Current Detection Methods of Ethanol: Pros and Cons

There are various detection methods already on record, and in literature to have been used to detect tramadol such as UV-visible spectroscopy, Spectrophotometry, High-performance Liquid Chromatography (HPLC), mass spectroscopy, Electrochemistry. etc.

2.2.1 UV-Visible spectroscopy

UV-visible spectroscopy is a form of Absorption spectroscopy. Absorption spectroscopy in the UV-Visible region is to be one of the oldest and most frequently employed technique in pharmaceutical analysis for qualitative, quantitative, and structural analysis of a substance in solution. UV-Vis spectroscopy is a widely used technique in many areas of science ranging from bacterial culturing, drug identification and nucleic acid purity checks and quantitation, to quality control in the beverage industry and chemical research [11]. This article will describe how UV-Vis spectroscopy works, how to analyze the output data, the technique's strengths and limitations and some of its applications.

Light has a certain amount of energy which is inversely proportional to its wavelength. Thus, shorter wavelengths of light carry more energy and longer wavelengths carry less energy. A specific amount of energy is needed to promote electrons in a substance to a higher energy state which we can detect as absorption. Electrons in different bonding environments in a substance require a different specific amount of energy to promote the electrons to a higher energy state. This is why the absorption of light occurs for different wavelengths in different substances [12]. Humans are able to see a spectrum of visible light, from approximately 380 nm, which we see as violet, to 780 nm, which we see as red.[1] UV light has wavelengths shorter than that of visible light to approximately 100 nm. Therefore, light can be

described by its wavelength, which can be useful in UV-Vis spectroscopy to analyze or identify different substances by locating the specific wavelengths corresponding to maximum absorbance (see the Applications of UV-Vis spectroscopy section) [12-14].

2.2.2. Spectrophotometry

Spectrophotometry deals with measurement of the radiant energy transmitted or reflected by a body as a function of the wavelength. Here, the intensity of the energy transmitted is compared to that transmitted by some other system that serves as a standard [15,16]. It is a procedure often used for determining how much light is reflected by a chemical material by measuring the strength of light as a light beam travels through the sample solution.

2.2.3 Mass Spectroscopy

Mass spectroscopy, also referred to as mass spectrometry, is an analytic technique by which chemical substances are identified by the sorting of gaseous ions in electric and magnetic fields according to their mass-to-charge ratios. Simply put, mass spectroscopy separates the components of a sample by their mass and electrical charge [17,18]. The instruments used in such studies are called mass spectrometers and mass spectrographs.

2.2.4 High Performance liquid chromatography (HPLC)

High Performance liquid Chromatography was formerly referred to as High Pressure Liquid Chromatography. It is a technique in analytical chemistry used to separate, identify, and quantify each component in a mixture [19]. These existing techniques

employed for the detection of tramadol, alcohol and other drugs and substances of abuse have their advantages and disadvantages [20]. These techniques such as HPLC for instance used in the detection of tramadol exhibit the following:

(i) **Sensitivity** such that they can detect a very low concentration of tramadol.

(ii) **Selectivity**, in that they can selectively detect tramadol in the presence of impurities and interferents.

(iii) **Re-usability** such that they are stable enough to give the same results under similar conditions over time.

However, they are fraught with some critical drawbacks in that some are

(i) Cumbersome and not simple to use.

(ii) Requires a well-skilled personnel and technical know-how to operate.

(iii) Requires complicated set-up and does not allow on-site operation.

Yet, electrochemical techniques have been reported to be more sensitive, more selective and more cost-effective.

2.2.5 Electrochemical detection (Advantages & Disadvantages).

Electrochemical detection is a powerful analytical method that can detect electric currents generated from oxidative or reductive reactions in test compounds. Its variants had been utilized in the detection of tramadol recorded in literature [22]. Its design can be simple and compact allowing construction of portable devices [23]. This electro-analytical technique can be divided into different types of conductometric, potentiometric, voltametric and amperometric methods etc. Electrochemical detection method has its advantages and disadvantages. The

advantages of electrochemical detection method relative to other detection methods include:

- It has a low power requirement
- Linear output and good resolution
- High sensitivity and selectivity
- Excellent repeatability
- Wireless networking
- Simple, compact and can be constructed into a portable device.

The drawbacks of electrochemical detection methods include:

- Short lifespan
- Temperature fluctuation
- Possible cross-sensibility

2.2.6 Electrode materials

2.2.6.1 Onion-Like Carbon (OLC)

The Onion-Like Carbons (OLC) also referred to as Carbon Nano Onion (CNOs) or carbon onions are usually quasi-spherical nanoparticles made up of multi-layer concentric defective graphitic shells like multi-shell fullerene [33]. They are the latest discoveries of the carbon nanostructures which are currently very popular research in electrocatalytic analyses. They have properties different from other carbon nanostructures such as graphite [26, 34, 37, 41].

The defective interconnects between the shells allow for the intercalation of small ions and molecules. They have a large surface area, small particle sizes and are porous with hectohedral and hexahedral structures which are synthesized by very

high temperatures (annealing) into small fine structures of about 5 -10µm [1, 23, 26]. This OLC is thermodynamically more stable than graphene because it is characterized by a curved structure which creates strong strains that causes a hybridization with partials sp^3 character.

The myriad properties enable the OLC to be utilized in areas such as:

- Pharmaceutical drug delivery in the body.
- Bioimaging.
- Electrochemical sensing.
- Electromagnetic shielding.
- Electrical energy storage.
- catalyst (and catalyst support),
- cell imaging and selective sensing

The Figure 2.4 below shows the images of Onion Like Carbon.

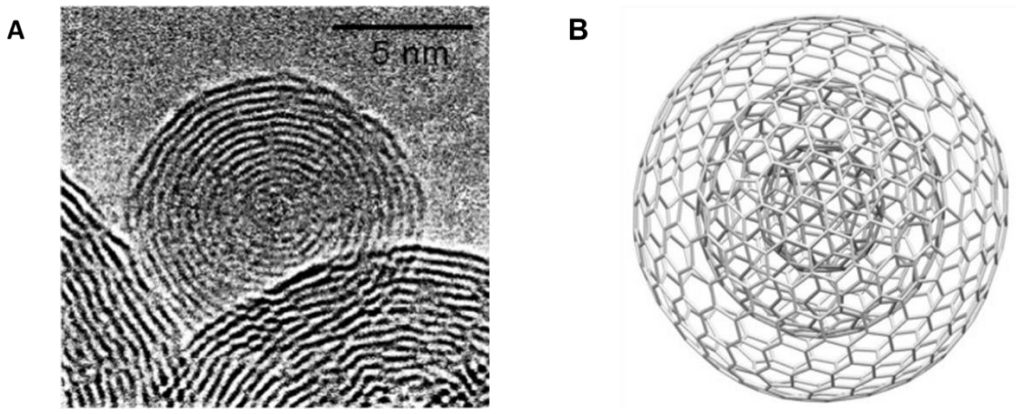


Figure 2.4 (A) HRTEM images of onion-like carbon (OLC) and (B) its structural representation. (Ugarte,1995).

2.2.6.2 Palladium Carbon on Carbon and Carbon-Ceria Supports as Catalysts

Palladium based materials have recently been explored as excellent electrocatalysts for anion membrane fuel cells (AMFCs) [23,24]. The configurative architectural design of the AMFCs is advantageously mimic for the detection of ethanol in this study. Platinum-based electrocatalysts have been exhaustively used and studied as catalysts for low temperature fuel cells, especially the direct ethanol fuel cell and in the preparation of sensors for detection of ethanol. However, the commercially available FC devices are too expensive and that could be traced to the use of bulk platinum (Pt) electrocatalysts to drive the reactions in acidic conditions.

The reaction at the cathode is of major concern in fuel cell and ethanol detection devices, as it is extremely sluggish and necessitated the use of high loadings of Pt electrocatalysts [38] as opposed to the anodic reaction, which is about five times faster than the reaction at the cathode, with very little loading of Pt [39]. Moreover, the Pt electrocatalyst is rarely readily available due to scarcity. Nanotechnology is one strategy that has been employed to minimize the cost of the Pt electrocatalyst and MEA for the fabrication of fuel cell or ethanol detection devices through electrocatalysis [29–31]. Nanotechnology has brought about research ideas to reduce the loading of Pt electrocatalysts (ca. 20 %). The utilization of various carbon supports to achieve this end has been variously reported [32]. Another strategy that has been employed in these electrocatalytic technologies is a replacement of the acidic media of operation with alkaline media [26] as electrocatalysts have shown great performance in alkaline media due to the impressive characteristics of alkaline media. Consequently, it became the interest of this research work to explore Pd-based carbon materials in alkaline conditions for the electrocatalytic detection of ethanol.

2.2.7 Tramadol and Ethanol

2.2.7.1 Tramadol

Tramadol is an opiate pain medication used in the treatment of moderate to moderately severe acute or chronic pain. It is metabolized in the human body by Cytochrome P2D6 (CYP2D6) enzymes to produce its therapeutic effects through its active metabolites, O-desmethyltramadol [35,36]. Tramadol is formulated in different dosage forms including tablets, powders, injections etc. Tramadol acts in the central nervous system (CNS) by binding to the μ-opioid receptor neuron and is also a serotonin-norepinephrine reuptake inhibitor. It is these actions on the CNS that make tramadol cause dependency effect leading to addiction which poses a potential danger to consumers and the society at large. This gives rise to the need to detect tramadol in its traces and control the same amongst individuals and in society [35,36].

2.2.7.2 Ethanol

Ethanol is an organic chemical compound. It is a simple alcohol with the chemical formula C_2H_6O. Its formula can be also written as $CH_3{-}CH_2{-}OH$ or C_2H_5OH, and is often abbreviated as EtOH. Ethanol is a volatile, flammable, colorless liquid with a slight characteristic odour [37]. When ingested in large quantity causes drowsiness, blurred vision, impairs concentration and may lead to addiction in humans. The abuse of alcohol leads to health hazards and is often linked to criminal activities and public insecurity including traffic offences. The Ethanol used in this work was absolute ethanol (ACS reagent, 99 % purity, and procured from MK Chemical).

2.2.8 Ferri-Ferrocyanide Solution.

Ferrocyanide/Ferricyanide often referred to as Ferri/Ferro is a redox reaction couple commonly used in electrochemistry as a mediator for shuttling electrons between electro -active species dissolved in a solution and a working electrode [39,40]. The working electrodes (WE) used for this particular work are glass carbon electrode (GCE) and screen plated electrode (SPE) modified with carbon nano-materials with a Platinum wire (PI) counter electrode (CE) and the varying current or voltage is measured with respect to reference electrode, Ag/AgCl.

2.2.9 Amstel Beer (4.0 % Alc)

This is an alcoholic beverage whose brand originated from Amsterdam but currently manufactured and marketed locally in South Africa. This beer contains 4.0% alcohol and we utilized this to run a comparative ethanol sensing in this Project.

2.2.10 Nederberg Wine (13.0 % Alc)

Nederberg wines is one of South Africa's largest and most prominent lines of wines produced in the country. It is located beneath the Drakenstein Mountains in Paarl, Western Cape and produces a wide range of wines from across the Western Cape, from classic South African varieties. For this Project the wine utilized contains 13.0% alcohol. It is employed as one of proof of concepts of sensing ethanol in commercial products, discussed in the later section of this work.

2.2.11 Interferents

These are chemical substances that are found in real samples such as serum, blood, urine and utilized to ascertain the selectivity of sensor(s) in distinctly detecting the various sample materials in the presence of such materials. The examples of

interferents are uric acid, citric acid, ascorbic acid, Sodium Chloride Potassium Chloride, Urea, Ammonium Sulphate, Calcium etc,

2.3 References

1) A. Abdel-Hamid, K. Andersson, M. D.Waldinger , T. H. Anis, “Tramadol Abuse and Sexual Function”, Sex Med Rev. 2016, 4: 235-246
2) J. A. Bumpus. “Low-Dose Tramadol as an Off-Label Antidepressant: A Data Mining Analysis from the Patients' Perspective”, ACS Pharmacol Transl Sci 2020, 29: 1293-1303.
3) S.S. Lim, T. Voss, A.D. Flaxman et al. “A comparative risk assessment of burden of disease and injury attributable to 67 risk factors clusters in 21 regions, 1990-2010: “A systematic analysis for the Global Burden of Disease Study 2010” Lancet 2012, 380: 2224-2260.
4) N. K. Morojeje, E. W. Dumbili, I.S. Obot, C.D.H. Parry. “Alcoholic consumption, harms and policy developments in sub-saharan Africa: The case for stronger national and regional responses”, Drug and Alcohol Review, 2021, 40: 402-419.
5) R.P. Ogeil, R.Room, S. Mathews, B. Lloyd. “Alcohol and burden of disease in Australia: the challenge in assessing consumption”, Australia and New Zealand Journal of Public Health, 2015, 39: 121-123.
6) J. Rehm, D. Ballunas, G.L.G. Borges *et al*. The relation between different dimensions of alcohol consumption and burden of disease – an overview. Addiction 2010, 105: 817-843.
7) J. Rehm, P.Anderson, F.Kanteres, C.D. Parry, A.V. Samokhvalov & J. Patra. “Alcohol, social development and infectious disease”. Toronto: Centre for Addiction and Mental Health. [ISBN number: 978-1-77052-444-6 (print)]:2009
8) V. Poznyak, A. Fleicshmann, D.Rekve, M.Rylett, J.Rehm, G. Gmel. The world health organization’s global monitoring system on alcohol and health. Alcohol

Res 2013, 35: 244-249.

9) K.D. Shield, C.Parry, J. Rehm.” Chronic Diseases and Conditions related to Alcohol use”. Alcohol Res 2014, 35: 155-171.

10) E. Bouchery; H. Hardwood; J. Sacks; Et al. Economic costs of excessive alcohol consumption in the u.s., 2006. American Journal of Preventive Medicine 2011, 41: 516-524.

11) T. Jiustin; UV-Vis Spectroscopy: Principles, Strengths and Limitations and Applications; by Technology Networks, Analysis and separations, https://www.technologynetworks.com/analysis/articles/uv-vis-spectroscopy-principle-strengths-and-limitations-and-applications-349865, June 2021.

12) J. Yu, H. Wang, J. Zhan, W. Huang. “Review of recent UV–Vis and infrared spectroscopy researches on wine detection and discrimination”. Appl Spectrosc Rev. 2018, 53: 65-86.

13) S. Behzadi, F. Ghasemi, M. Ghalkhani, et al. “Determination of nanoparticles using UV-Vis spectra”. Nanoscale 2015, 7: 5134-5139.

14) M. Picollo, M. Aceto, T. Vitorino. UV-Vis spectroscopy. Phys Sci Rev. 2018, 20180008

15) M.R. Sharpe. “Stray light in UV-VIS spectrophotometers”. Anal Chem. 1984, 56: 339A-356A.

16) O.C. Bosch, R.F. Sanchez. “Recent applications in derivative ultraviolet/visible absorption spectrophotometry: 2009–2011”. Microchem J. 2013, 106: 1-16.

17) A. Nakorchevsky, J.R. Yates. ”Biophysical Techniques for Structural Characterization of Macromolecules”. Comprehensive Biophysics, 2012.

18) R.F. Sánchez, O.C. Bosch. Recent development in derivative ultraviolet/visible absorption spectrophotometry: 2004–2008. Anal Chim Acta.

2009, 635: 22-44.

19) M.A. Hilal, K.M. Mohamed. “Simultaneous determination of tramadol and O-desmethyltramadol in human plasma using HPLC-DAD”. J Chromatogr Sci. 2014, 52: 1186-92.

20) A.J. Bard and L.R. Faulkner. “Electrochemical Methods: Fundamentals and Applications”. Russian Journal of Electrochemistry 2002, 38: 1364-1365.

21) E. Mynttinen, N. Wester, T. Lilius, E. Kalso, B. Mikladal, I. Varjos, S. Sainio, H. Jiang, E. I. Kauppinen, J. Koskinen, T. Laurila, Analytical Chemistry 2020, 92: 8218-8227.

22) H. Mahmoudi-Moghaddam, H. Beitollahi, S. Tajik, M. Malakootian, H. Karimi-Maleh, Environ. Monit. Assess. 2014, 186, 7431-7441; W. H. Elobeid, A. A. Elbashir, Prog. Chem. Biochem. *Res.* 2019, 2: 24-33.

23) K. I. Ozoemena, RSC Advances 2016, 6: 89523-89550.

24) A. K. Ipadeola, R. Barik, S. C. ray, K. I. Ozoemena, *Electrocatalysis* 2019, 10: 366-380.

25) A. Marshall, B. Børresen, G. Hagen, M. Tsypkin, and R. Tunold, “Hydrogen production by advanced proton exchange membrane (PEM) water electrolysers-Reduced energy consumption by improved electrocatalysis,” Energy, 2007, 32: 431-436.

26) H. A. Gasteiger, S. S. Kocha, B. Sompalli, and F. T. Wagner, “Activity benchmarks and requirements for Pt, Pt-alloy, and non-Pt oxygen reduction catalysts for PEMFCs,” Applied Catalysis B: Environmental. 2005, 56: 9- 35.

27) A. Mahata, A. S. Nair, and B. Pathak, “Recent advancements in Ptnanostructure-based electrocatalysts for the oxygen reduction reaction,” Catalysis Science and Technology. 2019, 9: 4835 – 4863.

28) S. Litster and G. McLean, “PEM fuel cell electrodes,” Journal of Power Sources, 2004, 130: 61-76.

29) M. S. Wilson, J. A. Valerio, and S. Gottesfeld, “Low platinum loading electrodes for polymer electrolyte fuel cells fabricated using thermoplastic ionomers,” Electrochim. Acta, 1995, 40: 355-363.

30) Z. Qi and A. Kaufman, “Low Pt loading high performance cathodes for PEM fuel cells,” J. Power Sources, 2003, 113: 37-43.

31) Leandro L. carvalho, Auro Tanaka, Flavio Colmati; “Palladium-platinum electrocatalysts for the ethanol oxidation reaction: comparison of electrochemical activities in acid and alkaline media”. Journal of Solid State Electrochemistry 2018, 22: 1471–1481.

32) K. I. Ozoemena, S. Musa, R. Modise, A. K. Ipadeola, L. Gaolatlhe, S. Peteni, G. Kabongo. “Fuel cell-based breath-alcohol sensors: Innovation-hungry old electrochemistry,” Current Opinion in Electrochemistry. 2018, 10: 82-87.

33) O.C. Ozoemena, N.S. Mathebula, T.J. Ehirim, T. Maphumulo, G. M. Valipke, J.L. SHAI, K. I. Ozoemena, Onion-like carbon re-inforced electrospun polyacrylonitrile fibres for ultrasensitive electrochemical immunosensing of Vibrio cholerae Toxin Electrochemica Acta. 2020, 356, 136816.

34) B. Yilmaz, A.F. Erdem. Simultaneous Determination of Tramadol and Its Metabolite in Human Urine by the Gas Chromatography-Mass Spectrometry Method. J Chromatogr Sci. 2015, 53: 1037-43

35) M.A. Hilal, K.M. Mohamed. Simultaneous determination of tramadol and O-desmethyltramadol in human plasma using HPLC-DAD.J Chromatogr Sci. 2014, 52: 1186-92.

36) E. D. Wang, J. B. Xu, and T. S. Zhao, “Density functional theory studies of the

structure sensitivity of ethanol oxidation on palladium surfaces," J. Phys. Chem. C, 2010, 114: 10489-10497.

37) H. A. Miller et al., "Highly active nanostructured palladium-ceria electrocatalysts for the hydrogen oxidation reaction in alkaline medium," Nano Energy, 2017, 33: 293-305.

38) M.Risch, K.A. Stoerzinger, T.Z. Regier, D.Peak, S.Y.Sayed, Y.Shao-Horn. "Reversibility of Ferri-/Ferrocyanide Redox during Operando Soft X-ray Spectroscopy". J. Phys. Chem. C. 2015, 119: 18903-18910.

39) D.Zehavi, J. Rabani. "Pulse radiolysis of the aqueous ferro-ferricyanide system. 1. Reactions of OH, HO2, and O2-radicals". J. Phys. Chem.1972, 76: 3703-3709.

40) S. J. Hendel, E. R. Young, "Introduction to Electrochemistry and the Use of Electrochemistry to Synthesize and Evaluate Catalysts for Water Oxidation and Reduction," J. Chem. Educ., 2016, 93, 11: 1951-1956

41) K. I. Ozoemena, S. Musa, R. Modise, A. K. Ipadeola, L. Gaolatlhe, S. Peteni, G. Kabongo, Current Opinion in Electrochemistry, 2018, 10: 82-87.

CHAPTER 3

MATERIALS AND METHODS

INTRODUCTION

The experimental and characterization techniques employed in this research are briefly summarised under this chapter. However, more information on the techniques and appropriate references are provided in chapters 4 and 5 that discuss in detail the results and discussion.

3.1 Chemical Reagents

The chemicals used in this work are listed in **Table 3.1**.

Table 3.5 Chemical reagents used in this work

Chemical Name	**Source**
Tramadol hydrochloride	Sigma Aldrich / Merck
Absolute Ethanol	MK Chemical
Potassium Hydroxide pellets	Association of Chemical Entrepreneur (ACE)
Detonated diamond particles	NaBond Technologies / Gelon, China
Carbon Black (Timical Super C45)	Gelon (China)
Human serum (Product #: H6914)	Sigma-Aldrich / Merck
Austell Tramadol capsule 50 mg, tramadol HCl 50 mg, AUSTELL South Africa; Batch No.: MG 20567; Exp: 08/2023	Local pharmacy
KH_2PO_4 and K_2HPO_4	Sigma Aldrich / Merck
$K_4Fe(CN)_6$ and $K_3Fe(CN)_6$	Sigma Aldrich / Merck
Dimethyl Formamide (DMF)	Sigma Aldrich / Merck

Nafion	Sigma Aldrich / Merck
Amstel Beer	SAB MILLER
Nederberg Wine	Nederberg Wine
Pure Nitrogen (N_2)	Afrox
Alumina Powder	Sigma Aldrich

3.1 Material Characterization

3.1.1 Powder X-ray Diffraction (PXRD)

The powder XRD is a rapid non-destructive analytical technique with the operation of constructive interference of monochromatic X-ray, employed basically to determine phases and structures of crystalline samples, giving crystallographic information of the crystalline materials [1-3].

3.1.2. Raman Spectroscopy

Raman spectroscopy is a non-contacting, non-destructive technique employed to obtain both qualitative and quantitative molecular information from a sample. It is used to characterize a material by its unique vibrational and crystallographic information, which is derived from the material's electronic states and photon energy dispersion. A Raman spectrum is obtained by exciting a sample with a laser. The inelastic scattering of photons from the vibrations within the molecules is then measured at low wave number resolution. It is performed at room temperature and ambient pressure [4-10]. Raman spectroscopy is very useful in the characterization of carbon nanomaterials such as OLC, CB e.t.c. (their detailed structure and configurations).

3.1.3 Scanning electron microscopy (SEM)

SEM was used to collect images of the samples. These images reveal information about the morphology and surface properties of each catalyst material [11]. It is a technique commonly used in the field of nanotechnology to visualize and examine nanoparticles and nanocomposites more closely. The procedure involves fixing a carbon tape to an SEM sample holder, and the sample (powdered) is sprinkled onto the carbon surface. A thin layer of platinum, gold, or carbon coating is then sputtered (≈100 Å) on the sample to ensure that the surface is conductive and not charging. This is a requirement for charging samples. The sample is then examined in a SEM chamber. Here, a fine beam of electrons is focused into a small probe which is used to scan over a sample. The interaction between the beam and the sample creates an emission of electrons and photons. The signals (back-scattered electrons, secondary electrons, transmitted electrons) emitted by the sample are observed on the detectors. The final product of the interaction of beams is the sample's image. A scanning electron microscope employs two image monitors. One monitor is used to observe the specimen and the other one is connected to a photo camera and is used to take images of the specimen.

3.1.4 Energy-dispersive X-ray spectroscopy (EDX)

EDX is employed for the identification of the elements in a given material sample. In other words, it is used for elemental analysis of the sample. The sample preparation for EDX is same as that of the SEM. It plays a complimentary role to the SEM analysis. (Page 29 highlighted)

3.1.5 Transmission electron microscopy (TEM) analysis

TEM is usually employed in the examination of the morphology of nanomaterials [12]. It helps to examine the microstructure of nanoparticles and nanocomposites.

TEM employs a nanometer-size electron probe with which it uniquely identifies and quantifies the structures of individual nanocrystals in a sample. TEM and SEM are similar, except that that the beam passes through the sample during TEM, while SEM studies the extrinsic structural morphology of the prepared Pd-based catalysts. Also, TEM can provide high-resolution images (up to 0.5 nm) of the samples from a high-powered beam of electrons accelerated at 120 kV to examine their intrinsic structural properties. In this research, a FEI Tecnai T12 TEM was used.

3.1.6 Thermogravimetric analysis (TGA)

The TGA is an analytical technique utilized with monitoring the weight changes of a material while the temperature is changed over time under a controlled temperature atmosphere [13]. This technique is used to analyze the thermal stability of a given sample. In this work, a Perkin Elmer Thermogravimetric analyzer (TGA)/Differential Thermogravimetric analysis (DTGA) 6000 was used for the TGA of the samples.

3.1.7 Brunauer-Emmett-Teller (BET) surface area analysis

Brunauer-Emmett-Teller (BET) analysis is employed to get this information about the specific surface area and porosity of materials. In this work, a Micromeritics TriStar II 3000 was used.

3.1.8 X-ray Photoelectron Spectroscopy (XPS)

XPS is a surface-sensitive analytical technique that provides information on quantitative atomic composition and chemistry. It identifies elements in a sample, as well as their chemical states [14]. In this work, the XPS facility used was the Thermo brand of ESCAlab 250Xi (monochromatic Al kα (1486.7 eV, x-ray power of 300 W, and spot size of 900 µm, pass energy (survey) of 100 eV, pass energy (hi-Resolution) 20 eV, and pressure of $<10^{-8}$ mBar).

3.2 Electrochemical Characterization Techniques

3.2.1 Cyclic voltammetry

This is a direct current (DC) electrochemical technique, which records the response in a current while a potential scan is applied to the working electrode at a constant scan rate in the forward and reversed directions, once or several times [15-17]. Cyclic Voltammetry (CV) is a standard technique used for determining the redox properties of a materials. It is the most popularly used electrochemical technique. In this technique, current signal is measured at a fixed potential range or window. It is used to acquire information about the properties and the characteristics of electrochemical process like the reversibility of a reaction, adsorption process, electron transfer kinetics, to determine the presence of intermediate in a redox reaction etc. The electrochemical equipment (potentiostat) is used to measure the current generated by the redox reaction, which is then plotted as current against applied potential, known as *Voltammogram*. In this process, the positive scan is the anodic (oxidation) process, while the backward scan is the cathodic (reduction) process. In general, the CV provides unique information about the redox properties of the material of interest such as reversibility or irreversibility, equilibrium potential, etc. This technique was used extensively in this PhD thesis (see Chapters 4 and 5 for detail).

3.2.2 Square wave voltammetry

This technique is a form of linear potential sweep voltammetry that uses a combined square wave and staircase potential applied to a stationary electrode. It has found numerous applications in various fields, including medicinal and various sensing communities, hence useful in the characterization of materials used in the detection of tramadol.

3.2.3 Differential pulse voltammetry (DPV)

Differential pulse voltammetry (DPV) (also differential pulse polarography, DPP) is a voltammetry method used to make electrochemical measurements and a derivative of linear sweep voltammetry or staircase voltammetry, with a series of regular voltage pulses superimposed on the potential linear sweep or stairsteps [15-17].

3.2.4 Electrochemical impedance spectroscopy

Electrochemical impedance spectroscopy (EIS) is a powerful analysis technique that helps to understand the electrode-electrolyte interfacial properties [16-18]. EIS helps to measure the electrical resistance during electrochemical reaction; measures the relationship between the imaginary part of the impedance (Z" or Zim) and the real part of the impedance (Z' or Zre). The plot of Z" versus Z' is called the Nyquist plot. The EIS parameters are usually obtained by fitting the experimental date with the electrical equivalent circuit, such as the Randles circuit shown below (Figure 3.3b). The Nquist plot (figure 3.3a) is a semi-circle at high frequency and a 45-degree rise at the low frequency region. From The Randles circuit (figure 3.3b), the Nyquist plot comprises resistance due to the electrolyte (R_s), resistance due to charge- or electron-transfer (R_{ct} or R_{et}), double layer capacitance (C_{dl}) and the Warbug impedance (Z_W) due to the diffusion of ions from the electrolyte to the electrode interface.

3.2.5 Chronoamperometry

This is an electrochemical technique in which the potential of the working electrode is stepped and the resulting current from faradaic processes occurring at the electrode (caused by the potential step) is monitored as a function of time. In this

work, chronoamperometric technique was used to measure current–time dependence of the concentrations of ethanol in electrolyte solution (see Chapter 5).

3.3 Evaluation of Electrochemical Sensor's Figures of Merit.

In this work, the electrochemical sensors of the glass carbon electrode (GCE), and screen-printed electrode (SPE) were modified with different nanomaterials and nanocomposites which were designed for the detection of tramadol and ethanol. The different modified electrodes were evaluated using the following criteria viz: sensitivity, limit of detection, limit of quantification, specificity studies, selectivity studies, and stability studies for possible application for use in real samples. These sensors showed good precision and accuracy as was recorded in the results section of this work. The different criteria used for the evaluation are discussed below:

3.3.1 Sensitivity

With sensitivity, the extent to which the true positive will not be missed is tested using the modified electrodes to test different substrates in a solution and making sure that the true positive is not overlooked. The sensitivity in other words is the measure of the degree to which the sensor can dictate the concentration of the test materials. The sensitivity of the modified electrodes used was tested for the detection of tramadol and ethanol respectively and each result was recorded according to their performance in the results section. This parameter is determined as the gradient or slope of the plots of current response to concentration of the analytes (tramadol or alcohol).

3.3.2 Limit of detection

Limit of detection (LoD) is an analytical expression used to determine the sensitivity of a given detection technique. LoD is the lowest analyte concentration likely to be

reliably detected by the sensor(s). It can also be defined as the lowest concentration of analyte that can be obtained which is statistically different from the blank sample at a given level of confidence. The (LoD) can be computed from the equation below:

$$LoD = \frac{3.0\delta}{m} \quad (3.1)$$

where δ, m and LoD are the standard deviation of the plot, the slope of the fitted plot of current from voltammogram against the analyte concentrations and limit of detection, respectively.

3.3.3 Limit of quantification

The term means the analyte is detected at its lowest concentration with precise and accurate quantification. LoQ is given in equation below.

$$LOQ = \frac{10\delta}{m} \quad (3.2)$$

where δ, *m* and LoQ are the standard deviation of the plot, the slope of the fitted plot of current from voltammogram against the analyte concentrations and limit of quantification, respectively.

3.3.4 Specificity / Selectivity

Specificity simply means the extent to which the electrochemical sensor can detect specific analyte irrespective of other interfering species.

3.3.5 Repeatability / Stability

The repeatability or stability of a sensor is its ability to be used repeatedly (over and over again) without a significant loss of activity or sensitivity.

3.4 References

1) R. Heimann and R. Heimann, “X-Ray Powder Diffraction (XRPD),” in The Oxford Handbook of Archaeological Ceramic Analysis, 2016. (https://dokumen.pub/the-oxford-handbook-of-archaeological-ceramic-analysis-oxford-handbooks-1nbsped-0199681538-9780199681532.html), May 2022
2) J. Lodge and J. P. Lodge, “X-Ray Powder Diffraction,” in Methods of Air Sampling and Analysis, 2018. https://www.amazon.in/Methods-Air-Sampling-Analysis-3rd/dp/0367457571, May 2022.
3) O. D. Neikov and N. A. Yefimov, “Powder Characterization and Testing,” in Handbook of Non-Ferrous Metal Powders, 2019, 3-62. https://www.sciencedirect.com/book/9780081005439/handbook-of-non-ferrous-metal-powders, May 2022.
4) D. D. Le Pevelen, “NIR FT-raman,” in Encyclopedia of Spectroscopy and Spectrometry, 2016, 98-109. https://www.elsevier.com/books/encyclopedia-of-spectroscopy-and-spectrometry/lindon/978-0-12-803224-4, May 2022.
5) P. S. Goh, A. F. Ismail, and B. C. Ng, “Raman Spectroscopy,” in Membrane Characterization, 2017, 31-46. DOI: 10.1016/b978-0-444-63776-5.00002-4
6) P. K. Chu and L. Li, “Characterization of amorphous and nanocrystalline carbon films,” Mater. Chem. Phys., 2006, 96, 253-277.
7) TUINSTRA F and KOENIG JL, “RAMAN SPECTRUM OF GRAPHITE,” J. Chem. Phys., 1970 53, 1126.
8) A. Ferrari and J. Robertson, “Interpretation of Raman spectra of disordered and amorphous carbon,” Phys. Rev. B - Condens. Matter Mater. Phys., 2000, 61.

9) A. C. Ferrari and J. Robertson, “Resonant Raman spectroscopy of disordered, amorphous, and diamondlike carbon,” Phys. Rev. B - Condens. Matter Mater. Phys., 2001, 64.

10) M. A. Pimenta, G. Dresselhaus, M. S. Dresselhaus, L. G. Cançado, A. Jorio, and R. Saito, “Studying disorder in graphite-based systems by Raman spectroscopy,” Physical Chemistry Chemical Physics. 2007,9, 1276-1290.

11) A. Ul-Hamid, A Beginners’ Guide to Scanning Electron Microscopy. 2018.

12) S. J. Pennycook et al., “Seeing inside materials by aberration-corrected electron microscopy,” Int. J. Nanotechnol., 2011, 8, 935 - 947.

13) W. M. Groenewoud, “Chapter 2 - Thermogravimetry,” in Characterisation of Polymers by Thermal Analysis, 2001, 61-76. https://www.sciencedirect.com/book/9780444506047/characterisation-of-polymers-by-thermal-analysis. Doi.org/10.1016/B978-0-444-50604-7.X5000-6.

14) H. Konno, “X-ray Photoelectron Spectroscopy (XPS),” Zairyo-to-Kankyo, 1993, 42, 27-36.

15) R.G. Compton, C.E. Banks, Understanding voltammetry, World Scientific 2018.

16) P.M. Monk, Fundamentals of electroanalytical chemistry, John Wiley & Sons 2008.

17) A.J. Bard, L.R. Faulkner, Electrochemical Methods: Fundamentals and Applications, 2nd ed., Wiley 2001.

18) M.E. Orazem, B. Tribollet, Electrochemical impedance spectroscopy, 2nd ed.2017.

CHAPTER 4

Comparative Electrocatalytic Oxidation and Detection of Tramadol on Carbon-Based Materials

Synopsis

This Chapter discusses the first interrogation of the possible application of nanodiamond-derived onion-like carbons (OLC), in comparison with conductive carbon black (CB), as carbon electrocatalysts for the detection of tramadol (an important drug of abuse). It is clearly proven that OLC exhibits excellent electrocatalysis towards tramadol compared to the CB counterpart. The physico-chemical properties of OLC and CB were determined using XRD, Raman, SEM, BET and TGA. The OLC exhibits, amongst others, higher surface area, more surface defects, and higher thermal stability than CB. Theoretical calculations (DFT simulations) predicts that the underlying science for the high performance of OLC is related to its weaker surface binding of tramadol (Ead = -26.656 eV) compared to the CB (Ead = -40.174 eV).

4.1 Introduction

The abuse of addiction drugs is one of the major global health challenges with tramadol (TR) regarded as one of the most abused drugs [1, 2]. TR belongs to the phenanthrene opium alkaloids and, albeit being a weak opioid, it is a strong pain-reliever and regularly used in the treatment of moderate to severe pain, especially in post-operative care [1, 3, 4]. TR hydrochloride is marketed as a racemic mixture of R- and S-stereoisomers, i.e., (1RS,2RS)-2-[(dimethylamino)methyl]-1-(3-methoxyphenyl)-cyclohexan-1-ol hydrochloride (**Figure 4.1**) [5, 6] because the two isomers strongly complement the analgesic properties of each other. Unlike conventional opioid-based analgesics, its mechanism of easing pain is somewhat different: it inhibits the re-uptake of norepinephrine and serotonin thereby increasing their release [7]. TR is an addictive drug that has become a menace in most countries including African countries such as Nigeria, Ghana, etc leading to wide ban in African countries [8, 9]. TR is regarded as relatively safe when used at the prescribed dosage. However, tramadol overdose or intoxication leads to high levels of tramadol in the blood and serious consequences such as cardiac complications and death [10, 11]. In addition, TR is being implicated as an environmental risk [12-14], especially in urban water pollution. High concentration of TR is required to achieve the therapeutic effect in patients. However, only 65 – 70% of the TR dosage is metabolized and absorbed by the body, while the remaining unmetabolized drugs (*ca.* 35%) is excreted in the urine which can find its way into the surface and underground water reserves [12-14].

Based on the above health and environmental challenges of TR, there have been consistent efforts amongst sensor researchers on developing simpler methods for rapid, sensitive and selective detection of TR in its pharmaceutical formulation

and human biological samples. The detection of opioids in patients' samples involves the use of standard techniques, notably the high-performance liquid chromatography (HPLC) [15], including the HPLC integrated with diode array detectors (HPLC-DAD) [4], or with mass spectrometer (HPLC-MS) [3, 16], solid-state electrochemiluminescence [17], and solid-phase extraction with UV-vis spectrophotometry [18]. These HPLC-based techniques are bulky and expensive techniques that require high-level expertise to perform. The need for fast and accurate detection of TR to curb the abuse has necessitated the intense exploration of the electrochemical techniques as viable alternatives [13, 19-33]. Electrochemical methods are associated with several advantages including low-cost, rapidity of detection, simplicity of operation with basic training skills, and ease of miniaturization for point-of-care usage.

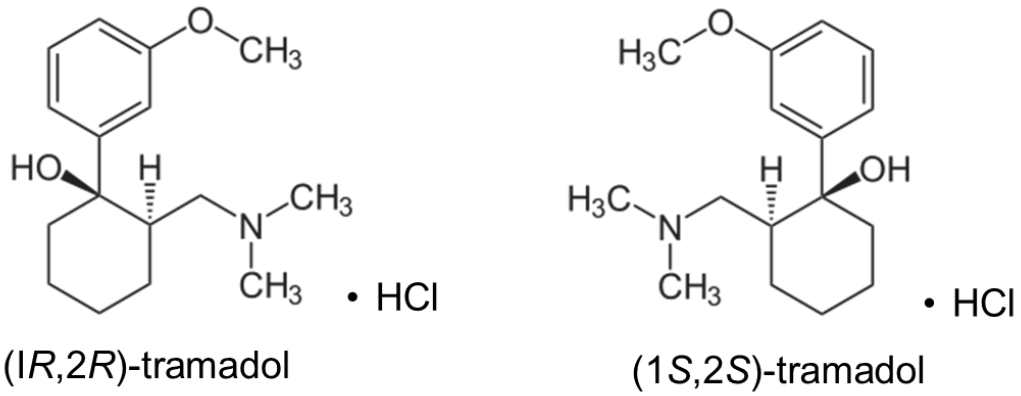


Figure 4.1 Isomeric structures of commercial tramadol hydrochloride

To date, carbon-based electrodes remain the most famous sensors for the detection of TR, which includes multi-walled carbon nanotubes (MWCNTs) [24], graphene modified with metal oxide [21], graphene oxide (GO) integrated with

MWCNTs [28], and carbon nanoparticles (CNP) [33]. These carbon materials have been reported to exhibit different sensitivity for electrocatalytic detection of TR. However, we are not aware of any report that provides a basic understanding on the possible reasons for the differences in the sensitivities.

In this work, we investigate the application of onion-like carbon (OLC) as electrocatalyst for tramadol and compare its performance with a well-known conductive carbon black (CB) (i.e., Super C45). In 2002, Keller and colleagues [34] were the first to publish the use of OLC as a catalyst for the synthesis of styrene. There are few reports on the use of OLC in electrochemistry, especially in the field of energy storage,[35-39] but its use in electrocatalysis has rarely been explored.[40-43] This work show OLC is a viable carbon catalyst for tramadol detection compared to the CB counterpart. Preliminary theoretical insights (DFT calculations) predict that the possible reason for the high electrocatalytic performance of the OLC is because the adsorption energy of tramadol onto the surface of OLC is weaker than on the surface of CB.

4.2 Experimental section

4.2.1 Materials, reagents and methods

Conductive carbon black (TIMICAL SUPER C45, 45 m^2/g) was obtained from Gelon, China, while OLC was synthesized from high purity (98–99%) nanodiamond powder (NaBond Technologies) by annealing in a muffle furnace at 1300 ^oC for 3 h in an argon atmosphere. All other reagents were of analytical grade and purchased from Sigma-Aldrich without further purification. Human serum (product number: H6914) was obtained from Sigma-Aldrich / Merck, while tramadol pharmaceutical formulation (Austell tramadol capsule 50 mg, tramadol HCl 50 mg, AUSTELL South

Africa; Batch No.: MG 20567; Exp: 08/2023) was donated from a local pharmacy store.

4.2.2 Physical property characterization

The powder X-ray diffraction "(PXRD) for OLC and CB were characterized using Bruker D2 Phaser (Cu-K_α X-rays at λ=1.5406 Å)" to investigate the extent of crystallinity. Morphology of the samples were established by Scanning electron microscopy (SEM). The specific surface areas of the samples were obtained with the Brunauer-Emmett-Teller (BET) method using the Micromeritics TriStar II 3000 area and porosity analyzer instrument. Raman spectroscopy (Bruker Senterra laser Raman spectrometer) was used to verify the extent of graphitization of the carbon. bond vibration. Thermal properties were investigated with the Perkin Elmer Thermogravimetric analyzer (TGA) / Differential Thermogravimetric analysis (DTGA) 6000. In a standard run, 10 mg of the samples were placed into a high-temperature alumina sample cup that was supported on an analytical balance located in the furnace chamber of the analyzer and the sample was heated in the air (5 °C min^{-1}) from 35 to 900 °C. Initially, the instrument uses nitrogen gas for purging (20 mL min^{-1}) while holding at 35 °C for 5 min.

4.2.3 Electrochemical detection procedure

Electrochemical measurements were conducted with the SP300 Bio-Logic Potentiostat (running on EC-Lab software). A three-electrode configuration was used: glassy carbon electrode (GCE, diameter 3.0 mm, 0.071 cm^2) modified with either OLC or CB ink as the working electrode, a platinum wire as the counter electrode, and a Ag|AgCl, 3 M KCl electrode as the reference electrode. Ultrapure

water of resistivity 18.2 MΩ cm was obtained from a Milli-Q Water System (Millipore Corp., Bedford, MA, USA) and used throughout for the preparation of solutions. Analytical grade KH_2PO_4 and K_2HPO_4 were used for the preparation of the phosphate buffer solutions (PBS, pH 7.4). The GCE was cleaned by proper polishing on a pad using alumina (Al_2O_3; nanopowder Aldrich) slurry followed by ultrasonic stirring in ethanol and acetone. The carbon ink was prepared by dispersing the powder (1 mg) in ethanol (1 mL) and adding 100 µL of Nafion (5 wt%) to increase the adhesion of the catalyst material on the GCE. The mixture was sonicated for 30 min to obtain a homogeneous mixture. The catalyst ink (10 µL) was then deposited on the GCE in a dropwise fashion and allowed to dry (**Figure 4.2**). Electrochemical impedance spectroscopy (EIS) experiments were carried out in the frequency range of 100 kHz and 10 mHz at an amplitude of 10 mV. Redox probe (3 mM $K_4Fe(CN)_6/K_3Fe(CN)_6$ (1:1 mol ratio) dissolved in 0.1 M KCl) was used to determine the charge-transfer kinetics of the GCE-immobilized carbon catalysts. The EIS was performed at an equilibrium potential ($E_{1/2}$) of the redox probe (0.15 V vs Ag|AgCl, 3 M KCl) as observed from prior cyclic voltammetry experiments. For real sample analysis (i.e., commercial tramadol capsules and in human serum), only OLC-modified screen-printed carbon electrodes (SPCE, DropSens) were used. The DPV parameters were 50 mV (pulse amplitude), 0.05 s (pulse width) and 0.2 s (pulse period).

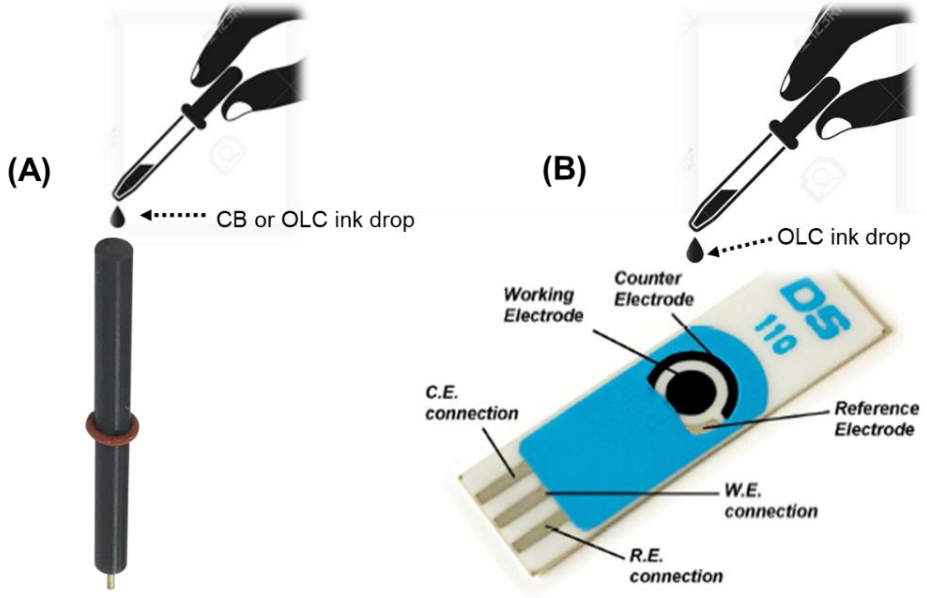


Figure 4.2 Electrode modification for tramadol electrocatalytic oxidation and sensing. The images are modified from the photographs obtained from electrode suppliers: (A) courtesy of BASi, copyright 2022; and (B) courtesy of Metrohm Dropsens, copyright 2022).

The modified electrodes (of GCE and SPE) were used to conduct the electrocatalysis and detection of TR drug samples (pure raw TR and pharmaceutical formulation). Prior to measurements of the TR, blank electrolyte scans were run several times until a stable background current was achieved. The DPV scans in PBS buffer solution were measured for several concentrations of the tramadol hydrochloride by successively injecting into the cell with a micropipette from a stock solution (0.5 nM TR). For the human serum measurements, the serum was diluted as 1:100 in PBS, and TR was injected from the stock solution.

4.2.4 Density functional theory (DFT) calculations

DFT simulations were performed at the super-computational facilities at the Centre for High-Performance Computing (CHPC, Cape Town, South Africa) using the BIOVIA Material Studio Suites and employing adsorption locator tool module. TR

was used as the adsorbate on both CB and OLC models. Supercells of 3 x 3 were modelled for carbon electrocatalysts, followed by geometric relaxation calculations with threshold energy set at 10^{-6} eV for convergence to be achieved. The modelled TR was cleaned using Material Studio cleaning tool, prior to its' adsorption. The minimum adsorption distance was set at 5 Å. DMol^3, another module of the BIOVIA Materials Studio, was used to calculate the electronic properties. The same threshold energy as that used for adsorption was set for the calculations of electronic and energy properties. Condensed-phase Optimization Molecular Potential for Atomistic Simulation Studies (COMPASS), forcefield was used since it guarantees reliable theoretical results.

4.3 Results and discussion

4.3.1 Materials characterization

Figure 4.3 shows the SEM images of (A) CB and (B) OLC, and the HRTEM image of the OLC. The SEM images show that CB comprises impure carbonaceous materials while the OLC is of high purity. The HRTEM images of the OLC clearly confirms its characteristic graphic concentric rings [39].

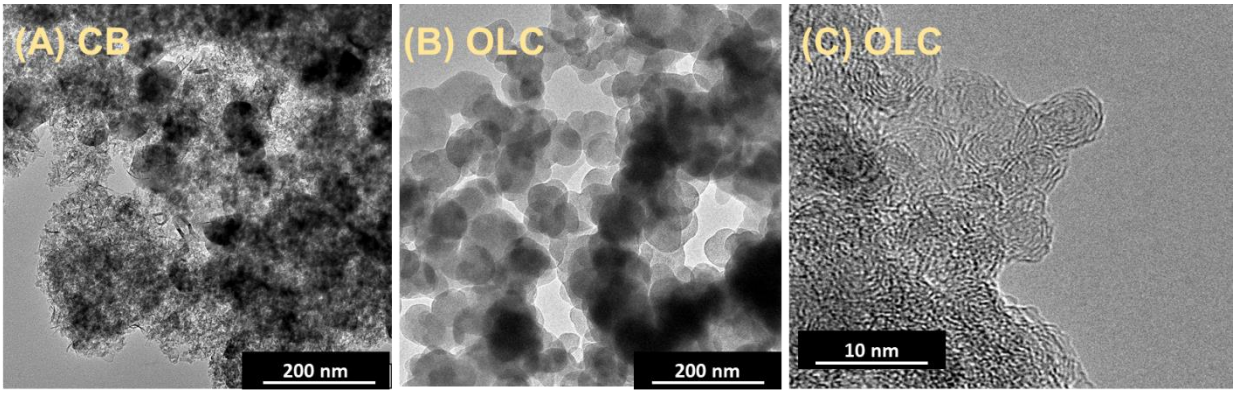


Figure 4.3 SEM images of (A) CB and (B) OLC, and (C) HRTEM image of OLC.

Figure 4.4 compares the XRD patterns (**Figure 4.4A**) and Raman spectra (**Figure 4.4B**) of the two carbon materials. The XRD patterns (Figure 2A) show broad diffraction peak centred at $2\theta = 25^{o}$ and a small diffraction peak at $2\theta = 3.2^{o}$, both of which are related to the (002) and (101) diffraction patterns of disordered carbon structure [44]. Structural information of CB and OLC was obtained with Raman spectroscopy (**Figure 4.4B**).

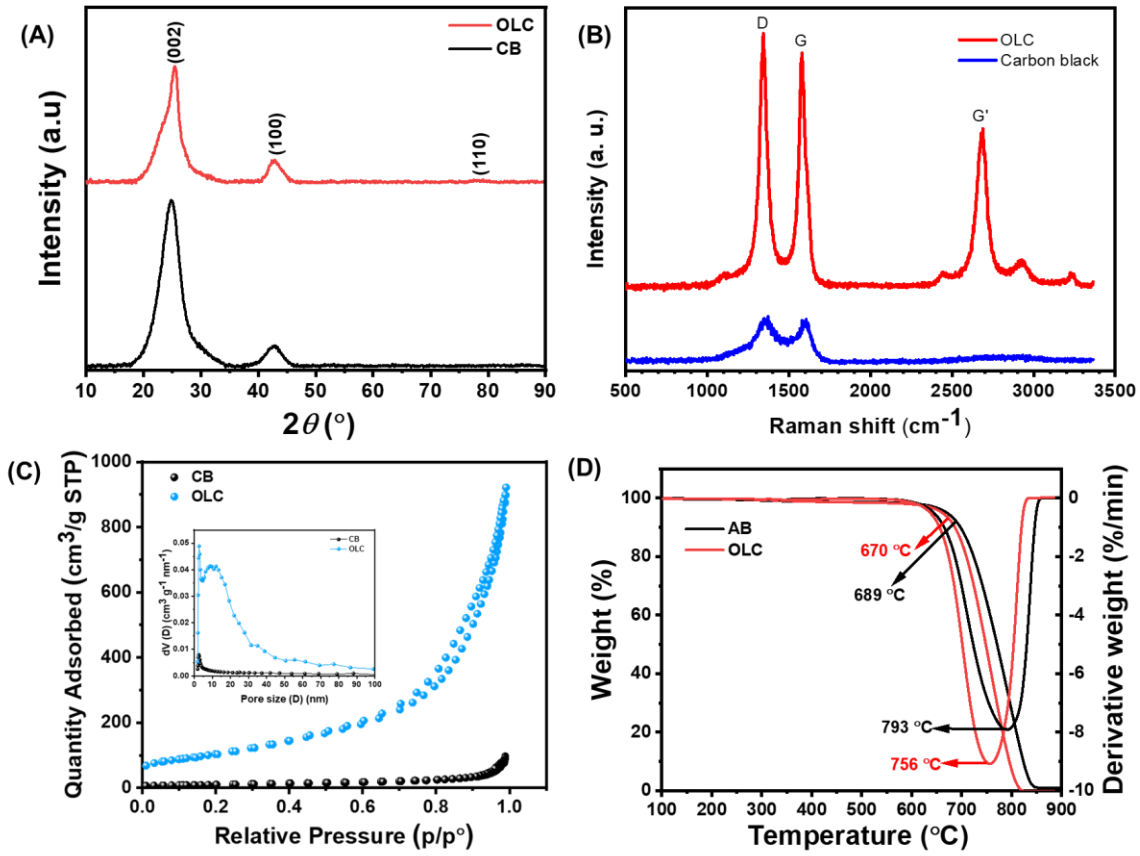


Figure 4.4 Comparing powder XRD (A), Raman spectra (B), BET adsorption desorption curve, and (inset) pore size distribution curves (C), and TGA and their corresponding derivative TGA (D) of OLC and CB.

The D band observed around the wavelength of 1350 cm^{-1} is due to the vibrations arising from the defect/disorder/amorphous carbon atoms (sp2-hybridized) while the G band observed around 1580 cm^{-1} is ascribed to the ordered/crystalline graphitic

carbon atoms (sp3-hybridized). The G' band observed at around wavelength 2700 cm^{-1} is due to the process of two-photon elastic scattering. The intensity ratio of the D and G bands (I_D/I_G) is used to determine the extent of defects or graphitization presents in the carbon materials; the higher the ratio, the higher the defects (lesser the graphitization). In addition, the higher the ratio of the IG'/IG, the higher the purity of the carbon [45-47]. The ID/IG values were estimated as 1.06 and 1.04 for the OLC and CB, respectively, meaning that OLC is slightly more defective than CB. The IG'/IG ratio for OLC was 0.76 while that of CB was zero, suggesting that OLC is of high purity while CB is mostly of poor quality. The porosity of CB and OLC were studied using N_2 adsorption-desorption measurements (BET). Specific surface area, pore volume and pore size are critical parameters for electrocatalysts.

Figure 4.4C compares the nitrogen adsorption-desorption isotherms and pore size distribution curves of CB and OLC. Both carbon materials exhibit type IV isotherms with type H3 hysteresis loops, indicating that they are essentially mesoporous materials (i.e., 2 – 50 nm). The BET surface areas (**Table 4.1**) of CB and OLC were determined as 35.6986 and 375.3579 m^2/g, respectively.

Table 4.1 Surface parameters CB and OLC materials.

Sample	Specific surface area, S_{BET} (m^2/g)	Pore volume, V (cm^3/g)	Pore size, D (nm)
CB	35.6986	0.1408	15.7771
OLC	375.3579	1.3888	14.7992

The specific surface area of OLC is more than 10 times higher than that of CB, confirming that OLC comprises much smaller nanoparticles than CB. The Barrett-Joyner-Halenda (BJH) approach was used to assess the pore size distribution of CB and OLC. A continuous pore size distribution within the range of 5–100 nm is observed, which is nearly in direct proportion to the pore diameter increase. The BJH method showed the pore diameter of CB and OLC ranging between 14.8 and 15.8 nm (see insert of **Figure 4.4C**), consistent with the mesoporous characteristics. Pore sizes smaller than 4 nm are due to mass loss arising from carbonization, while larger pore sizes (> 20 nm) are associated with the cavities in the carbon materials. The high specific surface area is important for enhancing the electrocatalytic properties of materials, thus one expects that OLC should provide better catalytic properties than the CB counterpart.

Figure 4.4D shows the thermal and derivative gravimetric analysis (TGA and DTGA) comparison of the CB and OLC. It is noted that the onset decomposition temperatures of CB and OLC were at 689 and 670 °C, respectively. The first order derivative peaks are centred at 793 and 756 °C for CB and OLC, respectively. Both CB and OLC are completely burnt with no weight retention, confirming the characteristic properties of carbon.

4.3.2 Cyclic voltammetry: mass transport and charge-transfer kinetics

Since this work has not been studied by anyone before, this work first sought to understand the cyclic voltammetric (CV) properties of the two carbon-based electrode in a solution of a redox probe. **Figure 4.5A &B** compare the CV evolutions of the bare GCE and GCE-modified with CB and OLC at 10 and 150 mV/s, respectively. **Table 4.2** summarizes the CV parameters of the electrodes, at the

smallest (10 mV/s) and highest (150 mV/s) scan rates. The CV evolutions at different scan rates for GCE-OLC (Figure 4.5C) and GCE-CB (Figure 4.5E) and their respective plots of peak current against square root of the scan rates (Figures 4.5D & F).

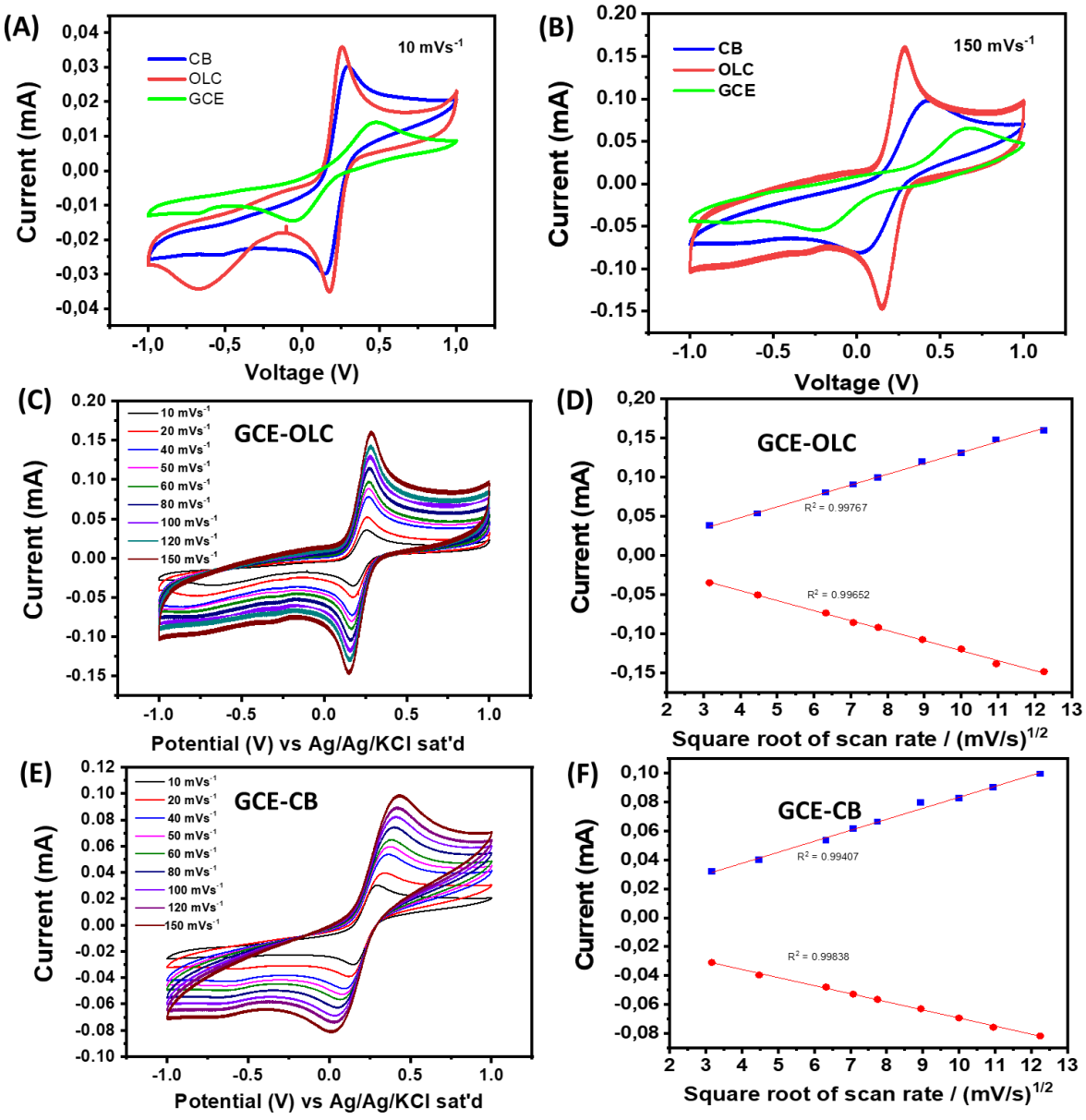


Figure 4.5 Cyclic voltammograms of the electrode at (A) 10 mV/s and (B) 150 mV/s; CV at different scan rates (10 – 150 mV/s) for the (C) OLC and (E) CB, and their corresponding plots of peak currents versus square root of scan rate (D) and (F), respectively. All data were collected in a redox probe ($[Fe(CN)_6]^{4-}/[Fe(CN)_6]^{3-}$ in 0.1 M KCl).

Table 4.6 CV parameters of the OLC- and CB-based electrodes obtained in a solution of redox probe.

CV Parameter	Bare GCE		GCE/OLC		GCE/CB	
	@ 10 mV/s	@150 mV/s	@ 10 mV/s	@150 mV/s	@ 10 mV/s	@150 mV/s
E_{pa} / V	0.460	0.674	0.260	0.292	0.301	0.437
E_{pc} / V	-0.063	-0.251	0.185	0.150	0.157	0.023
ΔE_p / V	0.523	0.925	0.075	0.142	0.144	0.414
$E_{1/2}$ / V	0.262	0.463	0.223	0.221	0.229	0.230
I_{pa} / mA	0.014	0.065	0.036	0.159	0.030	0.099
I_{pc} / mA	-0.015	-0.055	- 0.035	- 0.145	-0.030	-0.082
I_{pa} / I_{pc}	0.933	1.818	1.029	1.097	1.000	1.207

The current response at an electrode surface is the result of two inexorably intertwined processes: (i) the mass transport (i.e., the rate at which the analyte diffuses from the bulk electrolyte to the electrode surface), and (ii) charge-transfer kinetics (i.e., transport of electrons or ions across the electrode–electrolyte interface). The CV data reveal important electrochemical information with respect to mass transport and kinetics. First, the plot of peak current (for both anodic (I_{pa} / mA) and cathodic (I_{pc} / mA) versus the square root of scan rate ($\upsilon^{1/2}$ / $(mV/s)^{1/2}$) show

linear curves (R^2 > 0.99), which clearly confirms that the electrochemistry at these electrode platforms are diffusion-controlled processes in accordance with the conventional Randles-Sevcik theory. Note that slopes of the GCE-OLC is about twice that of the GCE-CB, meaning that diffusion is faster at the former than the latter.

At this juncture, it may be necessary to remind us that the current response from the surface of any porous electrode material (such as OLC) is a dual diffusion process, i.e., semi-infinite planar diffusion (of the analyte molecules towards the macro-electrode surface), and (ii) thin layer diffusion (i.e., small volume of analyte solution trapped in pockets within the porous structure)[48, 49]. Considering that both thin layer and adsorption effects also show linear dependence of log I_p vs log ν, it becomes somewhat difficult to distinguish between diffusion and adsorption phenomena, especially if the adsorption is rapidly reversible [48]. However, the value of the slope (*b*) of the log I_p vs log ν plot provides some insights: when b = 0.5 (pure diffusion process), when b = 1.0 (pure adsorption process), and when b > 0.5 but less than 1.0, it depicts a mixture of diffusion and adsorption process

es. In this work, the plot of log I_p vs log ν (for both anodic and cathodic) show linear curves (R^2 > 0.99, and with slopes ~ 0.55 for GCE-OLC, and ~ 0.4 for GCE-CB). These results show that the electrochemistry at the GCE-OLC is mostly diffusion-controlled while GCE-CB shows some resistive behaviour. Also, considering the high porosity of the of the OLC, thin layer diffusion cannot be ruled out. The inability to observe the adsorptive behaviour may be related to the weak or rapidity of adsorption of tramadol on the OLC surface (see discussion on DFT studies) compared to the CB.

Second, the ratio of the anodic-to-cathodic peak current (I_{pa}/I_{pc}) gives an insight into the electrochemical kinetics of the electrodes; if the ratio is unity, then the electrode is described as perfectly reversible. The two electrodes showed perfect reversibility ($I_{pa}/I_{pc} \approx 1$).

Third, the value of the peak-to-peak separation potential (ΔE_p / V) describes the extent of the electron-transfer kinetics; the smaller the ΔE_p value, the faster the rate of the electron-transfer, and vice-versa. From the CV data (Table 4.1), GCE-OLC exhibits much faster electron-transfer kinetics at small and high scan rates ($\Delta E_p \approx 75$ and 142 mV at 10 and 150 mV/s, respectively) compared to the GCE-CB counterpart ($\Delta E_p \approx 144$ and 414 mV at 10 and 150 mV/s, respectively). Fourth, the GCE-OLC showed higher current response (mass transport) than the GCE-CB counterpart. For example, at the 150 mV/s the current response at the GCE-OLC was 0.159 mA compared to the 0.099 mA for the GCE-CB. The result is attributed to the high specific surface area and high porous volume of the OLC compared to the CB, which corroborate the BET data.

Finally, the CV curves at different scan rates give further insight into the structural stability of the modified electrodes. It is observed that as the scan rate increased from 10 to 150 mV/s, both the anodic and cathodic peaks potentials of the GCE-CB shifted to the right by 136 mV (i.e., from 0.301 to 0.437 V) and left by 134 mV (i.e., from 0.157 to 0.023 V), respectively. On the other hand, the GCE-OLC only showed a very small shift (~ 32 mV) on the anodic peak potential (i.e., from 0.260 to 0.292 V) and ~ 35 mV shift on the cathodic side (i.e., from 0.185 to 0.150 V). This results clearly showed that the GCE-OLC the best structural and faster charge transport than the GCE-CB. In other words, the CB electrode exhibits sluggish electron transfer kinetics.

4.3.3 Electrochemical Impedance Spectroscopy: Charge-Transfer Kinetics

EIS is very important in understanding the redox properties of an electrocatalyst, which explains its wide application in various areas of electrochemistry. Figure 4.6 compares the EIS data obtained in the redox probe using the two carbon-based electrodes.

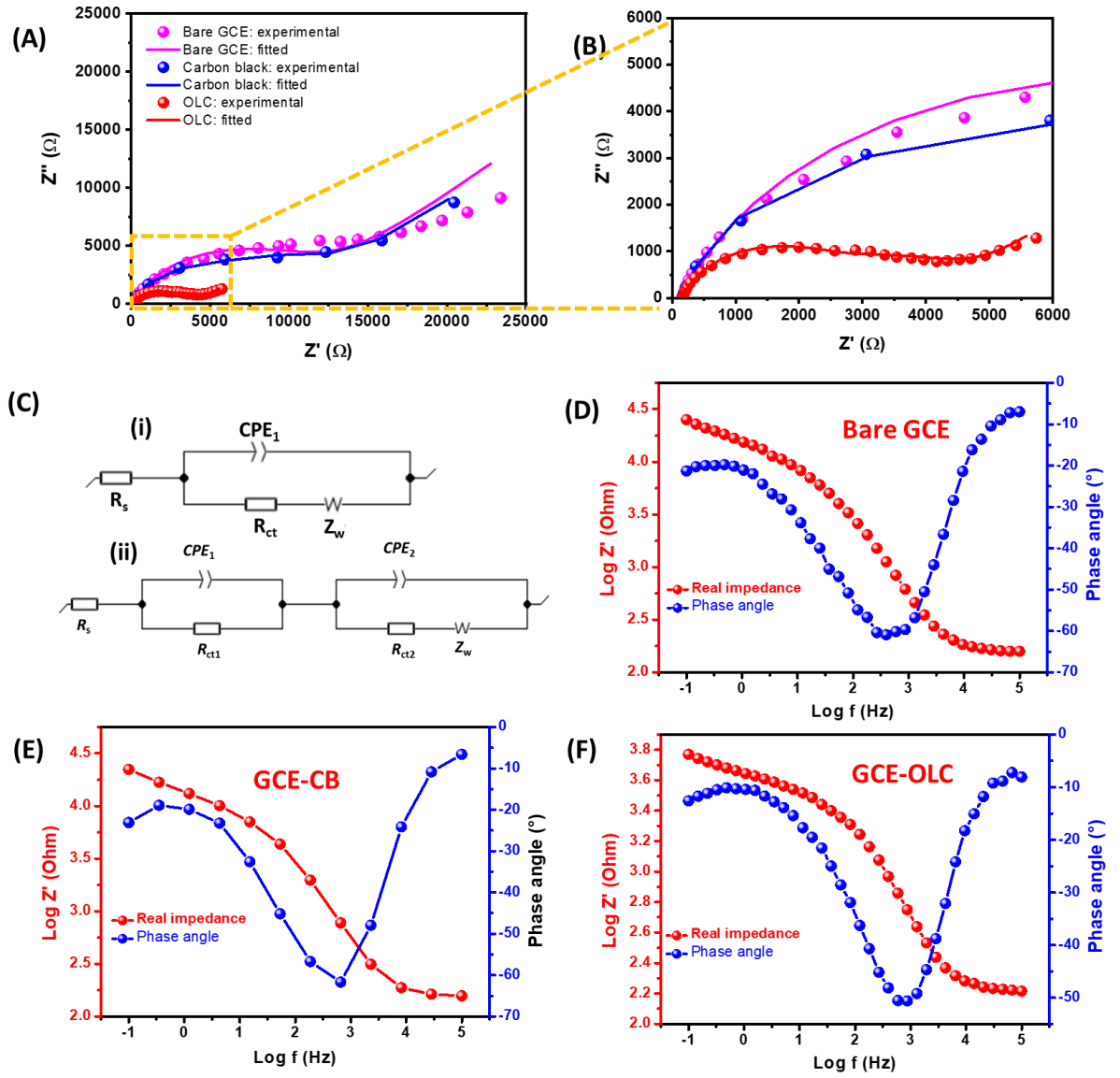


Figure 4.6 (A) Nyquist plots and (B-D) Bode plots of the GCE, GCE-OLC and GCE-CB. Data points are experimental, while lines are fitted data using the electrical equivalent circuit (inset in Figure 6A). All data were collected in redox probe ([Fe(CN)6]4−/[Fe(CN)6]3−) in 0.1 M KCl.

The electrodes were satisfactorily modelled with a coupled RC-Randles circuit (i.e., with ion-diffusion/Warburg region). The modelled parameters comprise the electrolyte resistance (R_s), the interfacial resistance (R_{int}) arising from the IR drop and the corresponding non-ideal capacitance of the interfacial layer or constant-phase element (CPE_1), the charge-transfer resistance (R_{ct}), and its corresponding constant-phase element (CPE_2) due to surface heterogeneity or irregularities of the electrode surface, and the Warburg diffusion impedance (Z_w) due to resistance to ion-diffusion process.

The impedance of the CPE (ZCPE) is defined as **Equation 4.1** [44, 50-54]:

$$Z_{CPE} = \frac{1}{Q(jw)^n} \quad (4.1)$$

where Q is a constant associated with the electrode/electrolyte interface, j = $\sqrt{-1}$, ω is the radial frequency, while the exponent n represents the slope of the plot of log Z against log F (i.e., Bode plot). The values of n range between -1 and + (i.e., $-1 \leq n \leq 1$: when n = 0, the CPE is a perfect resistor; when n = 1, the CPE is a pure capacitor; when n = −1, the CPE is an inductor; and when n = 0.5, the CPE is equivalent to the Warburg impedance (Z_w). From **Table 4.3,** the total series resistance ($R_s + R_{int} + R_{ct}$) decreases as follows: GCE (15.076 kΩ) > GCE-CB (12.924 kΩ) > GCE-OLC (4.696 kΩ), meaning the electron transfer at the OLC-based electrode is more than 4 times faster than at the CB and GCE. This result corroborates the CV data (see Table 2 for the values of the ΔE_p). The appearance of the CPE in the modelling indicates that the electrode surface is rough and porous. The “n” values (n1 and n2) of the CPE range between 0.77 and 0.88, implying that these electrocatalyst materials exhibit mixed mechanism of pseudocapacitance. Finally, the Z_w value increased as follows:

GCE-OLC << GCE-CB < GCE, which indicates that the GCE-OLC allows for faster ionic diffusion than the GCE-CB, which perfectly agrees with the CV data of peak current vs square root of the scan rate.

Table 4.7 EIS parameters for the GCE, GCE-CB and GCE-OLCs.

EIS Parameter	Bare GCE	GCE-CB	GCE-OLC
R_s / Ω	145.40 ± 0.32	152.50 ± 0.21	158.5 ± 0.36
CPE_1 / $\mu F.s^{(n-1)}$	2.06 ± 0.02	1.321 ± 0.026	1.842 ± 0.038
n_1	0.79	0.87	0.83
R_{int} / Ω	-	4394 ± 76	2363 ± 35
CPE_2 / $\mu F.s^{(n-1)}$	-	6.286 ± 0.038	38.83 ± 0.01
n_2	-	0.81	0.77
R_{ct} / Ω	11732 ± 1.83	8377 ± 106	2174 ± 29
i^o / A	2.2×10^{-7}	3.1×10^{-6}	1.2×10^{-5}
k_{het} / cm s^{-1}	3.2×10^{-11}	4.49×10^{-10}	$1,73 \times 10^{-9}$
Z_w / Ω $s^{-0.5}$	9358 ± 1	6803 ± 6	952 ± 2

EIS data throws more light on the reversibility of the redox processes, by calculating the exchange current (i_0) and rate constant of the heterogeneous electron transfer (k_{het}) using **Equations 4.**2 and 3 [55-57]:

$$i_0 = \frac{RT}{nFR_{ct}} \quad (4.2)$$

$$k_{het} = \frac{i_0}{nFA} \quad (4.3)$$

where A is the geometric surface area of the electrode, R is the gas constant (8.314 J K^{-1} mol^{-1}, T is the Kelvin temperature (298 K), n is the number of electrons transferred, while F is the Faraday constant (96,485.33 C mol^{-1}). The higher the values of i_0 and k_{het} the better the electrocatalysis. Both the i_0 and k_{het} decreased as follows: GCE-OLC > GCE-CB > GCE, which clearly corroborates that the electron transport of GCE-OLC is about a magnitude faster than that of GCE-CB, with the bare GCE exhibiting sluggish electron transport.

4.3.4 Electrocatalytic detection of tramadol

Figure 4.7A compares the CV evolution of the three electrodes in the PBS (pH 7.4) containing 0.5 mM of TR, showing that the peak current responses decrease as GCE-OLC (0.157 mA) > GCE-CB (0.028 mA) > GCE (~ 0.0). This result means that the GCE-OLC depicts exceptional current response compared to the GCE-CB counterpart. **Figure 4.7B** then compares the current responses of the GCE-OLC in the absence and presence of TR, which clearly proves that the response observed in Figure 7A is indeed due to the oxidation of TR. Important electrocatalytic information can be obtained from CV at different scan rates. **Figure 4.7C** shows the effect of different scan rates (10 – 150 mV/s) on the current response at a given TR concentration (0.5 mM). Following the equation for a totally irreversible anodic diffusion-controlled process, a plot of peak potential vs log scan rate is obtained (**Figure 4.7D**).

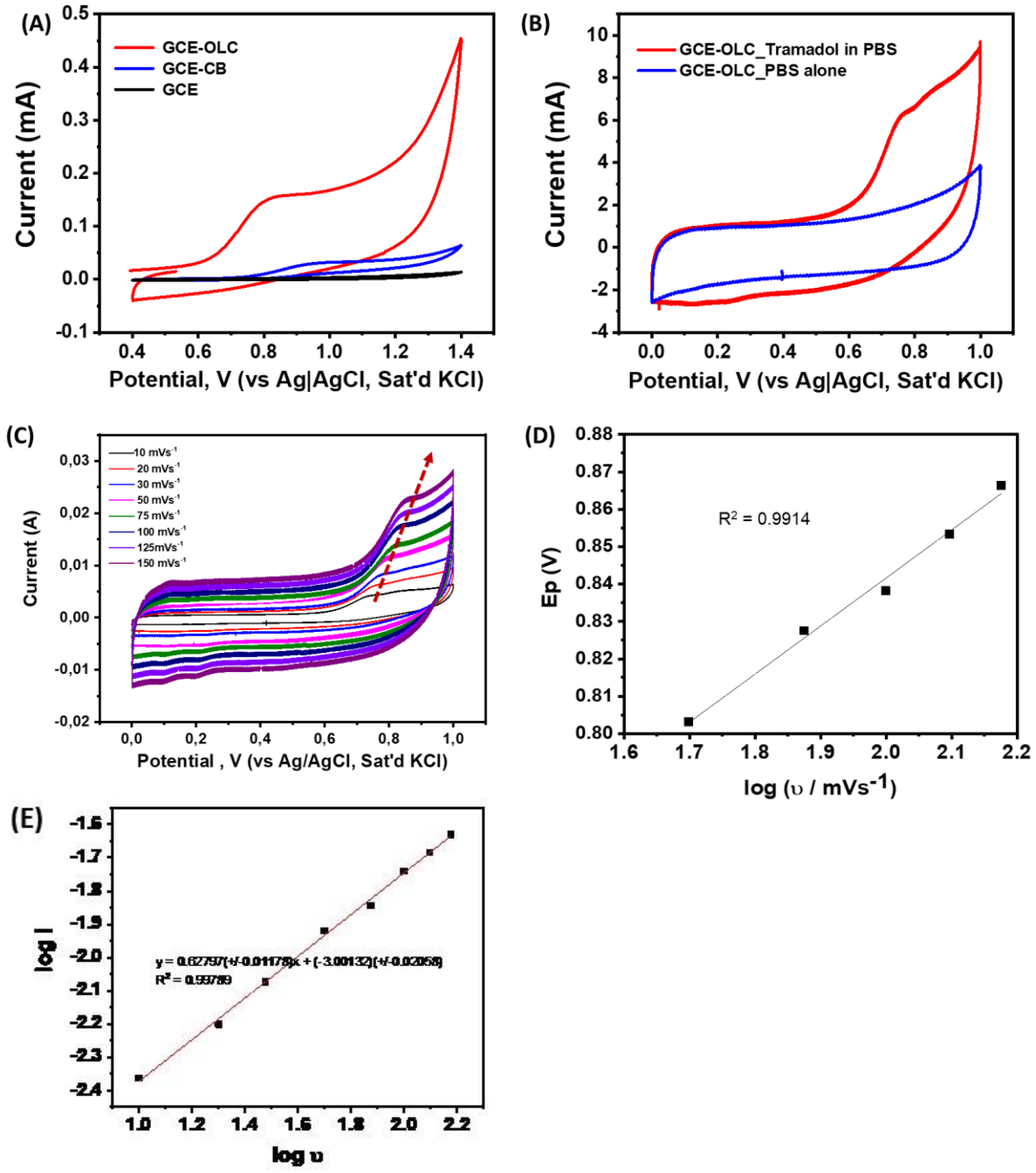


Figure 4.7 (A) CV evolutions of the GCE, GCE-CB and GCE-OLC in PBS (pH 7.4) containing 0.5 mM tramadol at 20 mV/s, (B) Comparing the CVs of GCE-OLC in PBS alone and PBS containing 0.5 mM tramadol at 20mV/s, (C) CV evolution showing the effect of changing scan rates on the current responses, (D) plot of peak potential versus log scan rate. All data acquired in PBS containing 0.5 mM tramadol. (E) plot of the log oxidation peak current vs log scan rate

The excellent linearity of the plot (correlation coefficient, R^2 = 0.9951) (**Equation 4.4**) is indicative of diffusion-controlled process.

I_p / A = 0.0667 log ($\upsilon^{1/2}$ / Vs^{-1}) - 0.0030 R^2 = 0.9951 (4.4)

From the CV evolutions (Figure 4.7C), the logarithmic plot of the oxidation peak current vs log scan rate (see Figure 4.7E and Equation 4.5) is linear, with slope of ~ 0.63 indicating mixed diffusion- and adsorption-controlled processes. Also, it is observed that when scan rate increases the peak potential (Ep / V) shifts slightly to the positive direction. The plot of Ep / V against the log υ (for scan rates of 50 – 150 mVs-1) showed a linear behaviour according to **Equation 4.6**:

log (I_p / A) = 0.628 log (υ / mVs^{-1}) - 3.00 R^2 = 0.9979 (4.5)

E_p / V = 0.129 mV log (υ / mVs^{-1}) + 0.585 R^2 = 0.9914 (4.6)

This behaviour agrees with the conventional equation for an irreversible anodic process (**Equations 4.7** and **4.8**)[58-61]:

$$E_p = \frac{b}{2}\log \upsilon + Constant \quad (4.7)$$

where,

$$b = \frac{2.303RT}{(1-\alpha)n_\alpha F} \quad (4.8)$$

where b/2 equals the slope of the plot (while *b* = Tafel slope), α is the transfer coefficient, n_α is the number of electrons involved in the rate-determining step (rds) of the electrode process, F is the Faraday constant, R is the gas constant and T is the absolute temperature. From the Tafel slope (i.e., b = 0.258 mV), $(1 - \alpha)n_a$ value is ~ 0.23. Assuming the one-electron mechanism in the rds (i.e., n_α = 1), the α is ~ 0.77 indicating that the activation free energy curve for an irreversible oxidation process for tramadol is asymmetrical.

4.3.5 Predicting the High Electrocatalytic Activity of OLC Over CB Towards the Detection of Tramadol: DFT Calculations

The excellent electrocatalytic performance of OLC towards the detection of TR raises an important question of *"why is OLC better than CB?".* To answer this critical question, we adopted the use of DFT to assist in predicting the interaction of TR with OLC vs CB. This is an important development as many researchers have used different carbons to detect TR but, to our knowledge, there is no report as to the reason why some carbons are better than others. Thus, this work attempts to fill this knowledge gap.

Figure 4.8 is the schematic representation of the carbon models used to predict the interaction of OLC and CB with the TR molecule. Using the Nanotube Modeler Software®, OLC was modelled as fullerene (spherical species) while the CB was modelled as flat molecules (i.e., multi-layers of graphene). From the isosurface potential, oxygen has higher negative potential (blue shades) compared to nitrogen (red shades), meaning that likely sites of tramadol interaction is dominated by oxygen. In the DFT calculation, the adsorption energy, E_{ad} (eV), is defined as (**Equation 4.9**) [43, 62, 63]:

$$\boldsymbol{E}_{ad} = (\boldsymbol{E}_{surface + adsorbate}) - (\boldsymbol{E}_{surface} + \boldsymbol{E}_{adsorbate}) \qquad (4.9)$$

where $\boldsymbol{E}_{surface + adsorbate}$ represents the total energy of the interacting catalyst surface and the adsorbate, while $\boldsymbol{E}_{surface} + \boldsymbol{E}_{adsorbate}$ are the energies of the bare catalyst surface and the free adsorbate in the gas phase. This equation shows that the more negative the $\boldsymbol{E}_{ad}$ value, the stronger the adsorption. The best performing electrocatalyst should possess the weakest adsorption strength ($\boldsymbol{E}_{ad}$ / eV) with the TR molecule. According to thermodynamics, the more negative the ΔG value, the weaker the interaction of the adsorbate on the surface of the catalyst.

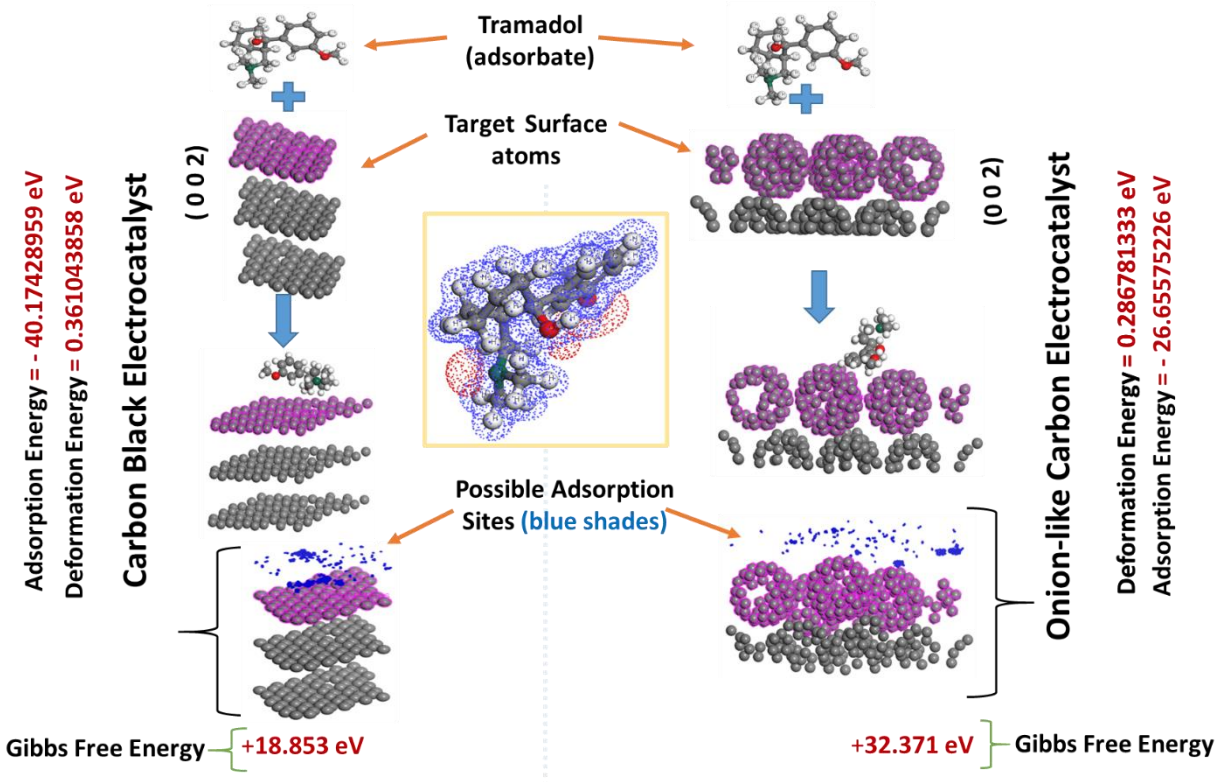


Figure 4.8 Adsorption sites of tramadol at the surfaces of CB and OLC. The dark blue dots (shades) show the possible site tramadol molecules are adsorbed. Inset is used to determine the isosurface potentials of tramadol @+/- 0.05181 isovalue(a.u.), for tramadol molecule.

Table 8.4 Predicted energy values from the DFT calculations accompanying the interaction of tramadol with the surfaces of OLC and CB.

Catalyst	Adsorbate	ΔG (eV)	E_{ad} (eV)	E_{def} (eV)	E_f (eV)	E_g (eV)	K.E. (Ha)
CB	n/a	n/a	n/a	n/a	- 6.838	0.008	-273.973
	Tramadol	18.853	- 40.174	0.361	- 6.838	0.002	-305.322
OLC	n/a	n/a	n/a	n/a	- 6.842	0.123	-124.389
	Tramadol	32.371	- 26.656	0.2868	- 6.831	0.121	-155.815

Key: ΔG = Gibb free energy; E_{ad} = adsorption energy; E_{def} = deformation energy; E_f = Fermi energy; E_g = energy band gap; K.E. = kinetic energy; n/a = not applicable

The DFT results (summarised in **Table 4.1)** show the E_{ad} and ΔG give the least negative values for the OLC-tramadol complex. Weak adsorption of adsorbate is most preferred in electrocatalysis, thus the weaker adsorption of TR onto OLC compared to CB predicts better electrocatalysis on OLC than on CB.

It is well known that graphene (single layer of graphite) is far more conducting that the fullerene and even carbon nanotubes. Thus, the smaller energy band gap (high conductivity) of the conductive CB (0.008 and 0.002 eV) than the OLC (0.123 and 0.121 eV) should be expected. The flat CB makes it easy for it to deform than the curved OLC, thus easy misalignment of p-orbitals of carbon atoms, meaning that the carbon atoms on the outside walls of the CB exhibit more sp3 nature than those carbons on the OLC (this is evident in the PDOS and Raman). Considering that the pi-pi interaction between the carbon atoms of TR and the adjacent carbon atoms of the OLC strengthens the deformation of the OLC, it simply means that a more stable deformation does not promote the overlap between the different pi-wave functions, thus the weakening the adsorption of TR molecule onto OLC. DFT predicts that CB exhibits properties inimical for electrocatalysis; a more metallic character (low Eg) and slower kinetics with tramadol than OLC.

To understand the electronic properties of TR on the carbon materials, before and after the adsorption process, DFT calculations on the electronic band structures and the projected density of states (PDOS) were carried out (**Figure 4.9**). Prior to adsorption of the TR molecule onto each of the carbon materials, both the band structure and PDOS show lower number of states than when TR is adsorbed onto the carbon catalyst. In other words, more electrons are available on the CB-tramadol and OLC-tramadol complexes than on the bare CB or OLC. Unlike the OLC that

shows a change in the Fermi energy value upon interaction with TR, the CB did not show any change. Note that upon the interaction of the TR molecule with the OLC catalyst, there is a mismatch in Fermi levels (E_f) that leads to the charge-transfer. This charge-transfer process leads to a redistribution of partial charge, which enhance the reactivity of the OLC over its CB counterpart.

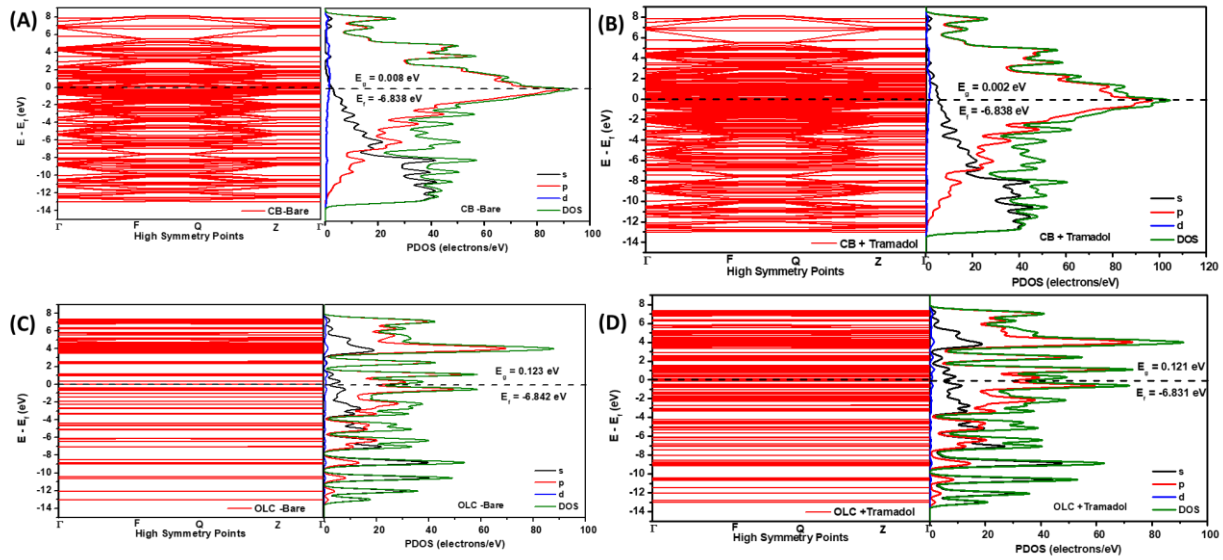


Figure 4.9 Band structures and PDOS for tramadol adsorbed on (A,B) CB and (C,D) OLC electrodes.

4.3.6 Analytical application of OLC-based electrochemical sensors

4.3.6.1 Determination of raw tramadol in PBS (pH 7.40)

Figure 4.10 shows typical concentration studies with SWV using both GCE-OLC (**Figure 4.10A**) and its corresponding linear calibration curve (**Figure 4.10B**). The near-vertical curve of the blank suggests some resistivity in the electrolyte under the experimental conditions, but this was somewhat suppressed in the presence of the tramadol drug. Expectedly, this explains one of the reasons why the linear curves could not start from the zero origin. Six replicate measurements were run for each

concentration. The anodic peak from the oxidation of tramadol appeared around 0.7 V vs Ag|AgCl (3 M KCl). The linear equation is as shown below (**Equation** 4.10):

I_{pa} (μA) = 0.0315±0.0003 [tramadol, μM] + 3.9940±0.040 (R^2 = 0.9938) (4.10)

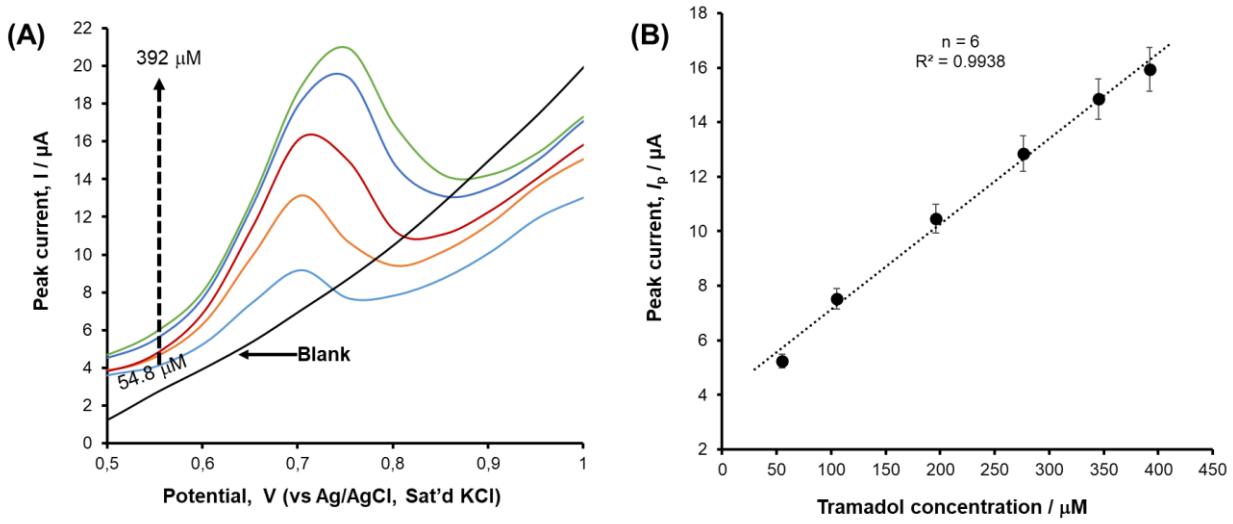


Figure 4.10 (A) Typical square wave voltammograms obtained in PBS (pH 7.4) containing different concentrations of tramadol (0 – 392 μM), and (B) plot of peak current response versus concentration of tramadol.

The electrode shows wide linear range (54.8 – 392 μM), high sensitivity (*m* = 0.0313 A M^{-1}) and low limit of detection and quantification (LoD ~ 3.80 μM, determined from LoD = 3 *s/m*, and LoQ = 10 *s/m* ~ 12.7 μM, where *s* is the standard deviation of the intercept (in μA), while *m* is the slope/sensitivity of the calibration plot (in μA/μM). Table 4.5 summarized values calculated using six electrode average.

4.3.6.2 Determination of tramadol in pharmaceutical sample and human serum

To validate that the OLC can be used for the determination of TR using 'a point-of-

care' type of electrode, a commercial screen-printed carbon electrode (SPCE, Dropsens®) was modified with OLC ink and used to determine TR in two different real sample solutions, i.e., "tramadol hydrochloride" capsule (50 mg tramadol) in (i) PBS (pH 7.40) (**Figure 4.11A,B**) and (ii) artificial human blood / serum diluted in PBS (pH 7.40) (**Figure 4,11C,D**). Human serum solution was first prepared by dissolving it in PBS (pH 7.40) at 1:100 v/v ratio. and tramadol dissolved. In all cases, the OLC-modified SPCE successfully detected TR, with the anodic peak current appearing at around the 0.70 V vs Ag|AgCl (Sat'd KCl) as was also seen for the pure tramadol samples in GCE-OLC electrode. Each of the four capsules was carefully opened, and contents accurately weighed to be *ca.* 82 mg (meaning that weight of excipients is *ca.* 39 % per capsule which, according to the description in the label, comprises colloidal silicon dioxide, magnesium stearate, microcrystalline cellulose, and sodium starch glycolate). A stock solution of each powder (3.75 mg in 10 ml, i.e., ~ 2.29 mg 'pure' tramadol chloride in 10 ml or 0.87 M tramadol chloride) was prepared in PBS (pH 7.40) as well as in human serum solution. Considering the importance of determining TR in the presence of real interfering materials in complex matrices such as human serum and excipient-rich tramadol capsule sample, no further treatment of the solution (such as filtering to obtain 'pure' supernatant) was carried out.

A standard addition method was used to conduct the concentrations studies (in the range of 20 nm to 0.45 uM) as shown in Figure 4.11. As should be expected, both DPV curves show broad peaks (Figure 4.11A&C) compared to the pure tramadol (shown in Figure 4.10A) due to the presence of several interfering species in the capsule and human serum. As should be expected, the resistivity introduced by these interferents and blank electrolyte would lead to the linear calibration curves

not starting from the origin, despite efforts to subtract the background current. However, interestingly, the tramadol peak was still around 0.7 V (vs Ag|AgCl Sat'd KCl) as in pure tramadol analysis.

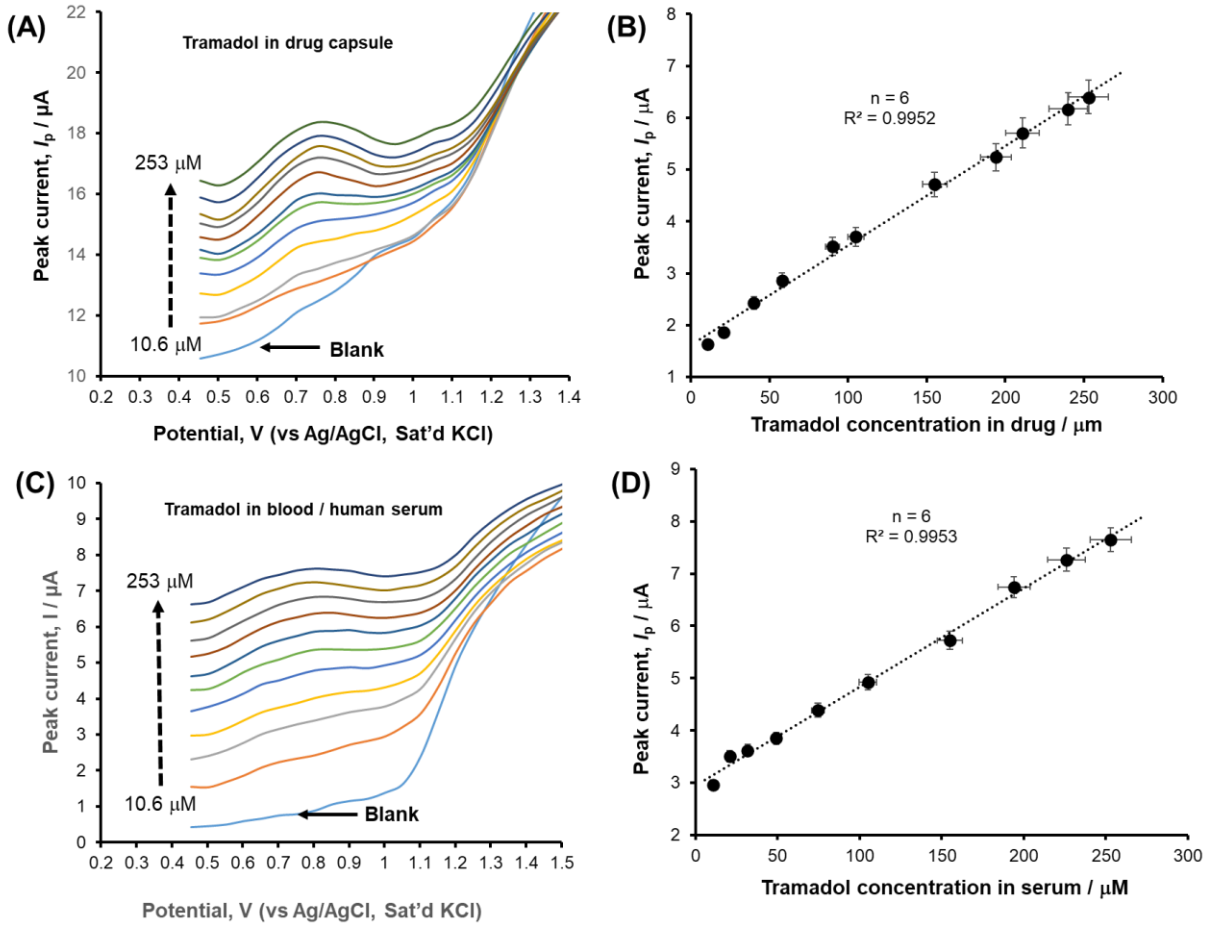


Figure 4.11 Typical SWV curves (A, C) obtained in real sample analysis using screen-printed carbon electrode (SPCE) modified with OLC (SPCE-OLC) for tramadol in drug capsule (A) and in human serum solution (C); and the plot of background-subtracted peak current responses versus the concentrations of tramadol (B,D).

The equations for the resulting calibration plots were as follows, **Equations 4.11 and 4.12**:

Tramadol capsule (pH 7.4):

I_{pa} (μA) = 0.0192±0.0002 [tramadol, μM] + 1.6154±0.015 (R^2 = 0.9955)

(4.11)

Tramadol in human serum (pH 7.4):

I_{pa} (μA) = 0.0188 ±0.0002 [tramadol, μM] + 2.9518±0.0300 (R^2 = 0.9953)

(4.12)

The contents of TR hydrochloride in each capsule were calculated to be 49.78 mg per tablet with a RSD of 3.2 % (n = 5), which is close to the labelled amount of 50 mg. The limit of detection (LoD) and limit of quantification (LoQ) for the drug (2.34 and 7.81 μM, respectively) and for the serum (4.70 and 15.9 μM, respectively). Although the key focus of this investigation is on the fundamental science and electrochemistry, it is interesting however to see that the results obtained in this work are comparable with many literature, for example, with carbon nanoparticles [33] and dual-carbon paste electrode modified with phosphotungstic acid and silicomolybdic acid [32]. Importantly, despite that this work has not been optimized to improve detection limits, it should be noted that these observed detection limits are quite satisfactory, especially if one considers that the toxic effects of TR only occurs when the blood tramadol concentration is greater than 1 mg/L (i.e., 3.8 μM) [4, 64] and, in most cases, when the blood tramadol concentrations are within the range of 1.6 – 61.8 mg/L (i.e., 6.07 – 234.64 μM) [65-68], which are several times greater than the normal therapeutic range of 0.1 - 0.3 mg/L (i.e., 0.38 – 1.14 μM) [64]. Indeed, the results show the potential for the use of OLC as an electrocatalytic platform for sensitive detection of tramadol.

Table 4.9 Summary of results obtained in this work for electrochemical sensing of tramadol, using the DPV method.

Sample	**Technique**	**Electrolyte**	**LCR / μM**	**LoD /μM**	**LoQ /μM**
GCE-OLC	DPV	PBS (pH 7.4)	54.8 - 392	3.80	12.70
SPE-OLC	DPV	PBS (pH 7.4)	27.9 - 345	17.5	58.14
SPE-OLC	DPV	Drug, PBS (pH 7.4)	10.6 – 253	2.34	7.81
SPE-OLC	DPV	Serum,PBS (pH 7.4)	10.6 – 253	4.70	15.90

4.4 Conclusion

This work has clearly shown that OLC is a better electrocatalyst than conventional CB for the detection of tramadol, including in pharmaceutical formulations. DFT simulations suggests that the high performance of the OLC is related to its spherical morphology and weak adsorption of tramadol on its surface.

4.5 References

1) L. Gong, U.M. Stamer, M.V. Tzvetkov, R.B. Altman, T.E. Klein, PharmGKB summary: tramadol pathway, Pharmacogenet Genomics, 2014, 24, 374-380.
2) S. Agrawal, P.R. Patel, R.V.N. Gundloori, Proteins as Nanocarriers To Regulate Parenteral Delivery of Tramadol, ACS omega, 2019, 4, 6301-6310.
3) G. Saccomanni, S. Del Carlo, M. Giorgi, C. Manera, A. Saba, M. Macchia, Determination of tramadol and metabolites by HPLC-FL and HPLC-MS/MS in urine of dogs, J Pharm Biomed Anal, 2010, 53, 194-199.
4) B. Solarino, B. Riesselmann, C.T. Buschmann, M. Tsokos, Multidrug poisoning involving nicotine and tramadol, Forensic Sci Int, 2010, 194, e17-19.
5) M. Subedi, S. Bajaj, M.S. Kumar, M. Yc, An overview of tramadol and its usage in pain management and future perspective, Biomed Pharmacother, 2019, 111, 443-451.
6) U.A. Murashova, L.V. Skalkina, P.V. Kazakov, N.S. Mirzabekova, Development of Chromatographic Methods for Assay of Contaminants of Russian-Made Tramadol Hydrochloride Substance, Pharmaceutical Chemistry Journal, 2020, 54, 766-771.
7) S. Hassamal, K. Miotto, W. Dale, I. Danovitch, Tramadol: understanding the risk of serotonin syndrome and seizures, The American journal of medicine, 2018, 131, 1382.e1-1382.e6
8) U.E. Chikezie, I.D. Ebuenyi, Tramadol misuse in the Niger Delta; A review of cases presenting within a year, Journal of Substance Use, 2019, 24, 487-491.

9) P. Peprah, W. Agyemang-Duah, E. Appiah-Brempong, A.G. Akwasi, A.K. Morgan, "With tramadol, I ride like a Jaguar": a qualitative study of motivations for non-medical purpose tramadol use among commercial vehicle operators in Kumasi, Ghana, Subst Abuse Treat Prev Policy, 2020, 15, 49.

10) J.B. Cole, S. Sattiraju, E.F. Bilden, R.W. Asinger, S.C. Bertog, Isolated tramadol overdose associated with Brugada ECG pattern, Pacing and Clinical Electrophysiology, 2012, 35, e219-e221.

11) N. Belin, A.-L. Clairet, S. Chocron, G. Capellier, G. Piton, Refractory cardiogenic shock during tramadol poisoning: a case report, Cardiovascular toxicology, 2017, 17, 219-222.

12) S.G. Zimmermann, A. Schmukat, M. Schulz, J. Benner, U. Gunten, T.A. Ternes, Kinetic and mechanistic investigations of the oxidation of tramadol by ferrate and ozone, Environ Sci Technol, 2012, 46, 876-884.

13) S. Amin, A. Hameed, N. Memon, A.R. Solangi, M. Aslam, Sirajuddin, M.T. Soomro, The efficacy of the Nafion® blended CTAB protected Au nanoparticles for the electrochemical detection of tramadol in wastewater: A parametric investigation, Journal of Environmental Chemical Engineering, 2016, 4, 3825-3834.

14) P. Du, Z. Zhou, Z. Wang, Z. Xu, Q. Zheng, X. Li, J. He, X. Li, H. Cheng, P.K. Thai, Analysing wastewater to estimate fentanyl and tramadol use in major Chinese cities, Sci Total Environ, 2021, 795, 148838.

15) A. Curticapean, D. Muntean, M. Curticapean, M. Dogaru, C. Vari, Optimized HPLC method for tramadol and O-desmethyl tramadol determination in human plasma, Journal of biochemical and biophysical methods, 2008, 70, 1304-1312.

16) L. Vlase, S.E. Leucuta, S. Imre, Determination of tramadol and O-desmethyltramadol in human plasma by high-performance liquid chromatography with mass spectrometry detection, Talanta, 2008, 75, 1104-1109.

17) S.N. Ding, J.J. Xu, W.J. Zhang, H.Y. Chen, Tris(2,2'-bipyridyl)ruthenium(II)-Zirconia-Nafion composite modified electrode applied as solid-state electrochemiluminescence detector on electrophoretic microchip for detection of pharmaceuticals of tramadol, lidocaine and ofloxacin, Talanta, 2006, 70, 572-577.

18) T. Madrakian, A. Afkhami, H. Mahmood-Kashani, M. Ahmadi, Superparamagnetic surface molecularly imprinted nanoparticles for sensitive solid-phase extraction of tramadol from urine samples, Talanta, 2013, 105 255-261.

19) H.M. Abu-Shawish, N.A. Ghalwa, F.R. Zaggout, S.M. Saadeh, A.R. Al-Dalou, A.A.A. Assi, Improved determination of tramadol hydrochloride in biological fluids and pharmaceutical preparations utilizing a modified carbon paste electrode, Biochemical Engineering Journal, 2010, 48, 237-245.

20) A. Afkhami, H. Khoshsafar, H. Bagheri, T. Madrakian, Preparation of NiFe(2)O(4)/graphene nanocomposite and its application as a modifier for the fabrication of an electrochemical sensor for the simultaneous determination of tramadol and acetaminophen, Anal Chim Acta, 2014, 831, 50-59.

21) M.R. Aflatoonian, S. Tajik, B. Aflatoonian, H. Beitollahi, K. Zhang, Q.V. Le, J.H. Cha, H.W. Jang, M. Shokouhimehr, W. Peng, A Screen-Printed Electrode Modified With Graphene/Co3O4 Nanocomposite for Electrochemical Detection of Tramadol, Front Chem, 2020, 8, 562308.

22) V. Arabali, S. Malekmohammadi, F. Karimi, Surface amplification of pencil graphite electrode using CuO nanoparticle/polypyrrole nanocomposite; a powerful electrochemical strategy for determination of tramadol, Microchemical Journal, 2020, 158.

23) N.F. Atta, R.A. Ahmed, H.M.A. Amin, A. Galal, Monodispersed Gold Nanoparticles Decorated Carbon Nanotubes as an Enhanced Sensing Platform for Nanomolar Detection of Tramadol, Electroanalysis, 2012, 24, 2135-2146.

24) A. Babaei, A.R. Taheri, M. Afrasiabi, A multi-walled carbon nanotube-modified glassy carbon electrode as a new sensor for the sensitive simultaneous determination of paracetamol and tramadol in pharmaceutical preparations and biological fluids, Journal of the Brazilian Chemical Society, 2011, 22, 1549-1558.

25) Z. Jahromi, E. Mirzaei, A. Savardashtaki, M. Afzali, Z. Afzali, A rapid and selective electrochemical sensor based on electrospun carbon nanofibers for tramadol detection, Microchemical Journal, 2020, 157, 104942.

26) M. Khairy, C.E. Banks, A screen-printed electrochemical sensing platform surface modified with nanostructured ytterbium oxide nanoplates facilitating the electroanalytical sensing of the analgesic drugs acetaminophen and tramadol, Mikrochim Acta, 2020, 187, 126.

27) T. Madrakian, S. Alizadeh, M. Bahram, A. Afkhami, A novel electrochemical sensor based on magneto LDH/Fe3O4 nanoparticles @ glassy carbon electrode for voltammetric determination of tramadol in real samples, Ionics, 2016, 23, 1005-1015.

28) M.A. Mohamed, S.A. Atty, N.N. Salama, C.E. Banks, Highly Selective Sensing

Platform Utilizing Graphene Oxide and Multiwalled Carbon Nanotubes for the Sensitive Determination of Tramadol in the Presence of Co-Formulated Drugs, Electroanalysis, 2017, 29, 1038-1048.

29) S. Mohammadi, M.A. Taher, H. Beitollahi, A hierarchical 3D camellia-like molybdenum tungsten disulfide architectures for the determination of morphine and tramadol, Mikrochim Acta, 2020, 187, 312.

30) E. Mynttinen, N. Wester, T. Lilius, E. Kalso, J. Koskinen, T. Laurila, Simultaneous electrochemical detection of tramadol and O-desmethyltramadol with Nafion-coated tetrahedral amorphous carbon electrode, Electrochimica Acta, 2019, 295, 347-353.

31) A.F. Nada, G.G. Abdo, A. Elzatahry, A. Galal, S.H. Hassan, Designed electrochemical sensor based on metallocene modified conducting polymer composite for effective determination of tramadol in real samples, Canadian Journal of Chemistry, 2021, 99, 437–446.

32) H.M. Abu-Shawish, N.A. Ghalwa, F.R. Zaggout, S.M. Saadeh, A.R. Al-Dalou, A.A. Abou Assi, Improved determination of tramadol hydrochloride in biological fluids and pharmaceutical preparations utilizing a modified carbon paste electrode, Biochemical Engineering Journal, 2010, 48, 237-245.

33) F. Ghorbani-Bidkorbeh, S. Shahrokhian, A. Mohammadi, R. Dinarvand, Simultaneous voltammetric determination of tramadol and acetaminophen using carbon nanoparticles modified glassy carbon electrode, Electrochimica Acta, 2010, 55, 2752-2759.

34) N. Keller, N.I. Maksimova, V.V. Roddatis, M. Schur, G. Mestl, Y.V. Butenko, V.L. Kuznetsov, R. Schlögl, The catalytic use of onion-like carbon materials for styrene synthesis by oxidative dehydrogenation of ethylbenzene,

Angewandte Chemie International Edition, 2002, 41, 1885-1888.

35) N. Palaniyandy, M.A. Kebede, K.I. Ozoemena, M.K. Mathe, Rapidly microwave-synthesized SnO2 nanorods anchored on onion-Like carbons (OLCs) as anode material for lithium-ion batteries, Electrocatalysis, 2019, 10, 314-322.

36) N. Palaniyandy, M.A. Kebede, K. Raju, K.I. Ozoemena, L. Le Roux, M.K. Mathe, R. Jayaprakasam, α-MnO2 nanorod/onion-like carbon composite cathode material for aqueous zinc-ion battery, Materials Chemistry and Physics, 2019, 230, 258-266.

37) K. Makgopa, P.M. Ejikeme, C.J. Jafta, K. Raju, M. Zeiger, V. Presser, K.I. Ozoemena, A high-rate aqueous symmetric pseudocapacitor based on highly graphitized onion-like carbon/birnessite-type manganese oxide nanohybrids, Journal of Materials Chemistry A, 2015, 3, 3480-3490.

38) K. Makgopa, K. Raju, P.M. Ejikeme, K.I. Ozoemena, High-performance Mn3O4/onion-like carbon (OLC) nanohybrid pseudocapacitor: Unravelling the intrinsic properties of OLC against other carbon supports, Carbon, 2017, 117, 20-32.

39) S. Choudhury, P. Srimuk, K. Raju, A. Tolosa, S. Fleischmann, M. Zeiger, K.I. Ozoemena, L. Borchardt, V. Presser, Carbon onion/sulfur hybrid cathodes via inverse vulcanization for lithium–sulfur batteries, Sustainable Energy & Fuels, 2018, 2, 133-146.

40) O.C. Ozoemena, T.J. Ehirim, T. Khawula, K. Makgopa, L.J. Shai, K.I. Ozoemena, Bovine Serum Albumin-Dependent Charge-Transfer Kinetics Controls the Electrochemical Immunosensitive Detection: Vibrio cholerae as a Model Bioanalyte, Electrocatalysis, 2021, 12, 595-604.

41) O.C. Ozoemena, L.J. Shai, T. Maphumulo, K.I. Ozoemena, Electrochemical sensing of dopamine using onion-like carbons and their carbon nanofiber composites, Electrocatalysis, 2019, 10, 381-391.

42) P.M. Ejikeme, K. Makgopa, K. Raju, K.I. Ozoemena, Promotional Effects of Nanodiamond-Derived Onion-Like Carbons on the Electrocatalytic Properties of Pd-MnO2 for the Oxidation of Glycerol in Alkaline Medium, ChemElectroChem, 2016, 3, 2243-2251.

43) J.J. Ogada, A.K. Ipadeola, P.V. Mwonga, A.B. Haruna, F. Nichols, S. Chen, H.A. Miller, M.V. Pagliaro, F. Vizza, J.R. Varcoe, CeO2 Modulates the Electronic States of a Palladium Onion-Like Carbon Interface into a Highly Active and Durable Electrocatalyst for Hydrogen Oxidation in Anion-Exchange-Membrane Fuel Cells, ACS Catalysis, 2022, 12, 7014-7029.

44) T.P. Mofokeng, Z.N. Tetana, K.I. Ozoemena, Defective 3D nitrogen-doped carbon nanotube-carbon fibre networks for high-performance supercapacitor: Transformative role of nitrogen-doping from surface-confined to diffusive kinetics, Carbon, 2020, 169, 312-326.

45) L. Reinert, M. Zeiger, S. Suárez, V. Presser, F. Mücklich, Dispersion analysis of carbon nanotubes, carbon onions, and nanodiamonds for their application as reinforcement phase in nickel metal matrix composites, RSC Advances, 2015, 5, 95149-95159.

46) G. Washer, F. Blum, Raman Spectroscopy for the Nondestructive Testing of Carbon Fiber, Research Letters in Materials Science, 2008, 2008, 1-3.

47) D. Yao, Y. Zhang, P.T. Williams, H. Yang, H. Chen, Co-production of hydrogen and carbon nanotubes from real-world waste plastics: Influence of catalyst composition and operational parameters, Applied Catalysis B:

Environmental, 2018, 221, 584-597.

48) I. Streeter, G.G. Wildgoose, L. Shao, R.G. Compton, Cyclic voltammetry on electrode surfaces covered with porous layers: An analysis of electron transfer kinetics at single-walled carbon nanotube modified electrodes, Sensors and Actuators B: Chemical, 2008, 133, 462-466.

49) L. Gaolatlhe, R. Barik, S.C. Ray, K.I. Ozoemena, Voltammetric responses of porous Co3O4 spinels supported on MOF-derived carbons: Effects of porous volume on dopamine diffusion processes, Journal of Electroanalytical Chemistry, 2020, 872.

50) K.I. Ozoemena, N.S. Mathebula, J. Pillay, G. Toschi, J.A. Verschoor, Electron transfer dynamics across self-assembled N-(2-mercaptoethyl) octadecanamide/mycolic acid layers: impedimetric insights into the structural integrity and interaction with anti-mycolic acid antibodies, Phys Chem Chem Phys, 2010, 12, 345-357.

51) J. Pillay, K.I. Ozoemena, Layer-by-layer self-assembled nanostructured phthalocyaninatoiron(II)/SWCNT-poly(m-aminobenzenesulfonic acid) hybrid system on gold surface: Electron transfer dynamics and amplification of H2O2 response, Electrochimica Acta, 2009, 54, 5053-5059.

52) N.W. Maxakato, C.J. Arendse, K.I. Ozoemena, Insights into the electro-oxidation of ethylene glycol at Pt/Ru nanocatalysts supported on MWCNTs: Adsorption-controlled electrode kinetics, Electrochemistry Communications, 2009, 11, 534-537.

53) T.P. Mofokeng, A.K. Ipadeola, Z.N. Tetana, K.I. Ozoemena, Defect-Engineered Nanostructured Ni/MOF-Derived Carbons for an Efficient Aqueous Battery-Type Energy Storage Device, ACS Omega, 2020, 5, 20461-

20472.

54) M.E. Orazem, B. Tribollet, Electrochemical impedance spectroscopy, 2nd ed. 2017. Print ISBN:9780470041406, Online ISBN:9780470381588, DOI:10.1002/9780470381588

55) P.M. Monk, Fundamentals of electroanalytical chemistry, John Wiley & Sons2008.

56) A.J. Bard, L.R. Faulkner, Electrochemical Methods: Fundamentals and Applications, 2nd ed., Wiley2001.

57) R.G. Compton, C.E. Banks, Understanding voltammetry, World Scientific2018.

58) H. Ahmar, A.R. Fakhari, Electro-oxidation and adsorptive stripping voltammetric determination of ephedrine and pseudoephedrine at carboxylated multi-walled carbon nanotube-modified electrode, Analytical Methods, 2012, 4.

59) J.T. Zhang, Yu-Hong; Pietro, William J,; Lever, A.B.P., Electrocatalytic activity of N,N',N'',N''-tetramethyl-tetra-3,4-pyridoporphyrazinocobalt(II) adsorbed on a graphite electrode towards the oxidation of hydrazine and hydroxylamine Journal of Electroanalytical Chemistry, 1996, 406, 203-211.

60) J.H.P. Zagal, Maritza A., Electro-oxidation of hydrazine on electrodes modified with vitamin B12, Electrochimica Acta, 1997, 42, 3477-3481.

61) M.P. Siswana, K.I. Ozoemena, T. Nyokong, Electrocatalysis of asulam on cobalt phthalocyanine modified multi-walled carbon nanotubes immobilized on a basal plane pyrolytic graphite electrode, Electrochimica Acta, 2006, 52, 114-122.

62) T. Yang, S. Yang, W. Jin, Y. Zhang, N. Barsan, A. Hemeryck, S. Wageh, A.A.

Al-Ghamdi, Y. Liu, J. Zhou, W. Chen, H. Zhang, Density Functional Investigation on alpha-MoO3 (100): Amines Adsorption and Surface Chemistry, ACS Sens, 2022, 7, 1213-1221.

63) P. Wang, X. Yuan, Z. Cui, C. Xu, Z. Sun, J. Li, J. Liu, Y. Tian, H. Li, A Nanometer-Sized Graphite/Boron-Doped Diamond Electrochemical Sensor for Sensitive Detection of Acetaminophen, ACS Omega, 2021, 6, 6326-6334.

64) S. Nakhaee, C. Hoyte, R.C. Dart, M. Askari, R.J. Lamarine, O. Mehrpour, A review on tramadol toxicity: mechanism of action, clinical presentation, and treatment, Forensic Toxicology, 2021, 39, 293-310.

65) K. De Decker, J. Cordonnier, W. Jacobs, V. Coucke, P. Schepens, P.G. Jorens, Fatal intoxication due to tramadol alone: case report and review of the literature, Forensic science international, 2008, 175, 79-82.

66) J.E. Clarkson, J.M. Lacy, C.L. Fligner, N. Thiersch, J. Howard, R.C. Harruff, B.K. Logan, Tramadol (Ultram®) concentrations in death investigation and impaired driving cases and their significance, Journal of Forensic Science, 2004, 49, JFS2004019-2004015.

67) B. De Backer, F. Renardy, R. Denooz, C. Charlier, Quantification in postmortem blood and identification in urine of tramadol and its two main metabolites in two cases of lethal tramadol intoxication, Journal of analytical toxicology, 2010, 34, 599-604.

68) N. Barbera, M. Fisichella, A. Bosco, F. Indorato, G. Spadaro, G. Romano, A suicidal poisoning due to tramadol. A metabolic approach to death investigation, Journal of forensic and legal medicine, 2013, 20, 555-558.

CHAPTER 5

Studies on the Electrocatalytic Oxidation and Detection of Ethanol on Palladium-Ceria-Onion-Like Carbon Electrocatalyst

Synopsis

The electrocatalytic oxidation of alcohol (EOR) in alkaline media is vital for the development of alkaline direct alcohol fuel cells (ADAFCs) as well as electrochemical sensors for alcohol in alkaline media. This Chapter describes the investigation of EOR in alkaline electrolyte (KOH), comparing the palladium catalysts supported on conductive carbon (Pd/CB), onion-like carbon (Pd/OLC), and ceria-OLC (Pd-CeO_2/OLC). Here, it is clearly proven that Pd-CeO_2/OLC exhibits the best electrocatalytic performance of EOR and sensing of ethanol, fully supported by DFT calculations, HRTEM and XPS data, due to the modulation of the electronic properties of the Pd-OLC interface.

5.1 Introduction

Ethanol oxidation reaction (EOR) is an industrially important process for the development of ethanol sensors and ethanol fuel cells for electricity generation (unique technology for the generation of clean and sustainable electricity from ethanol and air) [1]. Ethanol sensors are important for a plethora of applications, including in pharmaceutical industry, beverage industry, and mitigating the challenges of alcohol abuse and drunk driving in the society. Conventionally, ethanol is determined using a hydrometer, which is fraught with inaccuracy and human errors during reading. Other methods include the use of spectroscopy [2], and chromatography [3] which are bulky, expensive, and complex and difficult to miniaturize. Electrochemical techniques, on the other hand, are getting more attention [4-12] due to their simplicity, accuracy, low-cost, and ease of miniaturizing the sensor for use by non-skilled worker.

Efficient EOR can find applications in the development of alkaline direct ethanol fuel cell (ADEFC) which represents one of the most preferrable electrochemical energy devices for the development of renewable and clean electricity. ADEFC has become important because of the impressive properties of ethanol including high theoretical energy density, affordability, easy transportation and storage and non-toxicity [1, 13, 14]. Moreover, large quantities of ethanol can be produced from agricultural and

organic municipal wastes; 90 million liters of ethanol are produced globally from agricultural and organic domestic wastes every year [14].

Palladium(Pd)-based electrocatalysts are the most important electrocatalysts for EOR due to the high compatibility of Pd with non-noble metals, and excellent activity in alkaline media, where the non-noble metals can also be stable and function sufficiently for electrochemical applications [15]. One of the Pd-based electrocatalysts that have captured the interests of researchers for EOR is the carbon-supported Pd-CeO_2 electrocatalyst [16-19]. Like other auxiliary metal oxides (such as SnO_2, Mn_3O_4, Co_3O_4 and NiO), CeO2 is thought to increase the concentration of the surface-adsorbed hydroxyl species (OH_{ads}) on the Pd catalyst, thereby facilitating the C-C bond cleavage and formation of the final oxidation products [20]. However, unlike other auxiliary metal oxides, the CeO2 has been found to endow unique properties towards Pd catalyst: aside from having superior storage capacity for oxygen, it exhibits the Ce^{4+}/Ce^{3+} redox couple during the redox processes that lead to complex Pd−CeO_2 interactions that yield different Pd species.

A noble metal such as Pt or Pd interacts with CeO2, forming a highly dispersed noble metal ionic catalyst (NMIC) represented as $Ce_{1-x}M_xO_{2-\delta}$ (where M = noble metal, creating oxygen vacancies) rather than existing as metal nanoparticles on CeO2 support. The $Ce_{1-x}M_xO_{2-\delta}$ is found to be a better electrocatalyst than the same amount of M due to electronic interaction between M metal ions and CeO2 lattice [17]. The existence of the noble metal in CeO_2 lattice creates the adsorption sites for the electrocatalytic activities. In other words, for example, the Pd ions act as the adsorption sites for the electron donating molecule, thereby increasing the rates of oxidation reaction. The synergistic interaction between the noble metal and Ce ions allows for increased electron exchange, resulting in enhanced electrocatalytic

activity. However, both Ce and Pd take part in the electrocatalytic process by the synergistic electron transport between them. For example, XPS data had provided some evidence of how Pd^{2+}/Pd^{0} and Ce^{4+}/Ce^{3+} redox couples interact to keep Pd in its ionic state and, at the same time, permitting the availability of the lattice oxygen for the oxidation reaction [21, 22].

In a recent work [16], we showed that Pd-CeO_2/OLC is an efficient electrocatalyst for the development of durable anion-exchange membrane fuel cells (AEMFC) compared to the Pd alone (i.e., Pd-supported on carbon black (Pd/CB), or onion-like carbon (Pd/OLC)) and Pd-CeO_2/CB. The superior performance of the OLC and the ability of the CeO2 to modulate the electronic properties of the Pd/OLC has prompted the present study of the Pd-CeO_2/OLC for EOR in alkaline environment. We show that Pd-CeO_2/OLC is a viable new electrocatalyst for EOR and ethanol sensing. The underlying reasons for the enhanced electrocatalysis has been explained from the DFT calculations that show weak adsorption of the intermediates CH_3CO* and OH*, and the excellent conductivity (low band gap) arising from the highly effective charge of the defect-rich Ce_{1-x} $Pd_xO_{2-\delta}$ and OLC. Further insights were obtained from the valence band of the XPS data that show an increased lattice strain and the downshift of the d-band centre of the Pd-CeO_2/OLC compared to the monometallic catalysts (Pd/CB and Pd/OLC).

5.2 Experimental

5.2.1 Materials and reagents

Acetylene carbon black (TIMICAL SUPER C45, 45 m^2 g^{-1}) was obtained from Gelon, China, while OLC was synthesized from high purity (98–99%) nanodiamond

powder (NaBond Technologies) by annealing in a muffle furnace at 1300 ^{o}C for 3 h in an argon atmosphere.[23] $PdCl_2$ (≥99.9 %) and ethylene glycol (99.8 %), $Ce(NO_3)_3.6H_2O$ (99.999 %) and all other reagents were of analytical grade and purchased from Sigma-Aldrich without further purification. Platinum on graphitized carbon (40 wt%) was purchased from Sigma-Aldrich.

5.2.2 Synthesis procedures

To allow for comparison, the synthesis methods used are similar to a previous report [24], except those of the catalysts with OLC and OLC-CeO_2.

5.2.2.1 Synthesis of Pd/carbon

A mixture of 0.25 g conductive carbon black (CB, Timcal Super C45) and ethylene glycol (EG, 50 mL) was contained in a three-neck round-bottomed flask (500 mL) and sonicated for 20 min. $PdCl_2$ (0.04165 mg) was dispersed in a mixture of H_2O (2.083 mL), EG (50 mL) and 0.25 mL HCl (37%). The solution was then added in a dropwise fashion under stirring in a stream of N_2. After proper stirring, NaOH (5 g) was dissolved in H_2O (10 mL) and EG (35 mL) to make an alkaline solution, which was added to the reactor. The resultant mixture was then heated under a N_2 atmosphere for 3h at 125 °C, and then left to cool to room temperature. The mixture was then filtered leaving behind the desired product, which was then rinsed with distilled H_2O until a neutral pH and then dried in a vacuum oven at 40 °C.

5.2.2.2 Synthesis of OLC-CeO_2 support

A mixture of the OLC (2.0 g) and a solution of $Ce(NO_3)_3.6H_2O$ (5.05 g) in H_2O (125 mL) was stirred for 60 min and sonicated for 30 min. The pH was then adjusted to 12 with KOH and stirred for 2 h. The mixture was then filtered leaving behind the desired

product, which was then rinsed with distilled H_2O until a neutral pH and then dried in a vacuum oven at 65 °C, and thereafter heated under air in a tube furnace for 2 h at 250 °C. The product was cooled to room temperature under a flow of Ar.

5.2.2.3 Synthesis of Pd-CeO_2/OLC

A suspension of OLC-CeO_2 (500 mg) in water (62.5 mL) was vigorously stirred for 30 minutes and sonicated for 20 minutes. A solution of K_2PdCl_4 (172.5 mg) in water (7.5 mL) was then slowly added (approx. 1 hour) whilst stirring. This was followed by the addition of an aqueous solution of 2.5 M KOH (1.05 mL), after which ethanol (50 mL) was added. The resulting mixture was heated for 60 min at 80 °C, after which it was filtered, leaving behind the desired product (Pd-CeO_2/OLC), which was then washed with distilled water until a neutral pH and dried under vacuum at 65°C.

5.2.3 Physical property characterization

The catalysts were characterized using powder X-ray diffraction (PXRD) (Bruker D2 Phaser X-ray diffractometer equipped with a monochromatic Cu-Kα X-rays at λ=1.5406 Å) to investigate the crystallite size and structural phases. Elemental analysis of the samples was conducted using the energy-dispersive X-ray spectroscopy (EDS) unit “FEI Nova Nanolab 600 SEM” connected to a scanning electron microscope. This technique also establishes the chemical composition and elemental distribution profiles at the electrocatalyst surfaces. High-resolution transmission electron micrograms (HRTEM) were acquired from HRTEM (JEOL 2010F). Scanning electron microscopy (SEM) and transmission electron microscopy (TEM) were used to obtain information on the structural properties of the samples and correlate it with Brunauer-Emmett-Teller (BET) results, while X-ray photoelectron spectroscopy (XPS) was employed to understand the chemical state

and binding energies to within the surface resolution of the samples. The specific surface areas of the samples were obtained with the single-point Brunauer-Emmett-Teller (BET) method using the Micromeritics TriStar II 3000 area and porosity analyzer instrument. Raman spectroscopy (Bruker Senterra laser Raman spectrometer) was used to verify bond vibration in Pd/CB, Pd/OLC and Pd-CeO_2/OLC. The thermal stability of each Pd-based sample was studied with the help of a Perkin Elmer Thermogravimetric analyzer (TGA)/Differential Thermogravimetric analysis (DTGA) 6000. In a standard run, 10 mg of the samples were placed into a high-temperature alumina sample cup that was supported on an analytical balance located in the furnace chamber of the analyzer and the sample was heated in the air (5 °C min^{-1}) from 35 °C to 900 °C. Initially, the instrument uses nitrogen gas for purging (20 mL min^{-1}) while holding at 35°C for 5 min.

5.2.4 Density functional theory (DFT) calculations

DFT simulations were performed with the supercomputational facilities at the Centre for High Performance Computing (CHPC, Cape Town, South Africa) using the BIOVIA Material Studio and employing adsorption locator tool module. Two adsorbates (CH_3CO* and *OH) were chosen and adsorbed onto the modelled electrocatalyst surfaces (Pd/C, Pd/OLC, and Pd/CeO_2/OLC). Supercells of 3x3 were modelled for all the above electrocatalysts', followed by geometric relaxation calculations with a threshold energy set at 10^{-6} eV for convergence to be achieved. Material studio cleaning tool was used. The minimum adsorption distance was set at 5 Å. DMoI3, another module of the BIOVIA Materials Studio, was used to calculate the electronic properties. The same threshold energy as that used for adsorption was set for the calculations of electronic and energy properties. Condensed-phase

Optimization Molecular Potential for Atomistic Simulation Studies (COMPASS), forcefield was used since it guarantees reliable theoretical results.

5.2.5 Electrochemical and physical characterization

Electrochemical measurements were used to examine the electrochemical performance of the synthesized electrocatalysts. The experiments were performed using the SP300 Bio-Logic Potentiostat (running on EC-Lab software). A three-electrode configuration was used for half-cell tests, comprising a glassy carbon electrode (GCE, dia. 5.0 mm, 0.196 cm2) modified with the electrocatalysts ink as the working electrode, a platinum wire as the counter electrode, and a Ag|AgCl electrode (3 M KCl) as the reference electrode. The EOR was performed using a three-electrode (half-cell) system comprising of a GCE (diameter = 3 mm) as the WE, platinum wire as the CE (to generate applied potentials at the working electrode), and Ag|AgCl electrode (3 M KCl) as the RE (to monitor the current generated at the working electrode). The GCE was cleaned by proper polishing on a pad using alumina (Al2O3; nanopowder Aldrich) slurry followed by ultrasonic stirring in ethanol and acetone. The catalyst ink was prepared by dispersing the powder (1 mg) in ethanol (1 mL) and adding 100 µL of Nafion (5 wt%) to increase the adhesion of the catalyst material on the GCE. The mixture was sonicated for 30 min to obtain a homogeneous mixture. The catalyst ink (12 µL) was then deposited on the GCE in a dropwise fashion and allowed to dry, producing an electrocatalyst loading of 0.0144 mg cm^{-2}. Electrochemical impedance spectroscopy (EIS) was performed using the Bio-Logic Potentiostat. Between 100 kHz and 0.01 Hz at an amplitude of 10 mV, in the electrolyte solution containing redox probe (3 mM K4Fe(CN)6/K3Fe(CN)6 (1:1 mol ratio) dissolved in 0.1 M KCl). The EIS was

conducted at an equilibrium potential (E1/2) of the redox probe (0.15 V vs Ag|AgCl, 3 M KCl) observed from cyclic voltammetry experiments. Alcoholic drinks used for sensor testing were purchased from local suppliers.

5.3 Results and Discussion

5.3.1 Materials characterization

Figure 5.1 shows the thermal gravimetric analysis (TGA) comparison of the Pd/CB, Pd/OLC and Pd-CeO2/OLC. It is noted that the onset decomposition temperatures of CB and OLC were at 689 and 670 °C, respectively. Both Pd/CB and Pd/OLC showed weight retention of ca. 10%, confirming the presence of the 10% Pd used in the synthesis. The Pd-CeO2/OLC showed weight retention of about 38%, due to the presence of the Pd and Ce, and possibly their oxides.

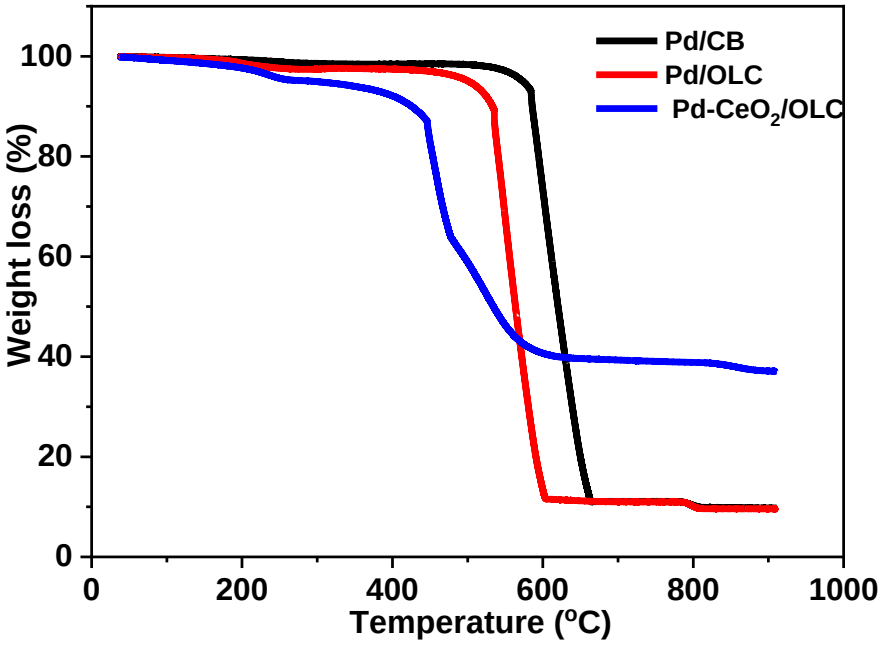


Figure 5.1 TGA of CB and OLC and their derivative TGA

The Raman spectra of the Pd/CB (Figure 5.2A), PD/OLC (Figure 5.2B) and Pd-CeO2/OLC (Figure 5.2C) show the two characteristic peaks of carbons around

1000 cm^{-1} (D band, describing the degree of defect or disorder in carbon, i.e., sp3-bonded carbon atoms) and ~ 2000 cm^{-1} (G band, describing the degree of graphitization in carbon, i.e., sp2-bonded carbon atoms) [25-27]. The intensity ratio of the bands (ID/IG) decreases as follows: Pd/CB (1.01) < Pd/OLC (1.26) and Pd-CeO2/OLC (1.35), which means that the presence of the CeO2 in the Pd-CeO2/OLC resulted in creating the most defects in the OLC (~ 7% defects compared to the Pd/OLC alone). It is well known that defect-rich surfaces can modulate electron distribution than their defect-poor (perfect) counterparts, and thus can greatly enhance electrocatalysis[28-30]

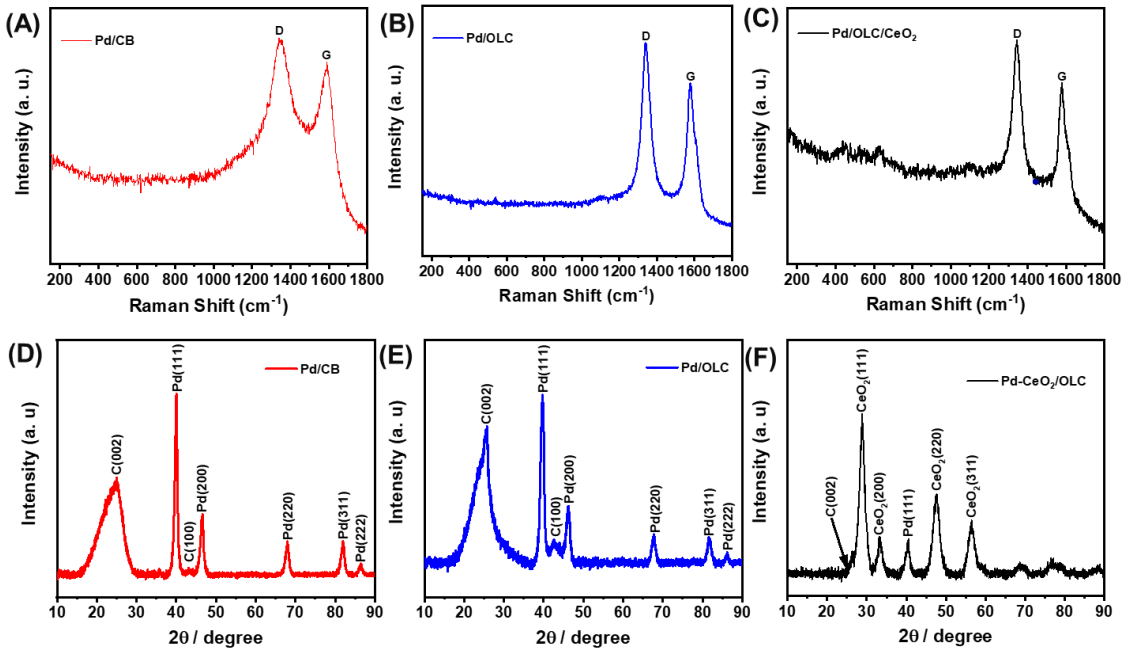


Figure 5.2 Raman spectra (A-C) and XRD patterns (D-F) of the electrocatalysts

The Raman spectra of the Pd-CeO_2/OLC (Figure 5.2C) show weak bands in the 600 – 400 cm-1 region. The band *ca.* 636 cm^{-1} is related to the doubly degenerate LO mode of CeO_2 [31],[32] and is evident of oxygen vacancies (Ov) in the CeO_2 lattice [33]. The weak bands suggest the presence high number of Ov (i.e., Pd-OLC_x-Ce_{1-}

$_xO_{2-y}$). Indeed, the weak or broad band in the 636 and 450 cm^{-1} regions are clear indication of defects or disordering as well as increased Pd-O-Ce bond strength [34]. The absence of bands below 400 cm^{-1} is due to a decrease in the crystallite size [34]. In general, one can conclude that the Pd/CeO_2-OLC is made up of small nanocrystal sizes.

Figure 5.2D-F compares the powder XRD patterns of the Pd/C (Figure 5.2D), Pd/OLC (Figure 5.2E) and Pd-CeO_2/OLC (Figure 5.2F), with the hexagonal carbon structure (002) appearing at 2θ ≈ 24.3° (for Pd/CB), 25.9° (for Pd/OLC), and weakly at 26.1° for the Pd-CeO_2/OLC. The suppression of the carbon peak (002) in the Pd-CeO_2/OLC is due to the high intensity of the adjacent CeO2 peak. The palladium peaks observed at 2θ ≈ 40°, 47°, 68°, 82° and 86° are related to the FCC (face-centred cubic) structure of the crystalline planes of Pd(111), Pd(200), Pd(220), Pd(311) and Pd(222), respectively, which agree with literature [35],[15]. The diffraction peaks of Pd-CeO_2/OLC are broader than those of the Pd/CB and Pd/OLC, which suggests that the presence of CeO2 led to further nano-sizing of the Pd nanoparticles. It is seen that the Pd peak (111) of the Pd-CeO_2/OLC shifted slightly to the higher angles (from 2θ ≈ 40 to 40.6^o) because of the smaller Pd^{2+} (0.86 Å) has been substituted by the larger Ce^{4+}(0.97 Å), contracting the unit cell and forming the Pd-O-Ce bond [36],[37].

Figure 5.3 compares TEM images obtained at low-resolution (500 nm) and high (10 nm) resolutions. the low-resolution TEM images of the four catalysts (500 nm), which show that the Pd/OLC and Pd-CeO_2/OLC have smaller particle sizes and thus high specific surface areas (SSA) compared to the Pd/CB. This result was corroborated with the particle size distribution data (Figure 2G – I) where the average particle increases as: Pd-CeO_2/OLC (6.2 nm) < Pd/OLC (7.5 nm) << Pd/C (52 nm). To

further corroborate the results, single-point BET data (**Table 5.1**) show that the SSA decreases as Pd-CeO_2/OLC (373.53 m^2 g^{-1}) > Pd/OLC (357.73 m^2 g^{-1}) > Pd/CB (30.57 m^2 g^{-1}). Also, the pore sizes increase as follows: Pd/CB (138.65 nm) > Pd/OLC (2.53 nm) > Pd-CeO2/OLC (2.47 nm).

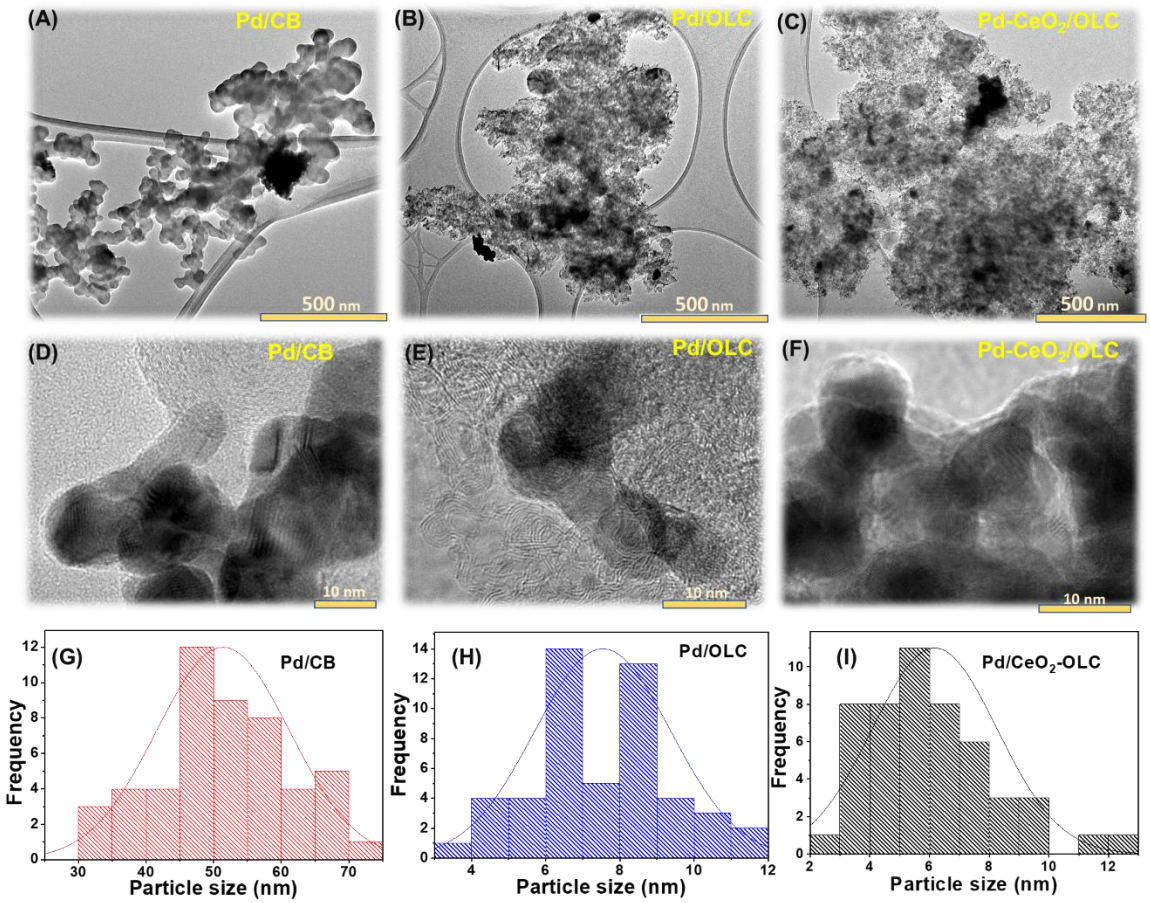


Figure 5.3 Typical low-resolution HRTEM images of (A) Pd/C, (B) Pd/OLC and (C) Pd-CeO_2/OLC, and typical HRTEM images of (D) Pd/CB; (E) Pd/OLC and (F) Pd-CeO_2/OLC. The particle size distribution of (G) PdCB, (H) Pd/OLC and (I) Pd-CeO_2/OLC.

Table 5.1 BET surface areas and porosity of the electrocatalysts.

Sample	Specific surface area, S_{BET} (m^2/g)	Pore volume, V (cm^3/g)	Pore size, D (nm)
Pd/CB	35.6986	0.1408	15.7771
Pd/OLC	357.73	0.225	2.53
Pd-CeO_2/OLC	373.53	0.230	2.47

Figure 5.4 shows the XPS data for the of the three electrocatalysts Pd/OLC and Pd-CeO2/OLC. The wide surveys (Figure 5.4A-C) show the expected elements (Pd, Ce, O and C). The C 1s spectra of the Pd/CB (Figure 4D), Pd/OLC (Figure 5.4E) show C-C (sp2), C-O, C=O, O-C=O and C-C (sp3) bonds at 284.1, 285.79, 287.9, 288.80 and 285 eV, respectively, whereas those of the Pd-CeO2/OLC (Figure 5.4DF) show C-C (sp2), C-O, C=O, O-C=O and C-C (sp3) bonds at 284.19, 285.79, 288.04, 288.80 and 285 eV, respectively.

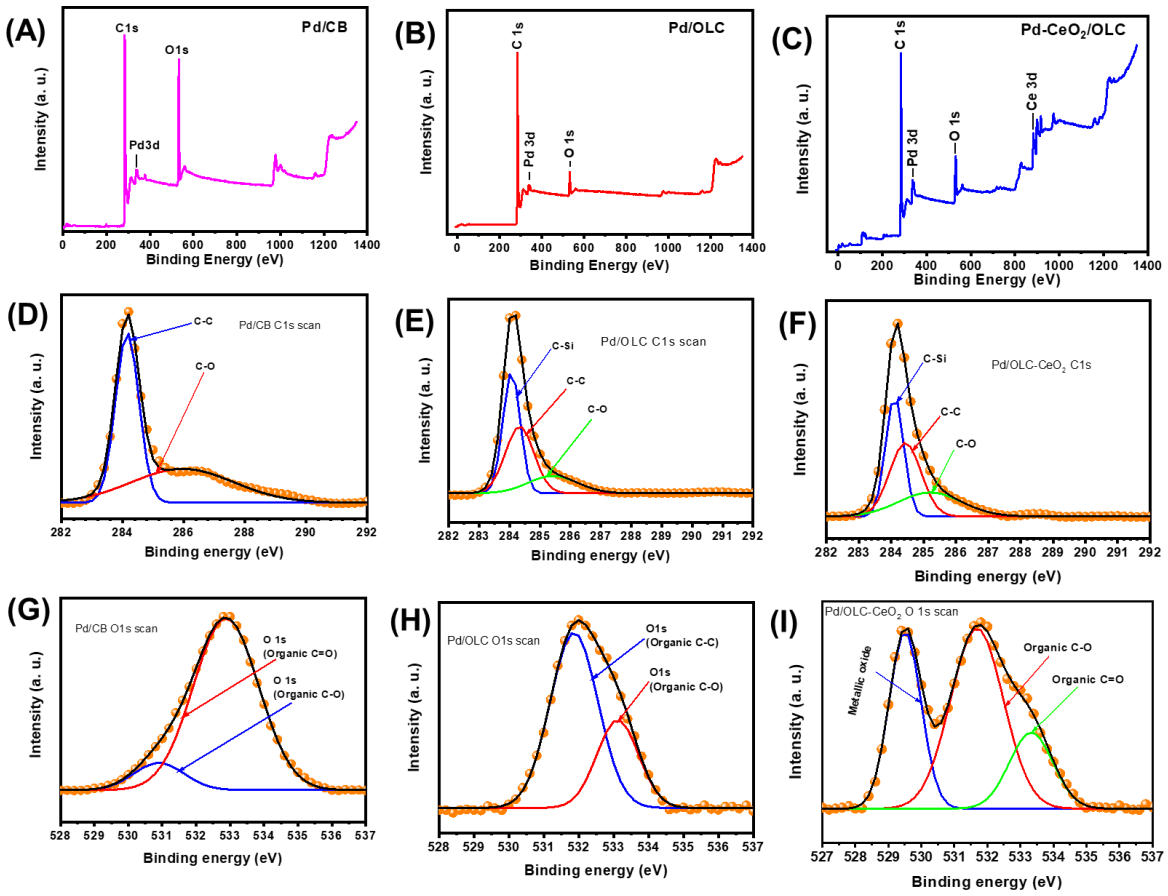


Figure 5.4 XPS data showing the wide spectra of (A) Pd/OLC and (B) Pd/CeO_2-OLC; C 1s scans of (C) Pd/OLC and (D) Pd-CeO_2/OLC; O 1s scans of (E) Pd/OLC and (F) Pd-CeO_2/OLC; Pd 3d scans of (G) Pd/OLC and (H) Pd-CeO_2/OLC; and Ce 3d scan of (I) of Pd-CeO_2/OLC.

The O 1*s* spectra of the Pd/CB (**Figure 5.4G**) and Pd/OLC (**Figure 5.4H)** appear at the expected energy levels (around 532 and 533 eV due to the C-O and C=O organic bonds, respectively). For the Pd-CeO_2/OLC (**Figure 5.4I**), the O 1s peaks deconvolute into four peaks at binding energies of 529.6, 531.59, 533.19 and 534.8 eV associated with the metal oxide bonds, C-O organic, C=O organic bonds, and organic O, respectively.

Figure 5.5 shows the core Pd 3d spectra of the Pd/CB (**Figure 5.5A**), Pd/OLC (**Figure 5.5B**), the Pd(0) $3d_{5/2}$ and $3d_{3/2}$ appear at 335.0 and 340.0 eV, those of the Pd(II) $3d_{5/2}$ and $3d_{3/2}$ appear at 336.6 and 341.8 eV, while those of the PdO $3d_{5/2}$ and $3d_{3/2}$ satellite peaks appear at 338 and 343.2 eV, respectively. The peaks denoted

as $Pd_xCe_yO_z$ seen in **Figure 5.5C** around 337.8 and 342.8 eV relate to Pd(II) or PdO which clearly confirm the formation of a compound between Pd and CeO_2 (in this case, $Ce_{1-x}Pd_xO_{2-\delta}$), which is a similar observation by other workers [38]. The peaks at 335.2 and 340.4 eV are associated with the Pd(0) $3d_{5/2}$ and $3d_{3/2}$, respectively. The observed higher binding energy of Pd3d core levels is a clear indication of the presence of a highly effective charge and formation of a stable solid solution $Ce_{1-x}Pd_xO_{2-\delta}$ [17]. For the Ce 3d spectra in the Pd-CeO_2/OLC (**Figure 5.5D**), the peaks due to Ce^{4+} $3d_{3/2}$ and Ce^{4+} $3d_{5/2}$ are observed at 917, 898.6 and 903.4 eV, respectively. The oxygen vacancies in CeO_2 are expected to improve the dispersion of nanoparticles and favour the electrocatalysis [39]. The peaks due to the Ce^{3+} are located at 886, 882.4, 903.4 and 907.6. These results are consistent with literature [40-42].

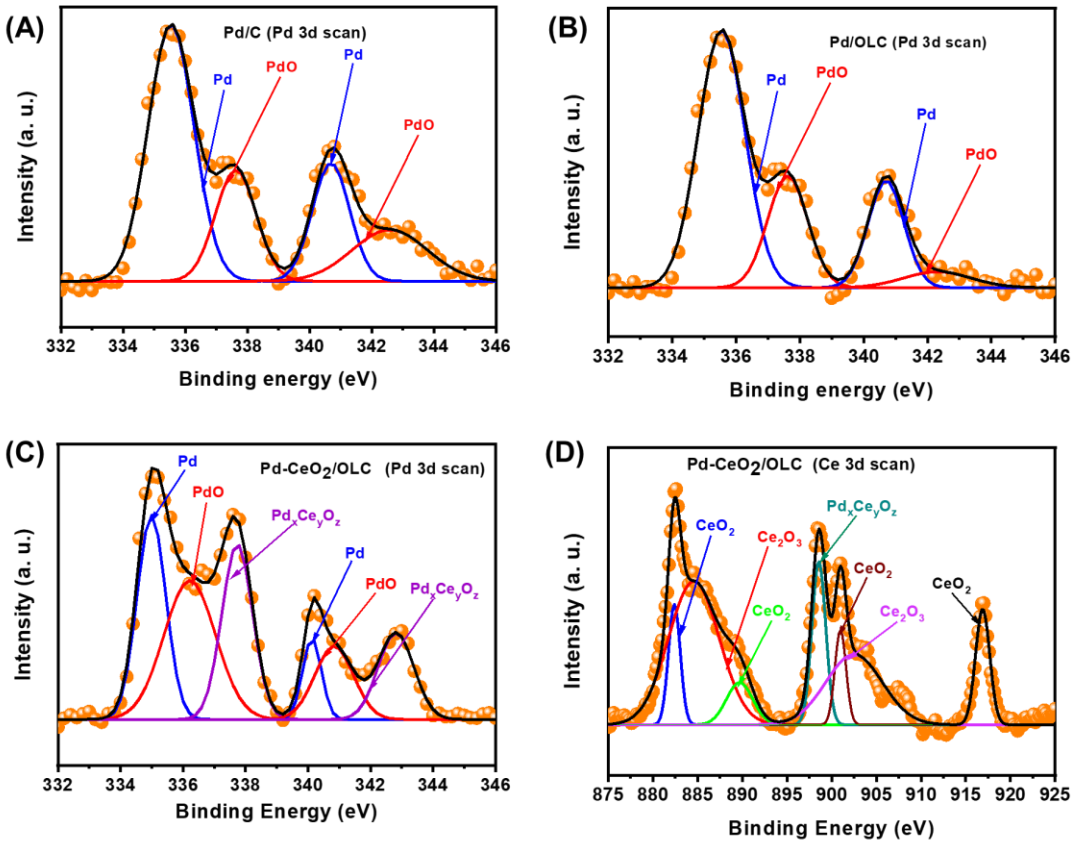


Figure 5.5 XPS data for the core Pd 3d scans of (A) Pd/CB, (B) Pd/OLC, (H) Pd-CeO_2/OLC; and Ce 3d scan of (D) Pd-CeO_2/OLC.

5.3.2 Cyclic voltammetry and EIS: Charge-transfer kinetics

Since this work has not been studied by anyone before, this work first sought to understand the cyclic voltammetric (CV) and EIS properties of the electrode materials in a solution of a redox probe. Figure 5.6 compares the CVs at 20 mVs^{-1} (Figure 5.6A) and Nyquist plots obtained at 0.26 V (vs Ag|AgCl, sat'd KCl) (Figure 5.6B). Table 5.2 summarizes the CV and EIS parameters of the electrodes. The EIS parameters: Rs = ohmic resistance, Rct = charge transfer resistance, CPE = constant phase element, a is the electrode surface roughness and W_d is the Warburg resistance. The electrodes showed perfect reversibility (Ipa/Ipc ≈ 1). The electron transfer kinetics as indicated by the value of the ΔEp and Rct decreases as Pd-CeO2/OLC > Pd/OLC > Pd/CB, indicating the high performance of Pd-CeO2/OLC. The result is attributed to the high specific surface area and high porous volume of the OLC compared to the CB, which corroborate the BET data.

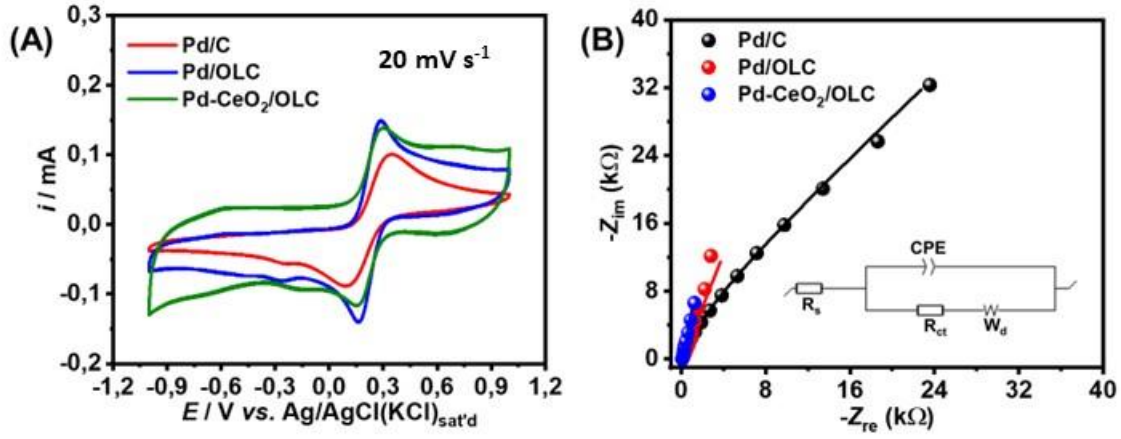


Figure 5.6 Typical comparative (A) cyclic voltammograms at 20 mV s^{-1}, and (B) Nyquist plots of the electrocatalysts immobilized onto GCE surface obtained at 0.22 V (vs Ag|AgCl, 3 M KCl). All data were collected in a redox probe ($[Fe(CN)_6]^{4-}$/$[Fe(CN)_6]^{3-}$ in 0.1 M KCl).

Table 5.2 CV parameters of the OLC- and CB-based electrodes obtained in a solution of redox probe.

CV & EIS data	Pd/C	Pd/OLC	Pd-CeO_2/OLC
E_{pa} / V	0.347	0.285	0.293
E_{pc} / V	0.089	0.159	0.151
ΔE_p / V	0.258	0.222	0.142
$E_{1/2}$ / V	0.220	0.220	0.222
I_{pa} / mA	0.100	0.149	0.138
I_{pc} / mA	-0.088	-0.141	-0.116
I_{pa} / I_{pc}	1.14	1.06	1.19
Rs / Ω	97.10 ± 0.27	96.05 ± 1.23	96.40 ± 0.20
Rct/kΩ	15.85 ± 3.77	2.03 ± 0.95	0.81 ± 0.09
CPE/ nF.$s^{(1-a1)}$	20.05 ± 0.02	124.30 ± 4.05	246.30 ± 0.08
a^1	0.84	0.80	0.90
W_d/ kΩ $s^{-1/2}$	7.25 ± 0.36	1.73 ± 0.42	0.45 ± 0.54

Figure 5.7 shows the CV evolutions at different scan rates and their respective plots of peak current against square root of the scan rates for OLC (Figure 5.7A & B), CB (Figure 5.7C & D) and Pd-CeO_2/OLC (Figure 5.7E & F). The plot of peak current (for both anodic (Ipa / mA) and cathodic (Ipc / mA) versus the square root of scan rate (υ1/2 / (mV/s)1/2) show linear curves (R2 > 0.99), which clearly confirms diffusion-controlled processes in agreement with the Randles-Sevcik theory. The slopes of the plots decrease as Pd/CB > Pd/OLC > Pd-CeO_2/OLC, which confirms the higher performance of the Pd-CeO_2/OLC over the OLC and CB counterparts.

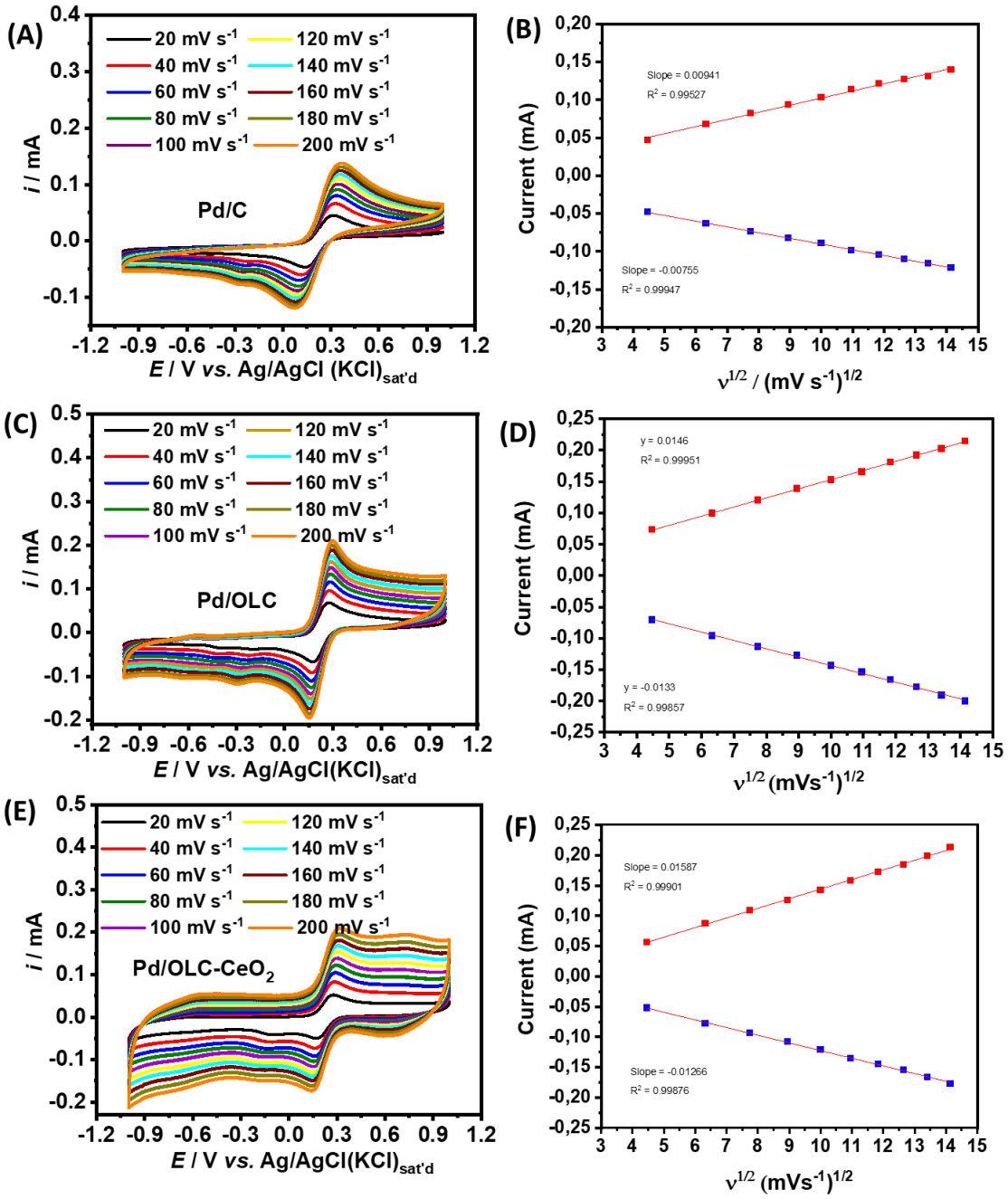


Figure 5.7 Cyclic voltammograms of the electrode at (A) 10 mV/s ansd (B) 150 mV/s; CV at different scan rates (10 – 150 mV/s) for the (C) OLC and (E) CB, and their corresponding plots of peak currents versus square root of scan rate (D) and (F), respectively. All data were collected in a redox probe ($[Fe(CN)_6]^{4-}/[Fe(CN)_6]^{3-}$ in 0.1 M KCl).

5.3.3 Electrocatalytic Oxidation and Detection of Ethanol in Alkaline Medium

The ethanol oxidation reaction was carried out in alkaline electrolyte (potassium hydroxide, KOH) utilizing the Pd-based electrocatalysts (Pd/CB, Pd/OLC and Pd-CeO_2/OLC). First, the Pd-based electrocatalysts' activities in the supporting electrolyte (1.0 M KOH).

Figure 5.8A shows the cyclic voltammograms of the Pd-based electrocatalyst for ethanol oxidation reaction. Well-resolved voltammograms are displayed by all the electrocatalysts with characteristics of hydrogen adsorption / desorption peaks at around -0.6 to -1.0 V *vs.* Ag/AgCl(KCl)$_{sat'd}$, small broad Pd oxidation peak around 0.0 V *vs.* Ag/AgCl(KCl)$_{sat'd}$ and PdO reduction peak at -0.35 V vs. Ag/AgCl(KCl)$_{sat'd}$. The electrochemical active surface area (ECSA) of the electrocatalysts is determined by integrating the PdO reduction peak, following established equation 5.1 below [43].

$$EASA = \frac{Q}{S.I} \qquad (5.1)$$

where *Q* is the coulombic charge (0.0427 mC, 0.0821 mC, and 0.1348 mC for Pd/CB, Pd/OLC, and Pd-CeO_2/OLC, respectively), *S* is the coulombic constant for monolayer of Pd (0.424 mC cm^{-2}), and *I* is the electrocatalytic loading (~ 1.0 μg$_{Pd}$).

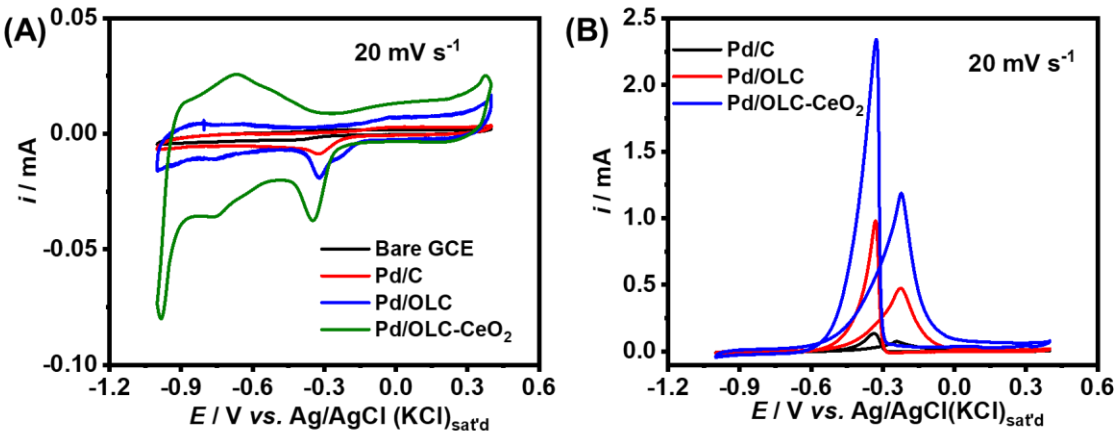


Figure 5.8 Cyclic voltammograms (A) 1.0 M KOH alone and (B) mixture of 1.0 M KOH and 1.0 M ethanol of the Pd-based electrocatalysts.

The ECSA of the Pd/CB, Pd/OLC and Pd-CeO2/OLC recorded are 100.7 cm2 mg-1, 193.6 cm2 mg-1 and 317.9 cm2 mg-1, respectively. The Pd-CeO2/OLC equally has highest ECSA in alkaline supporting electrolyte among the other electrocatalysts, corroborating its activities in the Ferri/Ferrocyanide redox probe. Indeed, the CeO2 modified the electronic property of the Pd catalyst in the Pd-CeO2/OLC for enhanced electrochemical performances. The performance for the electrocatalyst was then investigated towards oxidation of ethanol in the supporting alkaline electrolyte. Figure 5.8B shows the cyclic voltammograms of the electrocatalysts in the mixture of KOH and ethanol. Two distinct oxidation peaks (around - 0.75 V and - 0.3 V) were recorded which are the signature of the oxidation of the ethanol to carbonyl species (i.e., the forward or right peak) and further oxidation of the adsorbed carbonaceous species to carboxylic acid or carbon dioxide (i.e., reverse or left peak). The ratio of the current density value of the forward oxidation peak (jpf) to that of the backward oxidation peak (jpr) was utilized to determine the tolerance of these three electrocatalysts to accumulated carbonaceous intermediates generated during EOR on the electrode surface[44-53]. The higher the ratio (jpf / jpr), the greater the efficiency of the EOR during the forward scan and less accumulation of carbonaceous residues on the electrode surface. The tolerance order is as follows: Pd/CB (0.55) > Pd-CeO2/OLC (0.51) > Pd/OLC (0.48). The improved catalytic activity of the Pd-CeO2/OLC over the pure Pd/OL and Pd/CB may be ascribed to several factors. It is well known that the alloying component tends to leach out under electrochemical conditions and results in a surface rich in the active noble metal [53, 54]. Thus, in this work, it is perhaps not impossible that CeO2 can leach under electrochemical conditions thereby exposing additional active surface compared to the pure monometallic Pd/OLC and Pd/CB. Also, alloying tends to change the

geometric ligand (e.g., diminishes the Pd-Pd bond distance) or electronic impact (e.g., increase in the Pd d-electron vacancies), so one of the components modifies the electronic properties of the other to yield a more active catalytic surface [55-57]. In our latest work[16], we showed that, indeed, CeO2 modulates the electronic state of the Pd-OLC, thereby enhancing the electrocatalysis.

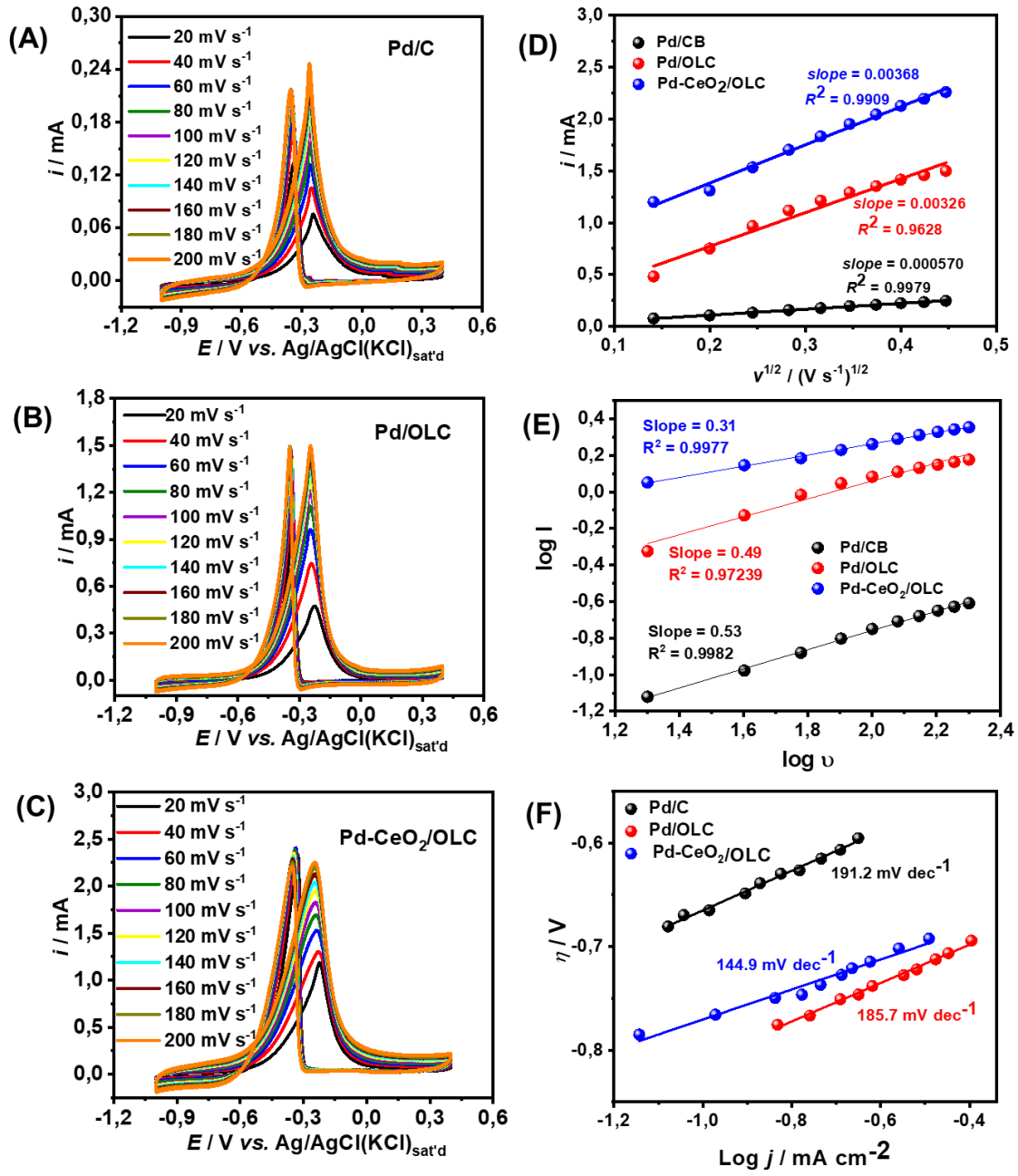


Figure 5.9 (A-C) Scan rate studies and (D) plots of the current against the square root of scan rates of the electrocatalysts toward ethanol oxidation reaction

As can be observed in Figure 5.9, the Pd-CeO_2/OLC, Pd/OLC and Pd/CB have onset potential of -0.68 V, 0.57 V and -0.46 V *vs.* Ag/AgCl$(KCl)_{sat'd}$, respectively. Note that the onset potential (E_{onset}) is related to the breaking of C–H bonds and the consequent removal of intermediates such as CO_{ad} by oxidation with adsorbed OH^- (OH^-_{ad}) provided by Pd–OH and/or Pt–OH sites [58, 59]. The more negative onset potential Pd/OLC-CeO_2 compared to the other two electrocatalysts is an indication that it requires least energy for the oxidation of ethanol. Moreover, the electrocatalysts follow a trend Pd-CeO_2/OLC > Pd/OLC > Pd/CB with respective forward current responses of 1.1875 mA, 0.4886 mA and 0.0773 mA. The increased current response of the Pd-CeO_2/OLC shows that it has the best ethanol oxidation performance among the electrocatalysts studied.

Scan rate studies of the electrocatalysts toward the oxidation ethanol were shown in Figure 5.9A-C, where the current response increased as the scan rates increased. Figure 5.9D show the plots of the peak forward current response to the square root of the scan rates, which gives straight line for all the electrocatalysts with regression close to unity, confirming that the interaction of the ethanol onto the electrodes' surfaces is diffusion-controlled. Also, the logarithmic plot of the forward peak current (log j_{pf}) vs scan rate (υ / mVs^{-1}) increased linearly (**Figure 5.9E**) with slopes between 0.31 and 0.53, further confirming that the electrocatalysis is essentially diffusion-controlled processes. Note that the peak potential of the forward peak (E_{pf} / V) shifts slightly to the positive direction as the scan rate increased, however, the backward peak current did not change with scan rate, which may suggest an improved tolerance to poisoning from carbonaceous intermediates. Tafel slope is a critical parameter that provides an insight into the rate-determining step of the EOR. The

Tafel slopes of the electrocatalysts decreased in the following order: Pd/CB (~191 mV/dec) > Pd/OLC (~ 186 mV/dec) > Pd-CeO2/OLC (~145 mV/dec). Since the values are in the same magnitude, one may conclude the electrocatalysts have same reaction mechanism for the EOR, with the Pd-CeO2/OLC providing the fastest electron transfer kinetics compared to other electrocatalysts.

5.3.4 Reasons for the high performance of the Pd-CeO_2/OLC electrocatalyst towards ethanol oxidation reaction

For the DFT calculation, the Pd (111) was chosen as the model catalyst surface considering that the (111) plane is known to give the highest EOR activity amongst the low-index surfaces. It is also the most prominent surface in the XRD patterns. Also, the choice of Ce (111) and OLC (002) stems from their prevalence in the XRD patterns. The acetyl (CH_3CO*) and hydroxyl (OH*) species were chosen as the adsorbates because it is well established, both by experiments [60, 61] and theory [62, 63], that the EOR follows the formation of acetic acid (CH_3COOH) via the oxidation of the adsorbed CH_3CO* by OH^* species [64], Equation (5.2)

$$CH_3CO^* + OH^* \rightarrow CH_3COOH^* + * \qquad (5.2)$$

Figure 5.10 exemplifies the adsorption of the CH_3CO* on the electrocatalysts' surfaces. The adsorption energy window was set at 100 kcal mol^{-1} and minimum energy difference set at 0.0 kcal mol^{-1}. In the DFT calculation, the adsorption energy, E_{ad} (eV), is defined as (**Equation 5.3**) [16, 65, 66]

$$\boldsymbol{E}_{ad} = (\boldsymbol{E}_{surface + adsorbate}) - (\boldsymbol{E}_{surface} + \boldsymbol{E}_{adsorbate}) \qquad (5.3)$$

where $\boldsymbol{E}_{surface + adsorbate}$ represents the total energy of the interacting catalyst surface and the adsorbate, while $\boldsymbol{E}_{surface} + \boldsymbol{E}_{adsorbate}$ are the energies of the bare catalyst surface and

the free adsorbate in the gas phase. This equation shows that the more negative the $\boldsymbol{E}_{ad}$ value, the stronger the adsorption. The DFT results (summarised in **Table 5.3)** show that the strongest adsorption of CH_3CO^* is observed for the Pd/CB (-25.494 eV) compared to the Pd/OLC (-16-503 eV) and Pd-CeO_2/OLC (-16.811 eV). The weaker adsorption of the CH_3CO^* on the Pd/OLC and Pd-CeO_2/OLC predicts better electrocatalysis on the OLC-based electrodes. The $\boldsymbol{E}_{ad}$ of Pd-CeO_2/OLC is 1.87% higher than that of the Pd/OLC, but this seems to be compensated by the excellent conductivity of the Pd-CeO_2/OLC (i.e., reduced band gap of 0.176 eV vs 0.433 eV). Also, the Pd-CeO_2/OLC shows the weakest adsorption for the OH* (-10.135 eV) compared to Pd/OLC (-10.448 eV) and Pd/CB (-13.116 eV).

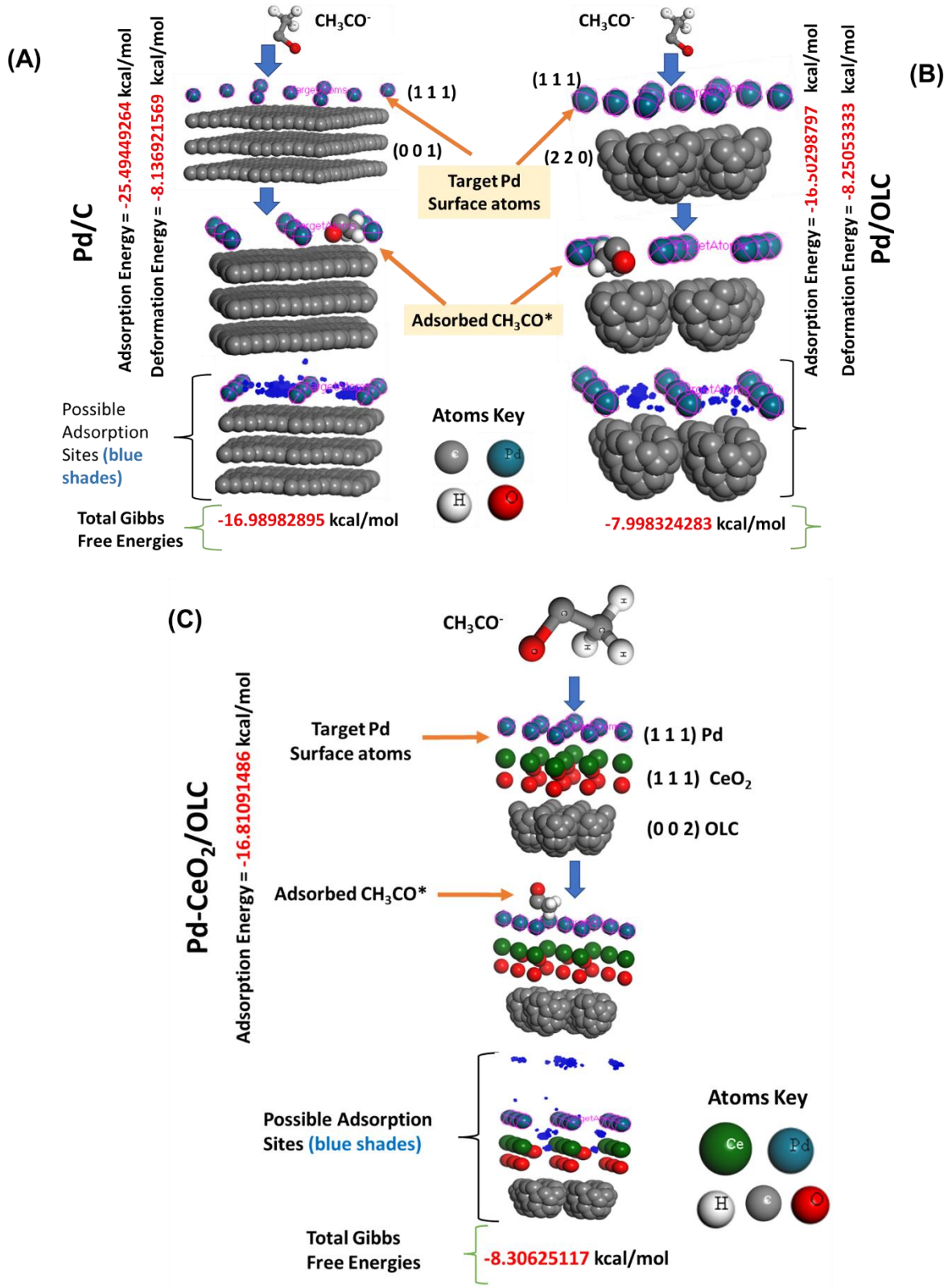


Figure 5.10 Acetyl group adsorption sites at the surfaces of (A) Pd/CB, (B) Pd/OLC and (C) Pd-CeO_2/OLC. The dark blue dots (shades) show the possible site ethanol molecules are adsorbed.

Table 5.4 Predicted energy values from the DFT calculations accompanying the interaction of tramadol with the surfaces of Pd/CB, Pd/OLC and Pd-CeO_2/OLC

Catalyst	Adsorbate	ΔG (eV)	E_{ad} (eV)	E_{def} (eV)	E_g (eV)
Pd/CB	n/a	n/a	n/a	n/a	0.582
	CH_3CO*	-16.990	- 25.494	-8.137	n/a
	OH*	-5.087	-13.116	-8.029	n/a
Pd/OLC	n/a	n/a	n/a	n/a	0.433
	CH_3CO*	-7.998	- 16.503	-8.251	n/a
	OH*	-2.418	-10.448	-8.029	n/a
Pd-CeO_2/OLC	n/a	n/a	n/a	n/a	0.176
	CH_3CO*	-8.306	- 16.811	-8.241	n/a
	OH*	-2.106	-10.135	-8.029	n/a

Key: ΔG = Gibb free energy; E_{ad} = adsorption energy; E_{def} = deformation energy; E_g = energy band gap; n/a = not applicable

The weak adsorption energy between the OH* and Pd-CeO_2/OLC confirms that CeO_2 is an efficient oxygen storage promoter [67], which can speedily supply enough OH species as needed for the fast electrocatalytic kinetics of the EOR. In addition, the bulky nature of the CeO_2 may create some steric hindrance to the Pd thereby mitigate the risk of poisoning the active Pd species.

In addition to the DFT data, it can be observed in Figure 5.11 that both HRTEM and XPS data provide further insights into the reasons for the enhanced performance of the Pd-CeO_2/OLC toward EOR. First, HRTEM shows intimate association of the Pd with the CeO_2, confirming the interfacial interaction between the two species (see **Figure 5.11 A**). Regarding XPS, it has been reported from XPS data how Pd^{2+}/Pd^0 and Ce^{4+}/Ce^{3+}

redox couples interact to keep Pd in its ionic state and, at the same time, allowing the availability of the lattice oxygen for the oxidation reaction [21, 22]. In the solid solution of $Ce_{1-x}Pd_xO_{2-\delta}$, it is either that the Ce^{4+} is reduced to Ce^{3+} or the Pd^{2+} is reduced to Pd^0, or both. However, considering that the electronic configuration of Pd^{2+} ($4d^8\ 5s^0$) means that there is a vacancy in its valence band and, coupled with the fact that it lies below the Ce^{4+}4f band, it simply means that it should be preferentially reduced to Pd(0) rather than the Ce^{4+} to Ce^{3+}. The formation of Pd(0) means that the Pd valence will cross the Ce^{4+}level toward the Fermi level since the addition of electrons tends to move the electronic states much closer to the Fermi energy level [17]. From the XPS data obtained in this work, the Pd-CeO_2/OLC shows slightly higher binding energy of the Pd 3d core energy (i.e., Pd(0) $3d_{5/2}$ at 335.2 eV and Pd(0) $3d_{3/2}$ at 340.4 eV) compared to the Pd/OLC (i.e., Pd(0) $3d_{5/2}$ at 335.0 eV and Pd(0) $3d_{3/2}$ at 340.0 eV), indicating a highly effective charge and formation of a stable $Ce_{1-x}Pd_xO_{2-\delta}$ for the Pd-CeO_2/OLC [17]. Importantly, from the valence band spectra of the catalysts (**Figure 5.11 B-D),** the d-band width increases as Pd/CB (1.04 eV) < Pd/OLC (3.26 eV) < Pd-CeO_2/OLC (9.00 eV). Similarly, the d-band center (ε_d) is shifted downward relative to the Fermi level, i.e., Pd/CB (3.2 eV) < Pd/OLC (3.6 eV) < Pd-CeO_2/OLC (4.2 eV). The broadening of the d-band is indicative of increased compressive strain on the Pd lattice, which leads to an increase in the overlap of the electronic states between the metal atoms (in this case the Pd and Ce). This phenomenon has been observed by other workers too [68, 69]. It is well established in various articles that the positive shift of the Pd 3d core-level and the downshift of the d-band center occur together because of electron loss [69-71]. In fact, the downshift of the d-band center is generally considered highly significant as it suggests a weaker adsorption strength of the adsorbing species on the catalyst's surface (as also predicted by the DFT for both the OLC-based catalysts, **Table 5.4**) which, of

course, is the result of a decreased electron back-donation from the metallic surface to the anti-bonding level of the adsorbed species [56, 68, 72, 73]..

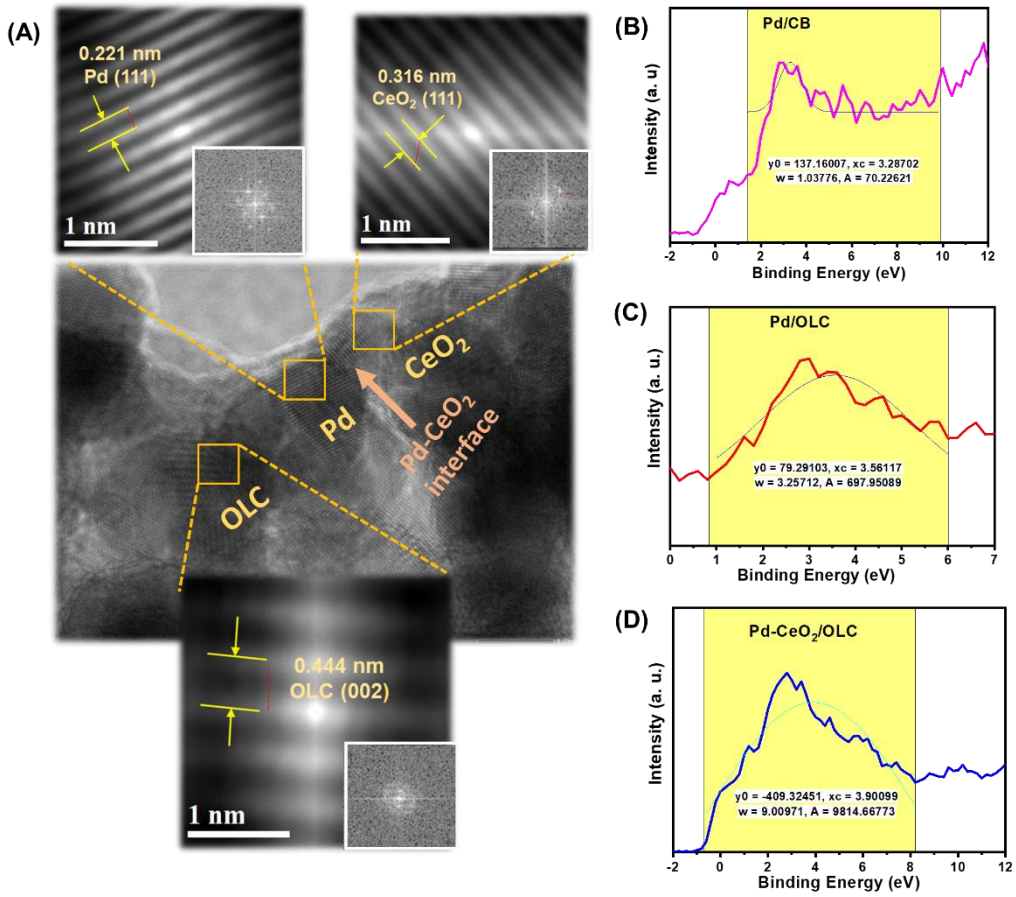


Figure 5.11 HRTEM showing the interfacial interaction between Pd and CeO2 in Pd-CeO_2/OLC, and the valence band spectra of the (B) Pd/CB (C) Pd-CeO2/CB and (D) Pd-CeO_2/OLC catalysts.

In summary, the modulation of the electronic states of the Pd-OLC by CeO2, evident by the enhanced interfacial interaction between the Pd and CeO_2, the increased lattice strain and the downshift of the d-band centre, explain the enhanced electrocatalytic ethanol oxidation reaction. Therefore, the enhanced electrocatalysis of EOR by the Pd-CeO_2/OLC is the results of the strong interfacial interaction of the Pd with the CeO_2-containing OLC. Experiments and theory prove that, unlike the CB, OLC

exhibits strong positive impacts on the electronic states of the Pd-CeO_2, enhancing the electrocatalytic performance of the Pd-CeO_2/OLC

5.3.5 Analytical application of Pd-CeO2/OLC-based electrochemical sensor

5.3.5.1 Alcohol detection in alkaline medium

Since the Pd/OLC-CeO_2 has the best performance for ethanol oxidation reaction, additional experiments for the sensing of ethanol and its detection in commercial beer and wine, as well as interferent studies with serum which mimic the condition in humans. The sensing of alcohol on Pd/OLC-CeO_2 electrocatalyst alone was studied using chronoamperometry (CA) technique. The study was done with a blank (i.e., alkaline electrolyte only without the alcohol) and very low concentrations of alcohol (38.5 mM – 666.7 mM). Figure 5.12A shows the sensing of alcohol at extremely low concentrations on the Pd/OLC-CeO_2 electrocatalyst, which was run for 30 s. It was observed that the current response of the amperometry increase with increasing concentration of the alcohol. Thereafter, a plot of peak current (*i*, µA) at 2.5 s against the ethanol concentrations was made and shown in Figure 5.12B. The equations for the resulting calibration plots were as follows, **Equations 5.4**:

$$I_{pa}\ (\text{mA}) = 0.00024 \pm 0.000\ [\text{Ethanol, mM}] + 0.0144 \pm 0.001\ (R^2 = 0.9990) \qquad (5.4)$$

The electrode shows better linearity in the range of 38.5 – 286 mM, sensitivity (*m* = 0.00024 mA mM^{-1}) and limit of detection (LoD ~ 8.7 mM, determined from LoD = 3 *s/m*, where *s* is the standard deviation of the blank or y-intercept. The values were calculated as the average of five electrodes.

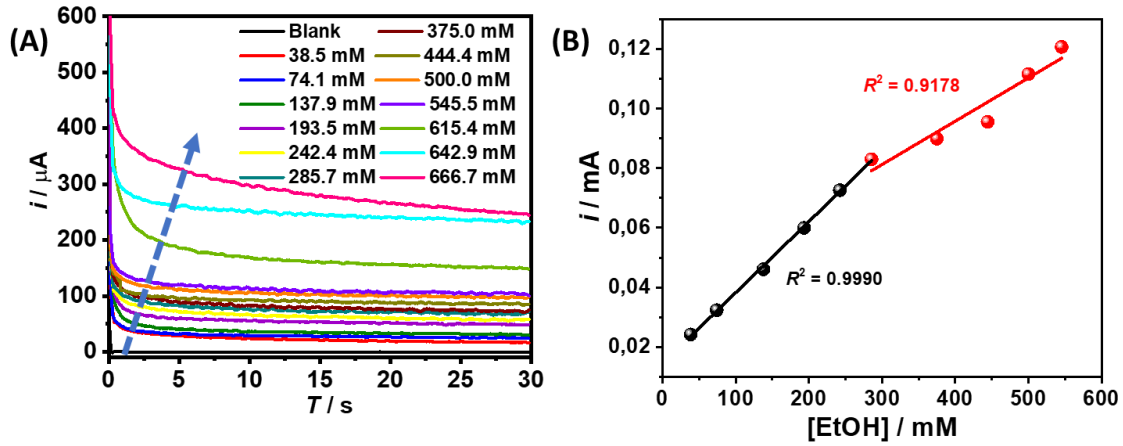


Figure 2.12 (A) Typical chronoamperometric curves obtained in 1 M KOH containing different concentrations of ethanol (0 – 666.7 mM), and (B) plot of peak current response versus concentration of ethanol.

5.3.5.2 Determination of ethanol in real alcoholic samples

To demonstrate the possibility of the GCE/Pd-CeO_2/OLC as a potential electrocatalyst for the detection of alcohol in real samples such as commercial beer (Amstel® beer), commercial wine (Nederberg® wine) and human serum were tested using the standard addition method. Each sample was tested five consecutive times and quantified using the standard linear plots. Relatively high recoveries (89 – 108 %) were achieved as summarized in Table 3, confirming that the Pd-CeO_2/OLC-based electrocatalyst has the potential to be developed as a viable electrocatalytic sensing platform for a variety of alcohol samples.

Table 5.5 Summary of results obtained in this work for electrochemical sensing of tramadol, using the DPV method

Sample	**Added (mM)**	**Detected (mM)**	**Recovery (%)**	**RSD (%)**
Human Serum	167	180	107.8	6.3
Commercial Beer (Amstel®)	91	81	89.0	7.2
Commercial Wine (Nederberg®)	193	184	95.3	5.4

5.4 Conclusion

This study has clearly proven that Pd-CeO2/OLC is the best performing electrocatalyst for EOR and ethanol detection in alkaline electrolyte. DFT calculations, which is supported by HRTEM and XPS data, predict that this high performance may be attributed to the modulation of the electronic properties of the Pd-OLC interface.

5.5 References

1) K.I. Ozoemena, Nanostructured platinum-free electrocatalysts in alkaline direct alcohol fuel cells: catalyst design, principles and applications, RSC advances, 6 (2016) 89523-89550.
2) G. Possetti, L. Côcco, C. Yamamoto, L. De Arruda, R. Falate, M. Muller, J. Fabris, Application of a long-period fibre grating-based transducer in the fuel industry, Measurement Science and Technology, 20 (2009) 034012.
3) H. Lidén, A. Vijayakumar, L. Gorton, G. Marko-Varga, Rapid alcohol determination in plasma and urine by column liquid chromatography with biosensor detection, Journal of pharmaceutical and biomedical analysis, 17 (1998) 1111-1128.
4) F. Mehrjo, M. Hashemi, Z. Solati, S. Hashemnia, Biosynthesis of ZnO Nanosheets Decorated with Pd Nanoparticles and Their Application for Electrochemical Investigation of Ethanol, Electrocatalysis, 12 (2021) 272-282.
5) E. Tavakolian, J. Tashkhourian, Z. Razmi, H. Kazemi, M. Hosseini-Sarvari, Ethanol electrooxidation at carbon paste electrode modified with Pd–ZnO nanoparticles, Sensors and Actuators B: Chemical, 230 (2016) 87-93.
6) J. Shi, P. Ci, F. Wang, H. Peng, P. Yang, L. Wang, Q. Wang, P.K. Chu, Pd/Ni/Si-microchannel-plate-based amperometric sensor for ethanol detection, Electrochimica Acta, 56 (2011) 4197-4202.
7) B.R. Adhikari, H. Schraft, A. Chen, A high-performance enzyme entrapment platform facilitated by a cationic polymer for the efficient electrochemical sensing of ethanol, Analyst, 142 (2017) 2595-2602.
8) E.T.H.B.K.B.H.B.M. AhmedGalal, An amperometric aqueous ethanol sensor based on the electrocatalytic oxidation at a cobalt-nickel oxide electrode,

Electrochimica Acta, 41 (1996) 337-344.

9) S. Cinti, M. Basso, D. Moscone, F. Arduini, A paper-based nanomodified electrochemical biosensor for ethanol detection in beers, Anal Chim Acta, 960 (2017) 123-130.

10) C. Xu, F. Sun, H. Gao, J. Wang, Nanoporous platinum-cobalt alloy for electrochemical sensing for ethanol, hydrogen peroxide, and glucose, Anal Chim Acta, 780 (2013) 20-27.

11) E.P. Nascimento, H.C. Firmino, A.M. Santos, H.B. Sales, V.D. Silva, D.A. Macedo, G.A. Neves, E.S. Medeiros, R.R. Menezes, Facile synthesis of hollow F-doped SnO2 nanofibers and their efficiency in ethanol sensing, Journal of the American Ceramic Society, 104 (2021) 1297-1308.

12) S. Prasanna Kumar, L. Parashuram, D.P. Suhas, P. Krishnaiah, Carboxylated graphene-alcohol oxidase thin films modified graphite electrode as an electrochemical sensor for electro-catalytic detection of ethanol, Materials Science for Energy Technologies, 3 (2020) 159-166.

13) R. Othman, A.L. Dicks, Z. Zhu, Non precious metal catalysts for the PEM fuel cell cathode, International journal of hydrogen energy, 37 (2012) 357-372.

14) S. Badwal, S. Giddey, A. Kulkarni, J. Goel, S. Basu, Direct ethanol fuel cells for transport and stationary applications–A comprehensive review, Applied Energy, 145 (2015) 80-103.

15) C. Bianchini, P.K. Shen, Palladium-based electrocatalysts for alcohol oxidation in half cells and in direct alcohol fuel cells, Chemical reviews, 109 (2009) 4183-4206.

16) J.J. Ogada, A.K. Ipadeola, P.V. Mwonga, A.B. Haruna, F. Nichols, S. Chen, H.A. Miller, M.V. Pagliaro, F. Vizza, J.R. Varcoe, CeO2 Modulates the

Electronic States of a Palladium Onion-Like Carbon Interface into a Highly Active and Durable Electrocatalyst for Hydrogen Oxidation in Anion-Exchange-Membrane Fuel Cells, ACS Catalysis, 12 (2022) 7014-7029.

17) M.S. Hegde, P. Bera, Noble metal ion substituted CeO2 catalysts: Electronic interaction between noble metal ions and CeO2 lattice, Catalysis Today, 253 (2015) 40-50.

18) E. Slavinskaya, A. Boronin, I. Danilova, Y.I. Amosov, A. Ivanova, P. Kuznetsov, I. Polukhina, R. Gulyaev, A. Stadnichenko, S. Koshcheev, Synthesis and physicochemical characterization of palladium-cerium oxide catalysts for the low-temperature oxidation of carbon monoxide, Kinetics and Catalysis, 50 (2009) 819-823.

19) R. Gulyaev, E. Slavinskaya, S. Novopashin, D. Smovzh, A. Zaikovskii, D.Y. Osadchii, O. Bulavchenko, S. Korenev, A. Boronin, Highly active PdCeOx composite catalysts for low-temperature CO oxidation, prepared by plasma-arc synthesis, Applied Catalysis B: Environmental, 147 (2014) 132-143.

20) P.M. Ejikeme, K. Makgopa, K. Raju, K.I. Ozoemena, Promotional Effects of Nanodiamond-Derived Onion-Like Carbons on the Electrocatalytic Properties of Pd-MnO2 for the Oxidation of Glycerol in Alkaline Medium, ChemElectroChem, 3 (2016) 2243-2251.

21) S. Sharma, B.D. Mukri, M.S. Hegde, Direct evidence of redox interaction between metal ion and support oxide in Ce(0.98)Pd(0.02)O(2-delta) by a combined electrochemical and XPS study, Dalton Trans, 40 (2011) 11480-11489.

22) S. Sharma, M. Hegde, Pt metal-CeO 2 interaction: Direct observation of redox coupling between Pt 0/Pt 2+/Pt 4+ and Ce 4+/Ce 3+ states in Ce 0.98 Pt 0.02

O 2− δ catalyst by a combined electrochemical and X-ray photoelectron spectroscopy study, The Journal of chemical physics, 130 (2009) 114706.

23) M. Hantel, V. Presser, J. McDonough, G. Feng, P.T. Cummings, Y. Gogotsi, R. Kötz, In situ electrochemical dilatometry of onion-like carbon and carbon black, Journal of the Electrochemical Society, 159 (2012) A1897.

24) H.A. Miller, F. Vizza, M. Marelli, A. Zadick, L. Dubau, M. Chatenet, S. Geiger, S. Cherevko, H. Doan, R.K. Pavlicek, S. Mukerjee, D.R. Dekel, Highly active nanostructured palladium-ceria electrocatalysts for the hydrogen oxidation reaction in alkaline medium, Nano Energy, 33 (2017) 293-305.

25) A.K. Ipadeola, N.Z. Lisa Mathebula, M.V. Pagliaro, H.A. Miller, F. Vizza, V. Davies, Q. Jia, F. Marken, K.I. Ozoemena, Unmasking the Latent Passivating Roles of Ni (OH) 2 on the Performance of Pd–Ni Electrocatalysts for Alkaline Ethanol Fuel Cells, ACS Applied Energy Materials, 3 (2020) 8786-8802.

26) T.P. Mofokeng, A.K. Ipadeola, Z.N. Tetana, K.I. Ozoemena, Defect-engineered nanostructured Ni/MOF-derived carbons for an efficient aqueous battery-type energy storage device, ACS omega, 5 (2020) 20461-20472.

27) J.-G. Li, C.-Y. Tsai, S.-W. Kuo, Fabrication and characterization of inorganic silver and palladium nanostructures within hexagonal cylindrical channels of mesoporous carbon, Polymers, 6 (2014) 1794-1809.

28) S. Jiao, X. Fu, S. Wang, Y. Zhao, Perfecting electrocatalysts via imperfections: towards the large-scale deployment of water electrolysis technology, Energy & Environmental Science, 14 (2021) 1722-1770.

29) G. He, Y. Song, K. Liu, A. Walter, S. Chen, S. Chen, Oxygen reduction catalyzed by platinum nanoparticles supported on graphene quantum dots, Acs Catalysis, 3 (2013) 831-838.

30) Y. Song, S. Chen, Graphene quantum-dot-supported platinum nanoparticles: defect-mediated electrocatalytic activity in oxygen reduction, ACS applied materials & interfaces, 6 (2014) 14050-14060.

31) X.-M. Lin, L.-P. Li, G.-S. Li, W.-H. Su, Transport property and Raman spectra of nanocrystalline solid solutions Ce0. 8Nd0. 2O2− δ with different particle size, Materials Chemistry and Physics, 69 (2001) 236-240.

32) W. Weber, K. Hass, J. McBride, Raman study of CeO 2: Second-order scattering, lattice dynamics, and particle-size effects, Physical Review B, 48 (1993) 178.

33) J. McBride, K. Hass, B. Poindexter, W. Weber, Raman and x-ray studies of Ce1− x RE x O2− y, where RE= La, Pr, Nd, Eu, Gd, and Tb, Journal of Applied Physics, 76 (1994) 2435-2441.

34) S. Loridant, Raman spectroscopy as a powerful tool to characterize ceria-based catalysts, Catalysis Today, 373 (2021) 98-111.

35) V. Bambagioni, C. Bianchini, Y. Chen, J. Filippi, P. Fornasiero, M. Innocenti, A. Lavacchi, A. Marchionni, W. Oberhauser, F. Vizza, Energy Efficiency Enhancement of Ethanol Electrooxidation on Pd–CeO2/C in Passive and Active Polymer Electrolyte-Membrane Fuel Cells, ChemSusChem, 5 (2012) 1266-1273.

36) K. Li, T. Lyu, J. He, B.W. Jang, Selective hydrogenation of acetylene over Pd/CeO2, Frontiers of Chemical Science and Engineering, 14 (2020) 929-936.

37) P. Venkataswamy, D. Damma, D. Jampaiah, D. Mukherjee, M. Vithal, B.M. Reddy, Cr-doped CeO2 nanorods for CO oxidation: insights into promotional effect of Cr on structure and catalytic performance, Catalysis Letters, 150

(2020) 948-962.

38) S. Chen, S. Li, R. You, Z. Guo, F. Wang, G. Li, W. Yuan, B. Zhu, Y. Gao, Z. Zhang, H. Yang, Y. Wang, Elucidation of Active Sites for CH4 Catalytic Oxidation over Pd/CeO2 Via Tailoring Metal–Support Interactions, ACS Catalysis, 11 (2021) 5666-5677.

39) J. Wang, B. Li, T. Yersak, D. Yang, Q. Xiao, J. Zhang, C. Zhang, Recent advances in Pt-based octahedral nanocrystals as high performance fuel cell catalysts, Journal of Materials Chemistry A, 4 (2016) 11559-11581.

40) A. Arumugam, C. Karthikeyan, A.S.H. Hameed, K. Gopinath, S. Gowri, V. Karthika, Synthesis of cerium oxide nanoparticles using Gloriosa superba L. leaf extract and their structural, optical and antibacterial properties, Materials Science and Engineering: C, 49 (2015) 408-415.

41) G. Wang, Q. Mu, T. Chen, Y. Wang, Synthesis, characterization and photoluminescence of CeO2 nanoparticles by a facile method at room temperature, Journal of Alloys and Compounds, 493 (2010) 202-207.

42) S. Song, K. Wang, L. Yan, A. Brouzgou, Y. Zhang, Y. Wang, P. Tsiakaras, Ceria promoted Pd/C catalysts for glucose electrooxidation in alkaline media, Applied Catalysis B: Environmental, 176-177 (2015) 233-239.

43) D. Rand, R. Woods, The nature of adsorbed oxygen on rhodium, palladium and gold electrodes, Journal of Electroanalytical Chemistry and Interfacial Electrochemistry, 31 (1971) 29-38.

44) M.B. Rohwer, K. Ozoemena, R.M. Modibedi, Microwave-assisted pechini synthesis of Pd-Ni nanocatalyst for ethanol electro-oxidation in alkaline medium, Research space (2012). http://researchspace.csir.co.za/dspace/handle/10204/7796

45) T. Ramulifho, K.I. Ozoemena, R.M. Modibedi, C.J. Jafta, M.K. Mathe, Electrocatalytic oxidation of ethylene glycol at palladium-bimetallic nanocatalysts (PdSn and PdNi) supported on sulfonate-functionalised multi-walled carbon nanotubes, Journal of Electroanalytical Chemistry, 692 (2013) 26-30.

46) T. Ramulifho, K.I. Ozoemena, R.M. Modibedi, C.J. Jafta, M.K. Mathe, Fast microwave-assisted solvothermal synthesis of metal nanoparticles (Pd, Ni, Sn) supported on sulfonated MWCNTs: Pd-based bimetallic catalysts for ethanol oxidation in alkaline medium, Electrochimica Acta, 59 (2012) 310-320.

47) N.E. Mphahlele, A.K. Ipadeola, A.B. Haruna, P.V. Mwonga, R.M. Modibedi, N. Palaniyandy, C. Billing, K.I. Ozoemena, Microwave-induced defective PdFe/C nano-electrocatalyst for highly efficient alkaline glycerol oxidation reactions, Electrochimica Acta, 409 (2022) 139977.

48) O.O. Fashedemi, H.A. Miller, A. Marchionni, F. Vizza, K.I. Ozoemena, Electro-oxidation of ethylene glycol and glycerol at palladium-decorated FeCo@ Fe core–shell nanocatalysts for alkaline direct alcohol fuel cells: functionalized MWCNT supports and impact on product selectivity, Journal of Materials Chemistry A, 3 (2015) 7145-7156.

49) O.O. Fashedemi, K.I. Ozoemena, Comparative electrocatalytic oxidation of ethanol, ethylene glycol and glycerol in alkaline medium at Pd-decorated FeCo@ Fe/C core-shell nanocatalysts, Electrochimica Acta, 128 (2014) 279-286.

50) A.K. Ipadeola, R. Barik, S.C. Ray, K.I. Ozoemena, Bimetallic Pd/SnO2 nanoparticles on metal organic framework (MOF)-derived carbon as electrocatalysts for ethanol oxidation, Electrocatalysis, 10 (2019) 366-380.

51) N.W. Maxakato, C.J. Arendse, K.I. Ozoemena, Insights into the electro-oxidation of ethylene glycol at Pt/Ru nanocatalysts supported on MWCNTs: Adsorption-controlled electrode kinetics, Electrochemistry Communications, 11 (2009) 534-537.

52) R.M. Modibedi, T. Mehlo, K.I. Ozoemena, M.K. Mathe, Preparation, characterisation and application of Pd/C nanocatalyst in passive alkaline direct ethanol fuel cells (ADEFC), International Journal of Hydrogen Energy, 40 (2015) 15605-15612.

53) K.M. Hassan, A.A. Hathoot, R. Maher, M. Abdel Azzem, Electrocatalytic oxidation of ethanol at Pd, Pt, Pd/Pt and Pt/Pd nano particles supported on poly 1,8-diaminonaphthalene film in alkaline medium, RSC Adv, 8 (2018) 15417-15426.

54) H. Ji, J. Frenzel, Z. Qi, X. Wang, C. Zhao, Z. Zhang, G. Eggeler, An ultrafine nanoporous bimetallic Ag–Pd alloy with superior catalytic activity, CrystEngComm, 12 (2010) 4059-4062.

55) H. Yang, W. Vogel, C. Lamy, N. Alonso-Vante, Structure and electrocatalytic activity of carbon-supported Pt− Ni alloy nanoparticles toward the oxygen reduction reaction, The Journal of Physical Chemistry B, 108 (2004) 11024-11034.

56) Y. Suo, L. Zhuang, J. Lu, First-principles considerations in the design of Pd-Alloy catalysts for oxygen reduction, Angewandte Chemie, 119 (2007) 2920-2922.

57) X. Yang, Q. Yang, J. Xu, C.-S. Lee, Bimetallic PtPd nanoparticles on Nafion–graphene film as catalyst for ethanol electro-oxidation, Journal of Materials Chemistry, 22 (2012) 8057-8062.

58) S. Wang, S.P. Jiang, T. White, J. Guo, X. Wang, Electrocatalytic activity and interconnectivity of Pt nanoparticles on multiwalled carbon nanotubes for fuel cells, The Journal of Physical Chemistry C, 113 (2009) 18935-18945.

59) B. Habibi, S. Mohammadyari, Facile synthesis of Pd nanoparticles on nano carbon supports and their application as an electrocatalyst for oxidation of ethanol in alkaline media: the effect of support, International Journal of Hydrogen Energy, 40 (2015) 10833-10846.

60) E.A. Monyoncho, S.N. Steinmann, C. Michel, E.A. Baranova, T.K. Woo, P. Sautet, Ethanol electro-oxidation on palladium revisited using polarization modulation infrared reflection absorption spectroscopy (PM-IRRAS) and density functional theory (DFT): why is it difficult to break the C–C bond?, ACS Catalysis, 6 (2016) 4894-4906.

61) W. Du, K.E. Mackenzie, D.F. Milano, N.A. Deskins, D. Su, X. Teng, Palladium–tin alloyed catalysts for the ethanol oxidation reaction in an alkaline medium, Acs Catalysis, 2 (2012) 287-297.

62) M. Li, W. Guo, R. Jiang, L. Zhao, H. Shan, Decomposition of ethanol on Pd (111): a density functional theory study, Langmuir, 26 (2010) 1879-1888.

63) E. Wang, J. Xu, T. Zhao, Density functional theory studies of the structure sensitivity of ethanol oxidation on palladium surfaces, The Journal of Physical Chemistry C, 114 (2010) 10489-10497.

64) B. Miao, Z.-P. Wu, H. Xu, M. Zhang, Y. Chen, L. Wang, DFT studies on the key competing reaction steps towards complete ethanol oxidation on transition metal catalysts, Computational Materials Science, 156 (2019) 175-186.

65) T. Yang, S. Yang, W. Jin, Y. Zhang, N. Barsan, A. Hemeryck, S. Wageh, A.A.

Al-Ghamdi, Y. Liu, J. Zhou, W. Chen, H. Zhang, Density Functional Investigation on alpha-MoO3 (100): Amines Adsorption and Surface Chemistry, ACS Sens, 7 (2022) 1213-1221.

66) P. Wang, X. Yuan, Z. Cui, C. Xu, Z. Sun, J. Li, J. Liu, Y. Tian, H. Li, A Nanometer-Sized Graphite/Boron-Doped Diamond Electrochemical Sensor for Sensitive Detection of Acetaminophen, ACS Omega, 6 (2021) 6326-6334.

67) Q. Yuan, H.H. Duan, L.L. Li, L.D. Sun, Y.W. Zhang, C.H. Yan, Controlled synthesis and assembly of ceria-based nanomaterials, J Colloid Interface Sci, 335 (2009) 151-167.

68) M. Ren, Y. Zhou, F. Tao, Z. Zou, D.L. Akins, H. Yang, Controllable Modification of the Electronic Structure of Carbon-Supported Core–Shell Cu@Pd Catalysts for Formic Acid Oxidation, The Journal of Physical Chemistry C, 118 (2014) 12669-12675.

69) S. Hu, L. Scudiero, S. Ha, Electronic effect on oxidation of formic acid on supported Pd–Cu bimetallic surface, Electrochimica Acta, 83 (2012) 354-358.

70) C.J. Corcoran, H. Tavassol, M.A. Rigsby, P.S. Bagus, A. Wieckowski, Application of XPS to study electrocatalysts for fuel cells, Journal of Power Sources, 195 (2010) 7856-7879.

71) W.P. Zhou, A. Lewera, R. Larsen, R.I. Masel, P.S. Bagus, A. Wieckowski, Size effects in electronic and catalytic properties of unsupported palladium nanoparticles in electrooxidation of formic acid, The Journal of Physical Chemistry B, 110 (2006) 13393-13398.

72) P. Strasser, S. Koh, T. Anniyev, J. Greeley, K. More, C. Yu, Z. Liu, S. Kaya, D. Nordlund, H. Ogasawara, M.F. Toney, A. Nilsson, Lattice-strain control of the activity in dealloyed core-shell fuel cell catalysts, Nat Chem, 2 (2010) 454-

460.

73) J.K. Nørskov, T. Bligaard, J. Rossmeisl, C.H. Christensen, Towards the computational design of solid catalysts, Nature chemistry, 1 (2009) 37-46.

CHAPTER 6

CONCLUSIONS AND RECOMMENDATIONS

6.1 Electrocatalytic Sensing of Tramadol

This work describes the first report on the use of OLC (vs conductive carbon black) as an electrode platform for the detection of tramadol, an important drug of abuse. OLC-modified glassy carbon electrode (GCE-OLC) shows wide linear concentration range for tramadol (*ca.* 55 – 392 μM) with high sensitivity and low limit of detection and quantification. OLC-modified screen-printed electrode (SPE-OLC) was successfully deployed in the determination of tramadol in human serum samples and pharmaceutical formulation. The OLC-based electrochemical sensor promises to be useful for sensitive and accurate detection of tramadol in clinics, quality control and routine quantification of tramadol drugs in pharmaceutical formulations. Theoretical calculations (DFT) predicted that OLC (and possibly spherically shaped carbons) rather than conductive carbon black (and possibly other flat-shaped carbons such as graphene) are the most likely carbon electrodes for the sensitive electrocatalytic detection of tramadol.

This work has opened doors for future research; thus the following **recommendations** should be considered:

(i) Further work is needed to explore other carbon models or morphologies such as nanotubes, diamond-shaped, nanofibres, nanowires, fishbones, and many other morphologies for the sensitive detection of tramadol and related drugs.

(ii) Given the high sensitivity of the OLC, future research on modification with low-cost transition metal oxides should be considered.

(iii) The sensitivity of the OLC-based electrodes for the sensing of tramadol and related drugs should be optimized and use a more sensitive electrochemical technique such as chronoamperometry.

(iv) More drugs of abuse (such as cocaine, codeine, methamphetamine, etc) should be explored with OLC-based electrochemical sensors.

(v) There is a need to fabricate electrochemical microsensor as a diagnostic device for tramadol and other drugs of abuse.

6.2 Electrocatalytic Sensing of Alcohol

This research studied the electrocatalytic properties of palladium catalysts supported on CB, OLC and CeO2/OLC (i.e., Pd/CB, Pd/OLC and Pd-CeO2/OLC) towards the oxidation of ethanol (EtOH) in alkaline medium. The presence of CeO2 significantly enhanced anodic performance of the two carbon supports. GCE/Pd-CeO2/OLC showed the best performance of ethanol oxidation reaction in terms of current densities (highest current density), smaller peak-to-peak separation (faster electron transport), higher jf/jb value (less poisoning from products of the intermediate reaction) and the lowest resistance to current flow as seen in the EIS results. DFT calculation, supported by XPS and HRTEM data, predicted that this high activity is due to the presence of CeO2 that modulated the electronic properties of the pristine Pd/OLC catalyst. Based on the above results, the GCE/Pd-CeO2/OLC catalyst was then employed for the detection of ethanol which gave wide linear range of 38.5 – 286 mM, sensitivity (m = 0.00024 mA mM-1) and limit of detection (LoD) of ~ 8.7 mM. The GCE/Pd-CeO2/OLC shows potential; for use in real samples of commercial alcoholic beverages and human serum, with satisfactory recoveries (89 – 108 %).

This work has opened doors for future research; thus the following **recommendations** should be considered:

(i) Given the high sensitivity of the Pd-CeO_2/OLC towards EOR and sensing of ethanol, future research on other lanthanides other than cerium could be explored.

(ii) The sensitivity of the Pd-CeO_2/OLC-based electrodes for the sensing of ethanol should be optimized and related drugs should be optimized by using a more sensitive electrochemical technique such as chronoamperometry.

(iii) It would be interesting to explore and fabricate electrochemical microsensor as a diagnostic device for the detection ethanol gas in human breath as breathalyzer (for catching drunk drivers).

APPENDIX

CALCULATION FOR CONCENTRATIONS OF ETHANOL

HIGH CONCENTRATION

1) Calculation of the concentrations of EtOH added from the stock solution (D; 1.0 M EtOH in 1.0 M KOH) to 25 mL of 1.0 M KOH electrolyte

Add 1.0 mL of stock solution for 1st – 5th addition

1st addition, $C_{initial}$ = 1.0 M; $V_{initial}$ = 1.0 mL = 0.001 mL; V_{new} = (25.0 + 1.0) mL = 26.0 mL = 0.026 L

$$C_{new} = \frac{C_{initial}\, x V_{initial}}{Vnew} = \frac{1.0\ M\ x\ 0.001\ L}{0.026\ L} = 0.038462\ M = 38.462\ mM = 0.2247\ \%$$

Note the formular for converting Molar to %

% EtOH = C_m x 100 % x $\frac{\text{Molar mass}}{\text{density}}$= 0.038462 M x 100 % x $\frac{46.07\ \text{g mol}^{-1}}{789.3\ \text{g L}^{-1}}$ = 0.2247 %

2nd addition, $C_{initial}$ = 1.0 M; $V_{initial}$ = 2.0 mL = 0.002 mL; V_{new} = (26.0 + 1.0) mL = 27.0 mL = 0.0270 L

$$C_{new} = \frac{C_{initial}\, x V_{initial}}{Vnew} = \frac{1.0\ M\ x\ 0.002\ L}{0.0270\ L} = 0.074074\ M = 74.074\ mM = 0.4328\ \%$$

Note the formular for converting Molar to %

% EtOH = C_m x 100 % x $\frac{\text{Molar mass}}{\text{density}}$= 0.074074 M x 100 % x $\frac{46.07\ \text{g mol}^{-1}}{789.3\ \text{g L}^{-1}}$ = 0.4328 %

3rd addition, $C_{initial}$ = 1.0 M; $V_{initial}$ = 3.0 mL = 0.003 mL; V_{new} = (27.0 + 1.0) mL = 28.0 mL = 0.0280 L

$$C_{new} = \frac{C_{initial}\, x V_{initial}}{Vnew} = \frac{1.0\ M\ x\ 0.003\ L}{0.0280\ L} = 0.107143\ M = 107.143\ mM = 0.6260\ \%$$

Note the formular for converting Molar to %

% EtOH = C_m x 100 % x $\frac{\text{Molar mass}}{\text{density}}$= 0.107143 M x 100 % x $\frac{46.07\ \text{g mol}^{-1}}{789.3\ \text{g L}^{-1}}$ = 0.6260 %

4th addition, $C_{initial}$ = 1.0 M; $V_{initial}$ = 4.0 mL = 0.004 mL; V_{new} = (28.0 + 1.0) mL = 29.0 mL = 0.0290 L

$$C_{new} = \frac{C_{initial}\, x V_{initial}}{Vnew} = \frac{1.0\ M\ x\ 0.0040\ L}{0.0290\ L} = 0.137931\ M = 137.931\ mM = 0.8059\ \%$$

Note the formular for converting Molar to %

% EtOH = C_m x 100 % x $\frac{\text{Molar mass}}{\text{density}}$= 0.137931 M x 100 % x $\frac{46.07\ \text{g mol}^{-1}}{789.3\ \text{g L}^{-1}}$ = 0.8059 %

5th addition, $C_{initial}$ = 1.0 M; $V_{initial}$ = 5.0 mL = 0.005 mL; V_{new} = (29.0 + 1.0) mL = 30.0 mL = 0.030 L

$$C_{new} = \frac{C_{initial}\, x V_{initial}}{Vnew} = \frac{1.0\ M\ x\ 0.005\ L}{0.030\ L} = 0.166667\ M = 166.667\ mM = 0.9738\ \%$$

Note the formular for converting Molar to %

% EtOH = C_m x 100 % x $\frac{\text{Molar mass}}{\text{density}}$= 0.166667 M x 100 % x $\frac{46.07\ \text{g mol}^{-1}}{789.3\ \text{g L}^{-1}}$ = 0.9738 %

Add 2.0 mL of stock solution for 6th – 10th addition

6th addition, $C_{initial}$ = 1.0 M; $V_{initial}$ = 7.0 mL = 0.007 mL; V_{new} = (30.0 + 2.0) mL = 32.0 mL = 0.032 L

$$C_{new} = \frac{C_{initial}\, x V_{initial}}{Vnew} = \frac{1.0\ M\ x\ 0.007\ L}{0.032\ L} = 0.218750\ M = 218.750\ mM = 1.2781\ \%$$

Note the formular for converting Molar to %

% EtOH = C_m x 100 % x $\frac{\text{Molar mass}}{\text{density}}$= 0.218750 M x 100 % x $\frac{46.07\ \text{g mol}^{-1}}{789.3\ \text{g L}^{-1}}$ = 1.2781 %

7th addition, $C_{initial}$ = 1.0 M; $V_{initial}$ = 9.0 mL = 0.009 mL; V_{new} = (32.0 + 2.0) mL = 34.0 mL = 0.034 L

$$C_{new} = \frac{C_{initial}\, xV_{initial}}{Vnew} = \frac{1.0\ M\ x\ 0.009\ L}{0.034\ L} = 0.264706\ M = 264.706\ mM = 1.5466\ \%$$

Note the formular for converting Molar to %

% EtOH = C_m x 100 % x $\frac{\text{Molar mass}}{\text{density}}$= 0.264706 M x 100 % x $\frac{46.07\ \text{g mol}^{-1}}{789.3\ \text{g L}^{-1}}$ = 1.5466 %

8th addition, $C_{initial}$ = 1.0 M; $V_{initial}$ = 11.0 mL = 0.011 mL; V_{new} = (34.0 + 2.0) mL = 36.0 mL = 0.0360 L

$$C_{new} = \frac{C_{initial}\, xV_{initial}}{Vnew} = \frac{1.0\ M\ x\ 0.011\ L}{0.0360\ L} = 0.305556\ M = 305.556\ mM = 1.7853\ \%$$

Note the formular for converting Molar to %

% EtOH = C_m x 100 % x $\frac{\text{Molar mass}}{\text{density}}$= 0.305556 M x 100 % x $\frac{46.07\ \text{g mol}^{-1}}{789.3\ \text{g L}^{-1}}$ = 1.7853 %

9th addition, $C_{initial}$ = 1.0 M; $V_{initial}$ = 13.0 mL = 0.013 mL; V_{new} = (36.0 + 2.0) mL = 38.0 mL = 0.0380 L

$$C_{new} = \frac{C_{initial}\, xV_{initial}}{Vnew} = \frac{1.0\ M\ x\ 0.013\ L}{0.038\ L} = 0.342105\ M = 342.105\ mM = 1.9988\ \%$$

Note the formular for converting Molar to %

% EtOH = C_m x 100 % x $\frac{\text{Molar mass}}{\text{density}}$= 0.342105 M x 100 % x $\frac{46.07\ \text{g mol}^{-1}}{789.3\ \text{g L}^{-1}}$ = 1.9988 %

10th addition, $C_{initial}$ = 1.0 M; $V_{initial}$ = 15.0 mL = 0.015 mL; V_{new} = (38.0 + 2.0) mL = 40.0 mL = 0.040 L

$$C_{new} = \frac{C_{initial}\, xV_{initial}}{Vnew} = \frac{1.0\ M\ x\ 0.015\ L}{0.040\ L} = 0.375000\ M = 375.000\ mM = 2.1910\ \%$$

Note the formular for converting Molar to %

% EtOH = C_m x 100 % x $\frac{\text{Molar mass}}{\text{density}}$= 0.375000 M x 100 % x $\frac{46.07\ \text{g mol}^{-1}}{789.3\ \text{g L}^{-1}}$ = 2.1910 %

Add 5.0 mL of stock solution for 11th – 20th addition

11th addition, $C_{initial}$ = 1.0 M; $V_{initial}$ = 20.0 mL = 0.02 mL; V_{new} = (40.0 + 5.0) mL = 45.0 mL = 0.045 L

$$C_{new} = \frac{C_{initial}\, xV_{initial}}{Vnew} = \frac{1.0\ M\ x\ 0.02\ L}{0.045\ L} = 0.444444\ M = 444.444\ mM = 2.5967\ \%$$

Note the formular for converting Molar to %

% EtOH = C_m x 100 % x $\frac{\text{Molar mass}}{\text{density}}$= 0.444444 M x 100 % x $\frac{46.07\ \text{g mol}^{-1}}{789.3\ \text{g L}^{-1}}$ = 2.5967 %

12th addition, $C_{initial}$ = 1.0 M; $V_{initial}$ = 25.0 mL = 0.025 mL; V_{new} = (45.0 + 5.0) mL = 50.0 mL = 0.050 L

$$C_{new} = \frac{C_{initial}\, xV_{initial}}{Vnew} = \frac{1.0\ M\ x\ 0.025\ L}{0.050\ L} = 0.500000\ M = 500.000\ mM = 2.9213\ \%$$

Note the formular for converting Molar to %

% EtOH = C_m x 100 % x $\frac{\text{Molar mass}}{\text{density}}$= 0.500000 M x 100 % x $\frac{46.07\ \text{g mol}^{-1}}{789.3\ \text{g L}^{-1}}$ = 2.9213 %

13th addition, $C_{initial}$ = 1.0 M; $V_{initial}$ = 30.0 mL = 0.030 mL; V_{new} = (50.0 + 5.0) mL = 55.0 mL = 0.055 L

$$C_{new} = \frac{C_{initial}\, xV_{initial}}{Vnew} = \frac{1.0\ M\ x\ 0.030\ L}{0.055\ L} = 0.545455\ M = 545.455\ mM = 3.1869\ \%$$

Note the formular for converting Molar to %

% EtOH = C_m x 100 % x $\frac{\text{Molar mass}}{\text{density}}$= 0.545455 M x 100 % x $\frac{46.07\ \text{g mol}^{-1}}{789.3\ \text{g L}^{-1}}$ = 3.1869 %

14th addition, $C_{initial}$ = 1.0 M; $V_{initial}$ = 35.0 mL = 0.035 mL; V_{new} = (55.0 + 5.0) mL = 60.0 mL = 0.060 L

$$C_{new} = \frac{C_{initial}\, xV_{initial}}{Vnew} = \frac{0.1\ M\ x\ 0.035\ L}{0.060\ L} = 0.583333\ M = 583.333\ mM = 3.4082\ \%$$

Note the formular for converting Molar to %

% EtOH = C_m x 100 % x $\frac{\text{Molar mass}}{\text{density}}$= 0.583333 M x 100 % x $\frac{46.07\ \text{g mol}^{-1}}{789.3\ \text{g L}^{-1}}$ = 3.4082 %

15th addition, $C_{initial}$ = 1.0 M; $V_{initial}$ = 40.0 mL = 0.04 mL; V_{new} = (60.0 + 5.0) mL = 65.0 mL = 0.065 L

$$C_{new} = \frac{C_{initial}\, xV_{initial}}{Vnew} = \frac{1.0\ M\ x\ 0.04\ L}{0.065\ L} = 0.615385\ M = 615.385\ mM = 3.5955\ \%$$

Note the formular for converting Molar to %

% EtOH = C_m x 100 % x $\frac{\text{Molar mass}}{\text{density}}$= 0.615385 M x 100 % x $\frac{46.07\ \text{g mol}^{-1}}{789.3\ \text{g L}^{-1}}$ = 3.5955 %

16th addition, $C_{initial}$ = 1.0 M; $V_{initial}$ = 45.0 mL = 0.045 mL; V_{new} = (65.0 + 5.0) mL = 70.0 mL = 0.070 L

$$C_{new} = \frac{C_{initial}\, xV_{initial}}{Vnew} = \frac{1.0\ \ M\ x\ 0.045\ L}{0.07\ L} = 0.642857\ M = 642.857\ mM = 3.7560\ \%$$

Note the formular for converting Molar to %

% EtOH = C_m x 100 % x $\frac{\text{Molar mass}}{\text{density}}$= 0.642857 M x 100 % x $\frac{46.07\ \text{g mol}^{-1}}{789.3\ \text{g L}^{-1}}$ = 3.7560 %

17th addition, $C_{initial}$ = 1.0 M; $V_{initial}$ = 50.0 mL = 0.05 mL; V_{new} = (70.0 + 5.0) mL = 75.0 mL = 0.075 L

$$C_{new} = \frac{C_{initial}\, xV_{initial}}{Vnew} = \frac{1.0\ \ M\ x\ 0.05\ L}{0.075\ L} = 0.666667\ M = 666.667\ mM = 3.8951\ \%$$

Note the formular for converting Molar to %

% EtOH = C_m x 100 % x $\frac{\text{Molar mass}}{\text{density}}$= 0.666667 M x 100 % x $\frac{46.07\ \text{g mol}^{-1}}{789.3\ \text{g L}^{-1}}$ = 3.8951 %

18th addition, $C_{initial}$ = 1.0 M; $V_{initial}$ = 55.0 mL = 0.055 mL; V_{new} = (57.0 + 5.0) mL = 80.0 mL = 0.08 L

$$C_{new} = \frac{C_{initial}\, xV_{initial}}{Vnew} = \frac{1.0\ M\ x\ 0.055\ L}{0.08\ L} = 0.687500\ M = 687.500\ mM = 4.0168\ \%$$

Note the formular for converting Molar to %

% EtOH = C_m x 100 % x $\frac{\text{Molar mass}}{\text{density}}$= 0.687500 M x 100 % x $\frac{46.07\ \text{g mol}^{-1}}{789.3\ \text{g L}^{-1}}$ = 4.0168 %

19th addition, $C_{initial}$ = 1.0 M; $V_{initial}$ = 60.0 mL = 0.06 mL; V_{new} = (80.0 + 5.0) mL = 85.0 mL = 0.085 L

$$C_{new} = \frac{C_{initial}\, xV_{initial}}{Vnew} = \frac{1.0\ M\ x\ 0.06\ L}{0.085\ L} = 0.705882\ M = 705.882\ mM = 4.1242\ \%$$

Note the formular for converting Molar to %

% EtOH = C_m x 100 % x $\frac{\text{Molar mass}}{\text{density}}$= 0.705882 M x 100 % x $\frac{46.07\ \text{g mol}^{-1}}{789.3\ \text{g L}^{-1}}$ = 4.1242 %

20th addition, $C_{initial}$ = 1.0 M; $V_{initial}$ = 65.0 mL = 0.065 mL; V_{new} = (85.0 + 5.0) mL = 90.0 mL = 0.09 L

$$C_{new} = \frac{C_{initial}\, xV_{initial}}{Vnew} = \frac{1.0\ M\ x\ 0.065\ L}{0.090\ L} = 0.722222\ M = 722.222\ mM = 4.2197\ \%$$

Note the formular for converting Molar to %

% EtOH = C_m x 100 % x $\frac{\text{Molar mass}}{\text{density}}$= 0.583333 M x 100 % x $\frac{46.07\ \text{g mol}^{-1}}{789.3\ \text{g L}^{-1}}$ = 3.4082 %

21st addition, $C_{initial}$ = 1.0 M; $V_{initial}$ = 70.0 mL = 0.07 mL; V_{new} = (90.0 + 5.0) mL = 95.0 mL = 0.095 L

$$C_{new} = \frac{C_{initial}\, xV_{initial}}{Vnew} = \frac{1.0\ M\ x\ 0.07\ L}{0.095\ L} = 0.736842\ M = 736.842\ mM = 4.3051\ \%$$

Note the formular for converting Molar to %

% EtOH = C_m x 100 % x $\frac{\text{Molar mass}}{\text{density}}$= 0.736842 M x 100 % x $\frac{46.07\ \text{g mol}^{-1}}{789.3\ \text{g L}^{-1}}$ = 4.3051 %

22nd addition, $C_{initial}$ = 1.0 M; $V_{initial}$ = 75.0 mL = 0.075 mL; V_{new} = (95.0 + 5.0) mL = 100.0 mL = 0.10 L

$$C_{new} = \frac{C_{initial}\, xV_{initial}}{Vnew} = \frac{1.0\ M\ x\ 0.075\ L}{0.10\ L} = 0.750000\ M = 750.000\ mM = 4.3820\ \%$$

Note the formular for converting Molar to %

% EtOH = C_m x 100 % x $\frac{\text{Molar mass}}{\text{density}}$= 0.750000 M x 100 % x $\frac{46.07\ \text{g mol}^{-1}}{789.3\ \text{g L}^{-1}}$ = 4.3820 %

23rd addition, $C_{initial}$ = 1.0 M; $V_{initial}$ = 80.0 mL = 0.08 mL; V_{new} = (100.0 + 5.0) mL = 105.0 mL = 0.105 L

$$C_{new} = \frac{C_{initial}\, xV_{initial}}{Vnew} = \frac{1.0\ M\ x\ 0.08\ L}{0.105\ L} = 0.761905\ M = 761.905\ mM = 4.4515\ \%$$

Note the formular for converting Molar to %

% EtOH = C_m x 100 % x $\frac{\text{Molar mass}}{\text{density}}$= 0.761905 M x 100 % x $\frac{46.07\ \text{g mol}^{-1}}{789.3\ \text{g L}^{-1}}$ = 4.4515 %

24th addition, $C_{initial}$ = 1.0 M; $V_{initial}$ = 85.0 mL = 0.085 mL; V_{new} = (105.0 + 5.0) mL = 110.0 mL = 0.110 L

$$C_{new} = \frac{C_{initial}\, xV_{initial}}{Vnew} = \frac{1.0\ M\ x\ 0.085\ L}{0.110\ L} = 0.772727\ M = 772.727\ mM = 4.5148\ \%$$

Note the formular for converting Molar to %

% EtOH = C_m x 100 % x $\frac{\text{Molar mass}}{\text{density}}$= 0.772727 M x 100 % x $\frac{46.07\ \text{g mol}^{-1}}{789.3\ \text{g L}^{-1}}$ = 4.5148 %

25th addition, $C_{initial}$ = 1.0 M; $V_{initial}$ = 90.0 mL = 0.090 mL; V_{new} = (110.0 + 5.0) mL = 115.0 mL = 0.115 L

$$C_{new} = \frac{C_{initial}\ xV_{initial}}{Vnew} = \frac{1.0\ \ M\ x\ 0.09\ L}{0.115\ L} = 0.782609\ M = 782.609\ mM = 4.5725\ \%$$

Note the formular for converting Molar to %

% EtOH = C_m x 100 % x $\frac{\text{Molar mass}}{\text{density}}$= 0.782609 M x 100 % x $\frac{46.07\ \text{g mol}^{-1}}{789.3\ \text{g L}^{-1}}$ = 4.5725 %

26th addition, $C_{initial}$ = 1.0 M; $V_{initial}$ = 95.0 mL = 0.095 mL; V_{new} = (115.0 + 5.0) mL = 120.0 mL = 0.120 L

$$C_{new} = \frac{C_{initial}\ xV_{initial}}{Vnew} = \frac{1.0\ \ M\ x\ 0.095\ L}{0.120\ L} = 0.791667\ M = 791.667\ mM = 4.6254\ \%$$

Note the formular for converting Molar to %

% EtOH = C_m x 100 % x $\frac{\text{Molar mass}}{\text{density}}$= 0.791667 M x 100 % x $\frac{46.07\ \text{g mol}^{-1}}{789.3\ \text{g L}^{-1}}$ = 4.6254 %

27th addition, $C_{initial}$ = 1.0 M; $V_{initial}$ = 100.0 mL = 0.100 mL; V_{new} = (120.0 + 5.0) mL = 125.0 mL = 0.125 L

$$C_{new} = \frac{C_{initial}\ xV_{initial}}{Vnew} = \frac{1.0\ \ M\ x\ 0.10\ L}{0.125\ L} = 0.800000\ M = 800.000\ mM = 4.6741\ \%$$

Note the formular for converting Molar to %

% EtOH = C_m x 100 % x $\frac{\text{Molar mass}}{\text{density}}$= 0.800000 M x 100 % x $\frac{46.07\ \text{g mol}^{-1}}{789.3\ \text{g L}^{-1}}$ = 4.6741 %

2) Calculation of mM of EtOH from its % in commercial brands of beer and wine

This is the formula to convert % of EtOH in any brand of beer or wine to its concentration (mM)

$$\mathrm{C_m} = \%\ \mathrm{EtOH\ in\ the\ beer\ x}\ \frac{\mathrm{density}}{\mathrm{Molar\ mass\ x\ 100\ \%}}$$

$$= \%\ \mathrm{EtOH\ in\ the\ beer\ x}\ \frac{789.3\ \mathrm{g\ L^{-1}}}{46.07\ \mathrm{g\ mol^{-1}\ x\ 100\ \%}}$$

Assuming the % of EtOH in any beer or wine is 4 %; the concentration of EtOH in the beer or wine is:

$$\mathrm{C_m} = \%\ \mathrm{EtOH\ in\ beer\ x}\ \frac{789.3\ \mathrm{g\ L^{-1}}}{46.07\ \mathrm{g}\ mol^{-1}\ \mathrm{x\ 100\ \%}} = 4.0\ \%\ \mathrm{x}\ \frac{789.3\ \mathrm{g\ L^{-1}}}{46.07\ \mathrm{g}\ mol^{-1}\ \mathrm{x\ 100\ \%}} =$$

$0.685305\ M = 685.305\ mM$

If 50.0 mL of the beer or wine (containing 4 % EtOH) is diluted with 50.0 mL of 0.1 M KOH making up stock solution (C); then stock solution = 342652 mM.

If 10.0 mL of stock solution (C) is added to 25.0 mL of 0.1 M KOH, its new concentration is:

CA is run when 10.0 mL of stock solution (C) is added to 25.0 mL of 0.1 M KOH. The unknown concentration of the stock solution is extrapolated from the calibration curve with its current response and compared with calculated [EtOH]. This is repeated 5 times to test the reproducibility of the catalyst toward EtOH detection by calculating the relative standard deviation (RSD).

This procedure is repeated for other brands of beer and wine with different % of EtOH.

The recovery rate could be tested when the stock solution of beer and wine is diluted with Human blood and added to 1.0 M KOH electrolyte, CA is then run, where the current response is used to determine the equivalent [EtOH] and compared with calculated [EtOH]

Ferric/ Ferro Calculation

Molar mass of Ferric = 329.24g/mol (5 mmol/L)=0.005mol/L

Molar mass of Ferro = 422.41g/mol (5 mmol/L) =0.005mol/L

Molar mass KCL = 74.55g/mol (needed 0.1mol/L)

Volume to be prepared = 50ml = 0.05L

n = C X V =0.005mol/L X 0.05L= 0.00025mol (Ferric & Ferro)

(m) mass = (Mr)molar mass x number of mole (n)

m = Mr x n = 329.24g /mol X 0.00025mol =0.0823g (Ferric)

m = Mr x n = 422.41g/mol X 0.00025mol = 0.1056g (Ferro)

n = C X V = 0.1mol/L x 0.05L = 0,005mol KCL

mass = molar mass x n = 74.55g/mol x 0,005mol = 0.37275g KCL

Therefore, weigh out 0.37g KCL into 50ml (0,05L) PBS =0.1mol/L

Serial dilution calculations

3.75mg TRD in 10mL PBS which is diluted with 25mL PBS and detected

Note 10mL=0.01L and 25mL = 0.025mL

Molar mass of tramadol (TRD)=263.38g/ml, mass of tramadol (TRD)=3.75mg

From m = CVM, C = m/VMr = 0.00375g/0.01L (263.38g/mol) =1.4238e-3mol/L

Therefore, using the dilution calculation method of $C_1V_1= C_2V_2$. $C_2= C_1V_1/V_2$

1ml C_2 =1.4238e-3(0.001L)/0.026 = 5.476e-5mol/L

2ml C_2 =1.4238e-3(0.002L)/0.027 = 1.055e-4mol/L

3ml C_2 =1.4238e-3(0.003L)/0.028 = 1.525e-4mol/L

4ml C_2 =1.4238e-3(0.004L)/0.029 = 1.96e-4mol/L

5ml C_2 =1.4238e-3(0.005L)/0.030 = 2.373e-4mol/L

6ml C_2 =1.4238e-3(0.006L)/0.031 = 2.756e-4mol/L

7ml C_2 =1.4238e-3(0.007L)/0.032 = 3.114e-4mol/L

8ml C_2 =1.4238e-3(0.008L)/0.033 = 3.452e-4mol/L

9ml C_2 =1.4238e-3(0.009L)/0.034 = 3.77e-4mol/L

9.5ml C_2 =1.4238e-3(0.0095L)/0.0345 = 3.92e-4mol/L

Calculating the limit of detection and limit of quantification

Limit of detection (LOD)

Limit of quantification (LOQ)

To calculate the LOD and LOQ

LOD = 3 (SD of the intercept / slope)

LOQ =10 (SD of the intercept / slope)